Topology Optimization for Wave Propagation and Vibration Phenomena in Elastic and Piezoelectric Solids

by

Cory J. Rupp

B.S., Montana State University, 2004

M.S., University of Colorado, 2006

A thesis submitted to the

Faculty of the Graduate School of the

University of Colorado in partial fulfillment

of the requirements for the degree of

Doctor of Philosopy

Department of Mechanical Engineering

2009

This thesis entitled:
Topology Optimization for Wave Propagation and Vibration Phenomena in Elastic and Piezoelectric Solids
written by Cory J. Rupp
has been approved for the Department of Mechanical Engineering

Prof. Martin L. Dunn

Prof. Kurt Maute

Prof. Anton Evgrafov

Prof. Mahmoud I. Hussein

Prof. Hung "Jerry" Qi

Date

The final copy of this thesis has been examined by the signatories, and we find that both the content and the form meet acceptable presentation standards of scholarly work in the above mentioned discipline.

Rupp, Cory J. (Ph.D., Mechanical Engineering)

Topology Optimization for Wave Propagation and Vibration Phenomena in Elastic and Piezoelectric Solids

Thesis directed by Prof. Martin L. Dunn and Prof. Kurt Maute

Topology optimization is a versatile design tool for the synthesis of heterogeneous engineering systems where the optimal distribution of constituent materials is sought such that a prescribed measure of performance is optimized. In this dissertation, topology optimization methodologies are developed for solving problems associated with wave propagation and vibration in elastic and piezoelectric media. These methodologies utilize the finite element method in conjunction with gradient-based optimization algorithms to create functional materials, structures, and devices. The methodologies are demonstrated in a number of examples and illustrative studies that progress the state-of-the-art in the fields of topology optimization, elastic waveguides, phononic band-gap materials, and piezoelectric energy harvesting systems. These include the design of bulk and surface wave elastic waveguides in two and three dimensions that guide various forms of wave energy as desired, band-gap structures that provide tailored frequency transmission spectrums for bulk waves and surface waves, band-gap materials that prevent wave propagation within certain frequencies, and piezoelectric energy harvesting systems designed to optimize power output. Also addressed are previously unreported issues with the application of topology optimization to these types of problems including the role of physical phenomena in the solutions, mesh dependency effects, non-uniqueness, and the impact of small feature sizes.

Acknowledgements

This work was supported by the National Science Foundation Graduate Research Fellowship Program (NSF Graduate Research Fellowship) and the Air Force Office of Scientific Research (grant F49620-02-1-0037 and MURI grant F9550-06-1-0326 "Energy Harvesting and Storage Systems for Future Aerovehicles")

Contents

Chapter

List of Tables

List of Figures

Chapter 1

Introduction

1.1 Overview

Traditionally, heterogeneous materials and structures have been thought of in terms of effective properties that describe the overall response to a load [111, 154]. In static loading this is generally acceptable, but when elastic waves propagate through a material or vibrations shake a structure then size effects must be considered. Specifically, when the wavelength of a propagating wave or a vibrating mode is on the order of the feature sizes of the material or structure, many different phenomena can occur. These may include the generation of different propagating modes, resonant effects and interactions due to material interfaces such as Bragg reflections and mode conversion, and electromechanical coupling in piezoelectric materials. Because of size effects, general macro-scale analyses of effective properties, which do not account for these phenomena, may be invalid. Far from being a hindrance, many of these effects are in broad use in many common devices today such as resonators and signal filters in cell phones, modulators in fiber optic systems, ultrasonic wave generating and receiving equipment, and energy harvesting systems. Many of these technologies have been enabled by advances in nano- and micro-manufacturing allowing the fabrication of heterogeneous material systems (devices and structured materials) with precise positional control of the constituent materials. Taking advantage of this progress, one can envision the design of heterogeneous materials where the specific interaction of waves and vibration with the

material structure is considered to yield some arbitrary and desired objective such as the guiding of wave energy or the conversion of vibrations into electrical energy. The more complex this objective is, however, the more quickly the limits of human imagination and capabilities are reached. As such, there remains a need for a rational design methodology that enables an engineer to systematically develop wave propagation and vibration materials and structures of arbitrary complexity.

Since the initial work by Bendsøe and Kikuchi [10], topology optimization has proven itself as a promising tool for the design of complex devices and structures. Applications span all fields of engineering [11], but are quite limited in scope when it comes to wave propagation problems. The study of elastic wave propagation topology optimization problems can be divided into two areas: waveguides and band-gap materials. Waveguides generally concern the guiding of wave energy from one location to another while maintaining the strength and integrity of the signal. Band-gap materials are structured materials that prevent certain wave frequencies from passing through them while allowing others. Cox and Dobsen [29, 30] first exploited the potential of topology optimization for the design of photonic band-gap materials while Sigmund and Jensen [146] later used it for the design of elastic waveguides. Upon implementation, waveguides created using topology optimization have been shown to function as much as 10 times more efficiently and with increased bandwidth over conventional designs [14, 53]. Many facets of the topology optimization problem for wave propagation and vibration such as the influence of different wave modes or mesh dependency, however, have not yet been studied or reported in the literature though they are necessary to fully understand the problem.

In a particular application of topology optimization to systems with piezoelectric materials, a number of actuators and sensors have been optimally designed and methodologies developed [34, 59, 158], although the vast majority of these are for static applications. Topology optimization of dynamic piezoelectric systems, however, is still

a rich and understudied field with many promising applications. A large segment of this field focuses on vibrating piezoelectric energy harvesting systems. These systems use piezoelectric materials to convert ambient vibrations into electrical energy. Much of the design focus for these systems is on the harvesting structure where the electromechanical coupling through the piezoelectric material is be optimized to produce as much energy as possible [45, 91]. Separate optimizations on the electrical harvesting circuit have also been performed [104, 123, 140]. A methodology for the simultaneous optimal design of both the dynamic harvesting structure and circuit, however, is absent from the literature. Also missing from the dynamic piezoelectric systems field is a methodology for the use of topology optimization for waveguides and band-gap materials with piezoelectric materials.

With these systems in mind, the aim of this research is to develop and expand analysis and design methodologies using topology optimization for the generation of heterogeneous elastic and piezoelectric materials and structures subject to wave propagation and vibration. To this end, this dissertation focuses on topology optimization as applied to three areas: elastic waveguides, elastic band-gap materials, and wave propagation and vibration in piezoelectric solids.

1.2 Contributions

This dissertation contributes to the state-of-the-art in the following areas:

Topology optimization of elastic waveguides

Much of the initial and continuing work in this area has focused on various new applications of the topology optimization technique to useful elastic waveguide structures. The technique is generally established, although the vast majority of studies have neglected to investigate the underlying mechanisms and physical reasoning behind the designs they obtain. It is suggested that the wave phenomenon of Bragg reflections is the primary design driver for these problems and the reason for clear "0-1" solutions. It is

shown here that, while this may be true, other effects also play an important and unexpected, but sensible, role including localized material dispersion and anisotropy caused by material feature sizes smaller than the wavelength. This work provides a more in-depth investigation and development of the methodology than what is currently present in the literature for topology optimization of elastic waveguides. This methodology is also applied to previously unexplored aspects of topology optimization with wave propagation, namely mode conversion, surface waves, three-dimensional waveguides, and thin-film configurations.

Topology optimization of elastic band-gap materials

The design of band-gap materials via topology optimization is a relatively understudied field with few reported investigations into the needs, restrictions, and design drivers for the problem. The work presented here attempts to bring to light and answer some of the outstanding questions in the field including the efficacy of single-band objective functions and the presence of local optima in the problem. The shortcomings of previously developed objective functions such as the ability to only passively create a band-gap and the requirement to have a pre-existing band-gap are discussed and an improved methodology is presented. This new framework is applied to a series of previously unstudied optimization problems including: surface wave, plate, and three-dimensional wire band-gap problems as well as the design of a specialized mode filtering material that filters bulk waves based on the incident mode of propagation.

Topology optimization of wave propagation and vibration in piezoelectric solids

The field of vibrating piezoelectric energy harvesting systems is a relatively mature field in terms of analysis capabilities and simple design concepts. The designs of the harvesting structures, however, have generally been limited to uni-morph or bi-morph cantilever beams with end masses used to match the beam natural frequencies to the host vibration signature to maximize the available energy that can be converted to electricity.

Topology optimization of piezoelectric structures has also been previously reported, but not for a vibrating structure connected to an electrical energy harvesting circuit. This work fills this gap by developing a methodology for the design of piezoelectric energy harvesting structures and their external harvesting circuits with the goal of improving energy harvesting capabilities in a wide range of scenarios such as the use of arbitrarily shaped harvesting structures or systems with strict mass constraints. The methodology enables the design of arbitrarily layered and shaped piezoelectric structures while also accounting for both structural and electrical dynamic effects. In addition to piezoelectric energy harvesting, specialized elastic waveguides and band-gap structures composed of piezoelectric materials are also developed that have the previously unreported property of being able to completely turn on and off through presence or absence of an electric field and a spatially varying piezoelectric polarization.

1.3 Dissertation Organization

This dissertation is organized as follows. Chapter 2 introduces the three types of problems addressed in this document and gives background into the phenomena and current applications of each. Chapter 3 provides an overview of existing design methodologies for each problem and details the formulation and use of topology optimization as a design tool for them. Chapter 4 explores the first of these problems, namely topology optimization of elastic waveguides, presenting analysis techniques and the application of topology optimization with examples. Relevant studies and observations are also discussed. The next two chapters have similar structure and address topology optimization as applied to the topics of band-gap materials in chapter 5 and wave propagation and vibration in piezoelectric materials in chapter 6. Chapter 7 summarizes the findings in this document and outlines some future studies that could further expand the work presented herein.

Chapter 2

Background

2.1 Introduction

This chapter provides background on the various physical phenomena that exist in the fields of wave propagation and vibration in elastic and piezoelectric structures and how these phenomena are used in applications today. The chapter begins with an examination of many phenomena in wave propagation including the various modes of propagation, how they interact at material interfaces and in periodic structures, and how they can be converted into different forms. Next, piezoelectricity is discussed with its influence on wave propagation and its interaction with electroded structures. The chapter is then finished with an overview of many of the applications in which these phenomena are used.

2.2 Phenomena in wave propagation and piezoelectricity

Devices utilizing wave propagation and vibration in elastic or piezoelectric solids typically make use of one or more of the following phenomena. Special attention is paid here because these are the physical design drivers for the topology optimization process that is the focus of this dissertation. Telltale signs of these phenomena at work can be seen in the many examples of the following chapters.

2.2.1 Phenomena in wave propagation

Modes of propagation

The manner in which elastic wave energy propagates comes in a variety of flavors. In homogeneous, infinite, isotropic media waves are called bulk waves and come in three forms: pressure (P) or longitudinal waves and two polarizations of shear (S) or transverse waves. The pressure mode displaces the media in the same direction as that of propagation and has a propagation speed of $\sqrt{(\lambda + 2\mu)/\rho}$, where λ and μ are the Lamé coefficients and ρ is the mass density. The two shear modes, which are identical in form but independent in orientation, exhibit displacements perpendicular to that of the direction of propagation. In three dimensions there are two independent perpendicular directions for any propagation direction and thus two independent shear modes. These are commonly distinguished by calling them SV (shear vertical) and SH (shear horizontal) modes, which correspond to the in-plane and out-of-plane polarizations, respectively. The speeds of propagation of these two waves are identical and equal to $\sqrt{\mu/\rho}$, which is always smaller than the longitudinal wavespeed for real, homogeneous materials with Poisson's ratio $0 \leq \nu < 0.5$. Material anisotropy can drastically alter the way these waves travel, both in form and function. In isotropic media the phase velocity (speed and direction of peaks and troughs and here generally referred to as wavespeed) and group velocity (speed and direction of energy propagation) are equal in magnitude and constant for all directions, but in anisotropic media this is not necessarily true. For example, the wavespeed for pressure waves change by 250% with a change of propagation direction in highly oriented graphite-epoxy composite. The effect of anisotropy is often represented in a slowness curve, which is a plot of the inverse of phase velocity for each mode as a function of propagation angle (see Figure 2.1). In isotropic media, the slowness curve is just a series of circles (Figure 2.1a) with the inner circle representing the pressure wave and outer circle (actually two overlaid circles) representing the two

shear modes. The slowness curve in the orthotropic plane of graphite-epoxy composite (Figure 2.1b), however, shows a highly skewed quasi-pressure wave curve surrounded by the two quasi-shear modes. These modes are called quasi-modes because unlike their isotropic mode counterparts, the direction of displacement is not necessarily parallel or perpendicular to the direction of propagation.

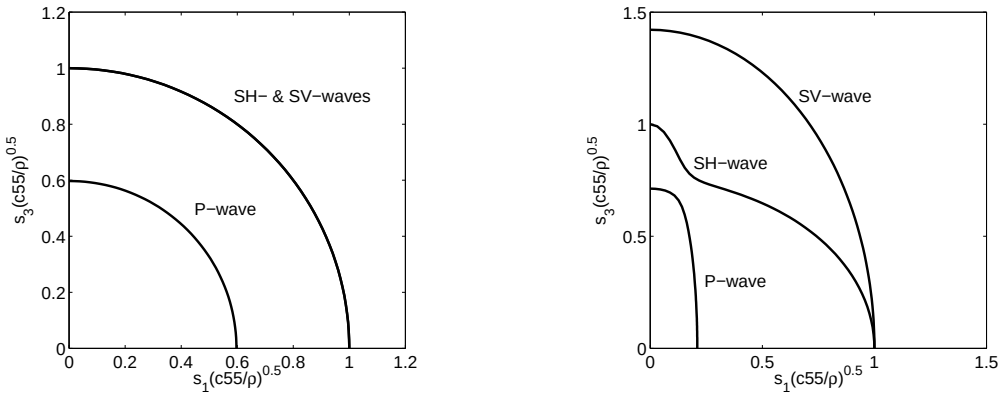

(a) (b)

Figure 2.1: Slowness curves for (a) isotropic silicon and (b) an orthotropic graphite-epoxy composite. Only a quarter of the curves are shown because of symmetries.

Surface modes represent a second flavor of elastic waves that occur only in the presence of a free surface. Surface waves have the unique and often desirable property that the energy of propagation is constrained to the free surface and decays in only two-dimensions as $1/\sqrt{r}$ from a point source, with r being the distance from the source, rather than the better known $1/r^2$ spatial decay rate of three-dimensional bulk waves. The most common type of surface wave is the Rayleigh wave. The displacements of this wave are coupled, occurring in the direction of propagation and the depth direction, and vary as a function of depth away from the surface in the manner show in Figure 2.2. In an isotropic material, the wavespeed is slightly slower than that of the shear bulk wave, is non-dispersive, and is dependent upon the Poisson's ratio of the material only. If

anisotropic or piezoelectric media or surface variations are considered, then a number of other surface waves can exist including shear acoustic surface waves in some anisotropic media (shear ASW), Bleustein-Gulyaev waves (BGW) in piezoelectric materials, and surface shear waves (SSW) in geometries with corrugated surfaces [3, 64]. Similar to bulk waves, the phase and group velocities as well as the form of the wave can depend on direction.

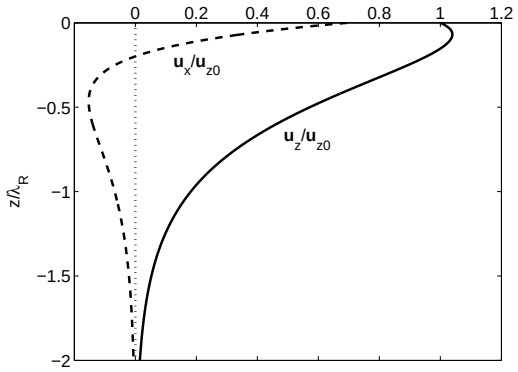

Figure 2.2: Rayleigh wave displacements in the x- (dashed) and y- (solid) directions as a function of depth normalized to the vertical displacement at the surface. The wave is propagating in the x-direction and attached to the free surface at $\frac{z}{\lambda_R} = 0$.

Naturally, as is the case with surface waves, when one or more changes are made to the boundary conditions of the propagating medium then other mode types can appear. For example, wave propagation in an infinite plate yields plate waves, also known as Lamb waves, which propagate along the length of the plate in either symmetric or anti-symmetric modes (see Figures 2.3a and b). These modes are dispersive, meaning that the group velocity is a function of frequency or wavenumber and also that the group and phase velocities are not necessarily equivalent. A peculiar property of Lamb waves is the realization of a negative group velocity for a certain range of frequencies/wave numbers meaning that while the peaks of the wave propagate in one direction, the energy

propagates in the other, a potentially desirable result. Plate geometries also exhibit SH shear plate modes, which are akin to SH shear bulk waves in that the displacement is normal to the viewing plane. Both Lamb and SH shear plate waves are families of related modes for which there may be many modes of each type existing at the same time, depending on the frequency of excitation and the wavenumber. Another notable and related form of wave propagation exists within a layer on a substrate of a different material and is called a Love wave. This type of wave exists when SH waves are "trapped" inside the layer due to total internal reflection as shown in Figure 2.3c. These waves are closely related to SH shear plate waves. At a material interface another mode, called the Stoneley wave, can exist. These waves, like many other specialized subgroups of wave types, only exist when certain conditions such as the adjacent media having sufficiently similar shear wave velocities in this case. A more detailed explanation of all these wave types can be found in a number of sources [3, 50, 62].

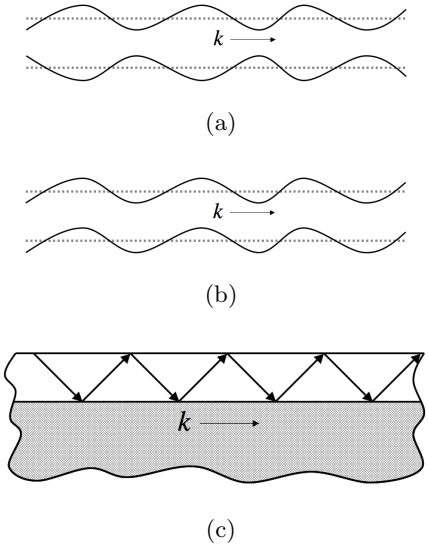

Figure 2.3: Propagation modes for (a) symmetric and (b) anti-symmetric Lamb waves in a plate and (c) Love waves which are caused by an SH wave trapped in a layer on a substrate. The arrow shows the direction of wave propagation with wavenumber k.

Reflection and transmission

Arguably the most important phenomena in wave propagation are wave reflection and transmission at a material interface. When a wave encounters an interface between two different media, some of the wave energy is transmitted and the rest is reflected. The amount of energy that gets transmitted/reflected depends on the material properties of the two media, specifically a value called the characteristic acoustic impedance Z. This value is dependent on the density ρ_α of the material α and the wavespeed c_α such that:

$$Z_\alpha = \rho_\alpha c_\alpha \quad \alpha = 1, 2 \tag{2.1}$$

When a wave travels through a material with impedance Z_1 and encounters a material with impedance Z_2 the wave will interact with a reflection coefficient r and transmission coefficient t such that:

$$r = \frac{Z_1 \cos\theta_\mathrm{i} - Z_2 \cos\theta_\mathrm{t}}{Z_1 \cos\theta_\mathrm{i} + Z_2 \cos\theta_\mathrm{t}} \tag{2.2}$$

$$t = \frac{2Z_1 \cos\theta_\mathrm{i}}{Z_1 \cos\theta_\mathrm{i} + Z_2 \cos\theta_\mathrm{t}} \tag{2.3}$$

for a given incident angle θ_i and transmitted angle θ_t related by Snell's law:

$$\frac{\sin\theta_\mathrm{i}}{c_1} = \frac{\sin\theta_\mathrm{t}}{c_2}. \tag{2.4}$$

These coefficients correspond to the reflection and transmission ratios of wave amplitude at the material interface. The reflectivity R and transmissivity T of energy take a different form:

$$R = \left| \frac{Z_1 - Z_2}{Z_1 + Z_2} \right|^2 \tag{2.5}$$

$$T = \frac{4Re(Z_1 Z_2)}{|Z_1 + Z_2|^2} = 1 - R \tag{2.6}$$

for normal incidence where the norm $|\cdot|$ and real operator $Re(\cdot)$ are present because in some situations it is useful to use a complex impedance to represent material energy losses. These expressions are only valid for a single mode of propagation at a time and may be different for different modes. Note that a couple special cases yield sanity checks

for these equations; for example the free and rigid boundary conditions. For the free boundary condition, the free space at the boundary has an impedance $Z_2 = 0$ and so the reflection coefficient is unity for all angles and although the transmission coefficient is $t = 2$, the transmissivity for energy is $T = 0$, so it is not contradictory. In the case with a rigid boundary the rigid impedance is $Z_2 = \infty$ for which the reflection coefficient is -1 (which takes into account the change in phase) and transmission coefficient limits to zero while their energy counterparts are the again unity and zero. Both cases make sense because all the energy is reflected at the interface as is expected. In the general case at normal incidence, it can be found that the reflectivity is maximized when the difference in impedance between the two materials, also known as the impedance mismatch, is maximized which correspondingly minimizes the transmissivity. Accordingly, the reflectivity is minimized and transmissivity maximized when the impedance mismatch is as small as possible (i.e. the materials look similar from the wave's perspective). This, however, changes with varying angle because Snell's law can break down for $\frac{c_2}{c_1}\sin\theta_\mathrm{i} > 1$, a condition for which total reflection occurs, although an evanescent wave (non-propagating, decaying wave) can appear on the transmitted side of the interface.

Bragg reflections

An elastic band-gap, or phononic, material is a micro-structured material that exhibits the property that elastic waves of certain frequencies will not pass through the material. The idea behind band-gap materials stems from the dispersion relationship for a structured composite material. The dispersion relationship is the relationship between frequency and wavevector for a wave traveling through a medium, usually shown in a dispersion diagram that reveals the allowable modes of propagation. In infinite, homogeneous, isotropic media, the modes of propagation consist of the three bulk modes (P, SV, and SH waves). Figure 2.4a shows a dispersion diagram for a typical bulk isotropic material. The dispersion diagram for a band-gap material, in which there exists a range of frequencies, or a band, for which no modes of propagation

exist, seen in Figure 2.4b. The existence of this forbidden band is based solely on the structural layout of the composite material, while the form of the band-gap and the rest of the dispersion relationship is additionally dictated by the properties of the constituent materials. Information other than the presence of band-gaps can also be obtained from the dispersion diagram, including the phase velocity $v_p = \omega/k$ and the group velocity $v_g = \partial\omega/\partial k$, which is the slope of the line in the diagram, making it an important source of information.

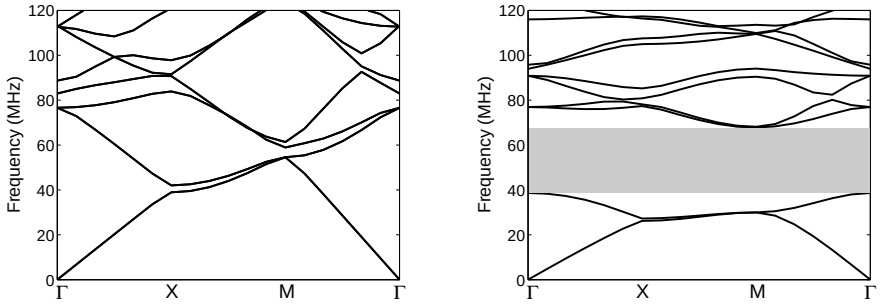

(a) (b)

Figure 2.4: Example dispersion diagrams for (a) typical bulk isotropic and (b) band-gap materials where Γ, X, and M are wavevector values/directions for symmetry points in the band-gap material. Modes of propagation exist only when there is at least one wavevector for a corresponding wave frequency.

One of the most fundamental concepts about band-gap materials and structures is that of the Bragg condition:

$$k\,\Lambda = m\,\pi \tag{2.7}$$

where k is the wavenumber, Λ is the lattice constant, and m is an integer. This equation dictates the condition under which a wave will interfere constructively/destructively and be reflected within the material in which it is propagating. For a one-dimensional periodic material, it reveals that a band-gap occurs when the half-wavelength of the

propagating wave is an integer multiple of the lattice constant which is the length scale of the smallest repeatable unit within the material (also called the unit cell). These structures are commonly called Bragg gratings for which the wave that the travels through them undergoes Bragg scattering or Bragg reflections. The equation also implies that there are an infinite number of band-gaps for a given lattice constant. For large m, however, they become indistinguishable from each other, a phenomenon more commonly found and studied in quantum mechanics.

As an example of the Bragg scattering in a Bragg grating, consider a one-dimensional grating N unit cells in length. The reflectivity $|r_N|^2$ for a wave with wavevector k traveling through the grating can be found via the transfer matrix method as:

$$|r_N|^2 = \frac{|\gamma|^2}{|\gamma|^2 + \left(\frac{\sin(k\Lambda)}{\sin(Nk\Lambda)}\right)^2} \tag{2.8}$$

where γ is related to the reflectivity of a single unit cell $|r_1|^2$ by:

$$|\gamma|^2 = \frac{|r_1|^2}{1 - |r_1|^2} \tag{2.9}$$

Figure 2.5 shows the reflectivity of the Bragg grating $|r_N|^2$ for three values of N and a unit cell reflectivity $|r_1|^2 = 0.05$. It is easy to see from the plots that the reflectivity approaches unity when the Bragg condition is met. Also, it is clear that increasing N results in increased reflectivity as well as narrower band-gaps. The Bragg condition is a recurring theme in wave propagation and its presence can be inferred later in examples of not only band-gap materials but also in waveguide structures.

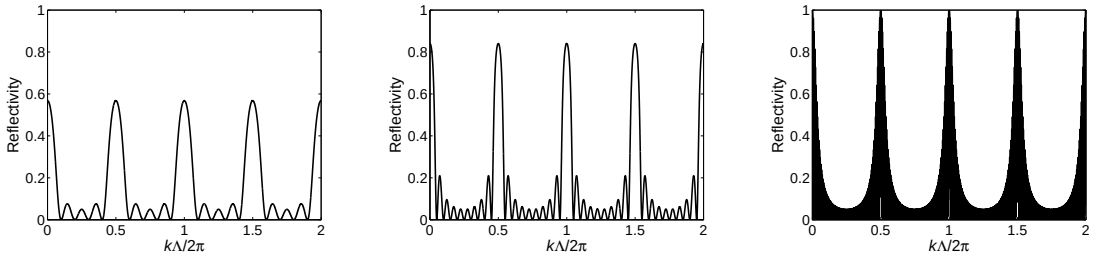

(a) (b) (c)

Figure 2.5: Reflectivity of a Bragg grating for various numbers of unit cells: (a) 5, (b) 10, and (c) 100. Band-gaps can clearly be seen where the Bragg condition is met while increasing the number of unit cells increases the reflectivity at these locations.

Mode conversion

Reflection and transmission of waves can be complicated through mode conversion in which one mode incident upon an interface may disassociate into a mode of its own type as well as other modes. For example, a pressure wave incident on an interface at an angle will split into instances of both reflected and transmitted pressure and shear waves with the total energy divided between them. As such, reflection and transmission coefficient relationships are highly dependent on the incident angle and mode type. In anisotropic materials the complexity of mode conversions and reflection and transmission increases significantly. An incident wave of any type (P, SV, SH) can reflect and transmit into all three of the mode types and the acoustic impedance is also a function of propagation angle and material orientation. Derivations of many of these relationships as well as specific examples can be found in Auld [3].

2.2.2 Piezoelectricity

Piezoelectric effect

Piezoelectric materials are a class of materials in which the atomic structure of the material is such that when strained an electric field is produced. This effect,

called the direct piezoelectric effect, also has a reciprocal effect, called the converse piezoelectric effect, where a piezoelectric material subject to an electric field, usually actuated through a voltage applied to electrodes, will produce a strain in the material. Together, these effects fully couple the mechanical response to the electrical response for any system that uses piezoelectric materials. The constitutive law that depicts this coupling is written as:

$$\begin{aligned} \mathbf{T} &= \mathbf{c}^E : \mathbf{S} - \mathbf{e} \cdot \mathbf{E} \\ \mathbf{D} &= \mathbf{e} : \mathbf{S} + \epsilon^S \cdot \mathbf{E} \end{aligned} \tag{2.10}$$

where $\mathbf{T}$ is the stress field, $\mathbf{c}^E$ is the constitutive stiffness matrix for constant electric field, $\mathbf{S}$ is the strain field, $\mathbf{e}$ is the piezoelectric strain tensor, $\mathbf{E}$ is the electric field, $\mathbf{D}$ is the electrical displacement field, and ϵ^S is the permittivity matrix for constant strain.

Wave propagation in piezoelectric materials

In a piezoelectric material, because the strain field is coupled with the electric field, any wave that passes through the material travels differently than it would through an uncoupled material. In addition to the coupled fields, piezoelectric materials are anisotropic, so a number of different wave modes can appear just on that basis. Generally, any mechanical wave is accompanied by a parasitic electromagnetic wave with the same propagation direction and vice-versa. These are called quasi-acoustic and quasi-electromagnetic waves, respectively, and have slightly altered wavespeeds. This change in wavespeed, however, is very small, primarily because of the difference in propagation speeds between elastic and electromagnetic waves. In some cases an elastic wave will not create an electromagnetic field and will instead create an electric field only in either the propagation direction or normal to the propagation direction. In the "3-1" class of piezoelectric materials, which are considered in this document, a wave traveling in the "1-direction" creates a perpendicular alternating electric field in the "3-direction" whose energy may be gathered or transferred elsewhere. Further details on wave propagation in piezoelectric materials can be found in Auld [3].

Charge cancellation in piezoelectric structures

In the operation of dynamic structures, strain varies as a function of location. In piezoelectric structures this means that distributions of positive and negative charge are also present, which, if connected through electrodes, will cancel to produce zero net charge. For example, an elastic wave traveling through an electroded "3-1" piezoelectric plate will produce alternating areas of positive and negative charge that are carried through the electrode and cancel each other out resulting in a net zero voltage across the electrodes. Similarly, in vibrating piezoelectric energy harvesting structures, the excited mode shape will produce regions of positive and negative strain whose charges will cancel if connected by the same electrode. This effect is noted in the papers of Erturk and Inman [40] and Erturk et al. [45], who, in their investigations of strain nodes (where strain changes sign), find that if an electrode crosses the strain node then charge cancellation occurs, degrading the performance of the piezoelectric harvester. This finding was also reported by Kim et al. [91, 92] for circular plates. In these studies, the authors rectify the charge cancellation by either segmenting the electrodes or changing the piezoelectric polarization to match the strain state. Doing so allows energy to be harvested from both tensile and compressive strain regions without cancellation. In general, it is best to avoid charge cancellation in order to maximize performance of a device.

2.3 Applications

Outlined here are a number of existing applications for wave propagation and vibrations in elastic and piezoelectric solids and structures. Specifically, applications in the areas of elastic waveguides, band-gap materials, and vibrating energy harvesting systems are considered.

2.3.1 Elastic waveguides and band-gap materials

Elastic waveguides and band-gap materials share many physical phenomena and therefore have many mutual applications. In fact, one of the primary uses of band-gap materials is to create waveguides by introducing line defects, a design method that will be discussed in more detail in the next chapter. Outlined here are some of the many applications of these closely related structures.

Ultrasonics

One of the major uses of general wave propagation is in ultrasonic inspection and characterization. Ultrasonics is defined to be the study of the propagation of acoustic waves at frequencies above the range of human hearing (i.e. you would need ultra-hearing to hear the waves) all the way up to about 1GHz at which point it is generally called hypersonics. Ultrasonic waves are usually actuated by piezoelectric transducers that use piezoelectric materials and the piezoelectric effect to convert an electric signal into an acoustic signal. Many types of transducers exist, including bulk wave (both pressure and shear modes) transducers and surface wave transducers, just to name the most common types. These can come in pulse mode or harmonic mode variations. Lasers are also used as a non-contact source of acoustic energy through the use of the thermo-acoustic effect. A laser incident on a surface heats the local area causing it to expand and create an acoustic pulse. The laser can also be modulated to create a wave of a certain frequency or frequencies. Both piezoelectric transducers and lasers are also used as acoustic sensors with transducers again using the piezoelectric effect to change an acoustic signal into an electric signal and lasers using interferometry techniques. An overview of various transducers types and their specific applications can be found in Cheeke [22].

Ultrasonic inspection is used in many different fields for a large variety of purposes. The field of nondestructive evaluation (NDE) is based upon using ultrasonics to test and

evaluate the condition of materials and structures. In its simplest form, a transducer is used to introduce an acoustic wave pulse into a material and sense any reflection of the wave off interfaces within the material whether it be another surface, a material interface, or an unwanted crack or defect. By timing the signals, the location of these features can then be determined and defects can be distinguished from otherwise known interfaces. For example, if a signal returns before it is expected then a defect is usually present. These very same techniques are used in medical ultrasonic imaging in which a transducer sends and receives an acoustic wave that gets distorted and reflected as it travels through variations in the composition of the human body. The variations in the signal can then be used to construct a diagnostic image of the organs. Another medical procedure that uses ultrasound is the breakup of kidney and gallstones in the body that often cause much pain in patients. For this procedure, a high intensity ultrasonic beam is focused upon the stone, which under high acoustic intensity breaks up into smaller pieces thereby allowing the body to pass the stone and relieving the patient of pain. A similar procedure is also used in manufacturing processes to machine and drill materials as well as to create joints using ultrasonic soldering and welding. The focusing of an ultrasonic beam to a point is also used in ultrasonic microscopy which functions in the same way as a light microscope but with acoustic waves rather than light waves. Ultrasonic microscopy is often used to create micro-scale subsurface images of opaque materials that would otherwise be unseen. It is also used to characterize the material properties of various bulk materials, but at a small scale and using only a small sample.

Sensors

When an acoustic wave passes through a changing environment, the manner in which wave itself propagates also changes. This is the basis of detection methods used in acoustic sensors to detect physical, biological, or chemical changes in an environment. Changes in wave propagation characteristics are usually sensed by using transducers to send and receive a known acoustic signal through an environment of interest. If

the received signal changes in frequency, phase, or amplitude relative to some reference state, then it is known that the environment has also changed. For example, some sensors place a thin reactive film on a substrate that reacts with a specific molecule (a chemical of biological agent) that may or may not be present in the environment. The presence of the molecule will change the characteristics of the film through mass loading or elasticity effects, thereby altering the acoustic signal that passes through it. The change in signal, conversely, indicates the presence of that specific molecule thereby completing the role of the sensor. This idea is very basic, but the implementation is much more technical. For example, some modes of propagation are less sensitive than others to changes such as mass loading or changes in elastic constants. For sensors built with a thin film sensing medium coating a substrate, bulk modes are rather insensitive to mass loading, but Lamb modes and surface wave modes can be approximately 30 times more sensitive [22]. As a result, many very specific types of sensors utilizing specific wave propagation modes have been developed that use a variety of methods to sense changes in the environment. Other examples of sensors other than chemical and biological agent sensors include density, viscosity, temperature, flow, and level sensors.

Signal processing

Electronic circuits are increasingly being integrated with elastic wave based devices that allow them to perform a wide variety of functions that would otherwise not be possible. Examples of such devices are surface acoustic wave (SAW) filters, delay lines, SAW resonators, oscillators, coded time domain structures, convolvers, and multistrip couplers [22]. Technologies that these devices are used in include radios, mobile phones, garage door openers, and fiber optic repeaters. Many of these devices utilize Rayleigh waves created by interdigital transducers (IDT). An interdigital transducer consists of a periodic array electrodes placed on a piezoelectric substrate, essentially creating a band-gap structure. It works by applying a voltage signal to the electrodes, which in turn create a spatially varying strain field through the converse piezoelectric effect. Nu-

merous IDT designs exist, each trying to increase or decrease effects or noise in the resulting elastic wave. The SAW resonator, as an example, has two IDTs (one to create the wave and one to receive) often separated by a periodic array of reflecting lines of a different material (a Bragg grating). The characteristics of this device can be altered by changing either the configuration of the IDTs or changing the Bragg grating properties. The focus of many studies has been to optimize the form, strength and directionality of the elastic waves created by the IDTs [119] or in some cases to use different wave modes such as Stoneley waves [88]. Another application is to use acoustic waves to influence the propagation of light. Examples of devices that do this include the Mach-Zehnder interferometer (based on acoustic wave induced changes in light wavespeed causing constructive and destructive interference of two coherent beams) and acousto-optic modulators (based on Brillouin scattering, a phenomenon akin to Bragg scattering and Bragg gratings, but where changes in material refractive index are caused by the propagation of an acoustic wave). These devices are used to modulate signals in laser systems, where an electric signal is converted into an acoustic signal and then into an optic signal, generally for use in fiber optic communication.

Band-gap material applications

A disparate array of applications for band-gap materials are either in use or have been suggested. Acoustic fibers, the acoustic analogue to crystal fibers in optics (electromagnetic waveguides), are used as a means to guide acoustic waves across large distances with low loss and low dispersion with applications as delay lines or as a means to carry an acoustic signal to a remote sensor. Band-gap materials are also used to reduce acoustic noise, for both vibration isolation and architectural applications [94, 133]. In promising future applications, band-gap materials have been proposed to create acoustic invisibility and negative refraction. The concept of invisibility, focused primarily in the field of photonics, but slowly moving into phononics, concerns the development of so-called negative refraction index or left-handed materials. These special materials

theoretically have the ability to create spheres of invisibility that can render an object invisible to outside detection [32, 114, 126] or superlenses that can breach the wave-focusing diffraction limit [115, 125, 162]. They are created by introducing localized resonances within the material structure and are often called meta-materials. Also of interest is the use of band-gap materials as so-called hypersonic phononic crystals that affect the flow of high frequency thermal phonons, which in turn changes the thermal properties of the material [61].

2.3.2 Vibrating piezoelectric energy harvesting systems

The use of piezoelectric materials incorporated into structures to harvest energy from ambient vibrations has received significant attention over the last decade with the overarching goal of eliminating or reducing the need of external power sources or batteries to power remotely operated devices. The interest in vibrational energy harvesting has been motivated by advances in low-power electronic components such as wireless sensors for structural health monitoring and tire pressure sensors, actuators that can be powered remotely, and by the need for supplemental energy sources for unmanned aerial vehicles [46]. Additional motivation is provided by the desire to develop such devices with simultaneous structural and power generation functionality, which can reduce weight, material usage, and costs. The interest in piezoelectric energy harvesting is reflected in a number of authoritative reviews that have been written in recent years [2, 7, 28, 37, 43, 129, 147]; extensive details regarding applications, experimental techniques, and modeling and design approaches can be found within these references.

Chapter 3

Design Methodologies

3.1 Introduction

This chapter outlines some of the existing design methodologies used today to create elastic waveguides, band-gap materials, and piezoelectric structures. These range from simple trial-and-error procedures to highly automated topology optimization techniques. Special focus is given to topology optimization including a detailed description of the general theoretical and computational framework. The chapter starts with a review of the existing design methods, then describes the topology optimization framework including general sensitivity analysis, and ends with examples of how topology optimization has been used in the field to date.

3.2 Existing design methods

This section provides an overview of the design methods for waveguides, band-gap materials, and piezoelectric structures. Through many decades these methods have changed and evolved starting with designs based on macro-scale flow engineering and phenomena to now creating customized micro- and nano-structured devices and materials that perform very specific functions.

3.2.1 Elastic waveguides and band-gap materials

Waveguides

Long before acoustics was commonly considered a self-encompassed field a number of inventions involved the use of acoustic waveguides. Examples include a number of musical instruments, namely the woodwinds and brass, the horn shaped hearing devices of the early 19th century, and sound lines to carry voice commands between decks of a ship. These first acoustic waveguides were likely viewed as flow channels for sound. They were simple and relied primarily on having high reflection coefficients caused by adjacent materials with high impedance mismatches to create total internal reflection and keep the wave contained within the waveguide (e.g. air surrounded by a metal horn or tube).

Similar techniques have since been developed for the creation of elastic waveguides. The easiest way to do this is to use a long thin rod in air or a vacuum. The high impedance mismatch contains the various elastic wave modes that a rod can support with its geometry, again using total internal reflection. Gentle curves can be created in these waveguides to change the direction of the wave, but only if the radius of curvature is much greater than the wavelength (at least 10 times), otherwise the waveguide will leak or reflect acoustic energy [22]. This is a key point and one of the major limitations for this type of waveguide. Other related issues include the presence of dispersion, which occurs in most non-bulk wave modes. Efforts to overcome dispersion in such waveguides have resulted in the design of capillary and fiber waveguides which function in a similar way as fiber optic lines [22].

Other geometries can also be used for waveguides, most of which use variations in geometry or material composition to contain one or many mode types. Examples include creating a ridge or wedge on the substrate of the same material or building a strip or slot of a different material on the substrate (see Figure 3.1). These waveguides,

called topographic waveguides, rely primarily on the presence of propagation modes that are a direct consequence of the existence of those features (e.g. plate-like modes in ridge waveguides). As a result, these guided modes are strongly attached to the geometry variation and the wave will follow any change in course of the geometry. The cross-sectional shape of the waveguide and the mode of propagation highly affects whether or not the propagation is dispersive, attributing some waveguides with much more desirable properties than others.

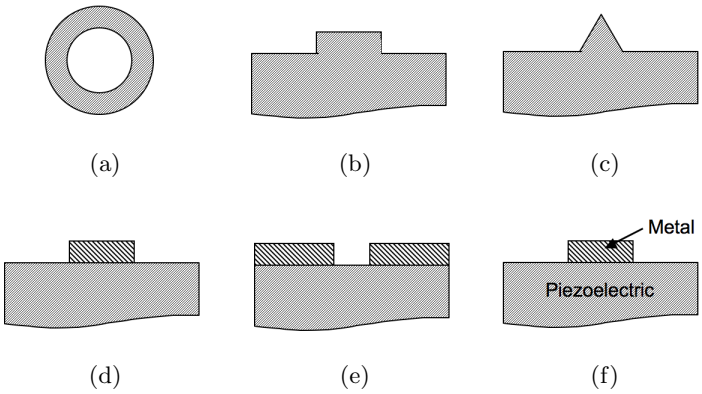

Figure 3.1: Waveguide types: (a) capillary or fiber, (b) ridge, (c) wedge, (d) strip, (e) slot, (f) shorting strip.

Another class of waveguides, called overlay waveguides, involve placing a layer of different material on a substrate in various configurations in order to create material interfaces and change the local properties. In the case of the strip waveguide, when the strip has a sufficiently lower wavespeed than the underlying substrate, Love waves become trapped in the layer and are then guided by it. This, however, is also dependent on the dimensions of the strip. For strips of low height and high wavespeed, the Rayleigh wave velocity is slowed locally thereby trapping Rayleigh waves in the local area under the strip. The slot waveguide works in the same fashion but the area under the strip has a faster Rayleigh wave velocity. If the substrate happens to be piezoelectric and the

overlaying strip a metal, then a variation of a piezoelectric Rayleigh wave forms and is guided by the metallic strip. Auld [3], who also discusses anisotropic waveguides, and Cheeke [22] both give good overviews of these types of waveguides.

As mentioned briefly in the last chapter, the development of two-dimensional band-gap materials resulted the invention of a new class of waveguides based on band-gap materials. While the presence of a band-gap material prohibits the propagation of wave energy through the material within a certain frequency range, it is also true that the absence of that material allows the wave to pass. More importantly, it has been shown that defects in band-gap materials allow for localized states (propagating and non-propagating) within the band-gap to exist even though it would normally be prohibited [87]. When defects are organized into lines, such as by removing a row of inclusions in the host matrix, then line defect waveguides are formed. Joannopoulos et al. [87] was one of the first to show this with photonic crystals and Sigalas [144] later did the same for phononic crystals.

The simplest line defect waveguide is of course a straight waveguide, which in some situations can serve as a delay line. Of more interest are various bending waveguides. These waveguides are used in optics as well as ultrasonics and signal processing to guide wave energy to a desired location. Such devices have been found to be more efficient and more compact than their total internal reflection based counterparts. For example, 90° bend photonic/phononic crystal waveguides are capable of bending light in the space of only about a wavelength, a drastic improvement when compared to the tens of wavelengths needed for traditional waveguides [87]. One drawback of these designs, however, is that the properties of the bending waveguide are highly dependent on the array and defect characteristics [26]. As a result, designing a photonic or phononic waveguide has developed into an effort to create the lowest loss, highest bandwidth combination of crystal arrays and defects, which is usually done by moving the defect lines or changing defect shapes through a trial and error method (e.g. [27]). In addi-

tion to waveguides, band-gap materials have also used the same techniques to create a number of special function waveguide devices such as multiplexers and demultiplexers, filters, modulators, and switchers [21, 127, 128] which are useful in signal processing applications. Most of these applications have been created for the field of photonics for which Prather et al. [128] give a nice history. The field of phononics on the other hand is much less developed, partly due to the increased complexity in the physics as well as the less immediately apparent advantages.

Band-gap materials

Early investigations into the band-gap phenomenon in spatially periodic structures focused on naturally occurring structures, usually of biologic origin, with peculiar optical properties. Early observations of iridescence, a band-gap caused phenomena, were reported in chlorate of potash crystals by Stokes in 1885 [149] and Rayleigh in 1888 [130]. More recently, what were later named photonic crystals were been found to be the cause of iridescence in opals, peacock feathers, and butterfly wings [93]. Both photonic and phononic band-gap materials can attribute their foundation to these observations.

Probably the first engineered use of phononic band-gaps was in the development of the surface acoustic wave (SAW) suite of devices starting around 1965 [119], with the first SAW resonator appearing in 1970 [64]. These early devices used simple Bragg gratings to reflect waves of a given frequency making a frequency filter which is useful in a number of signal processing and communication devices. As a result of this discovery, research in this area boomed with the use of various variations of Bragg grating-like structures to control the propagation of many different modes of elastic waves. The devices designed today still use the same basic ideas as the original inventions, usually by using uni-directional Bragg gratings, and are now generally referred to as band-gap or stop-band devices and materials.

Bragg gratings are generally considered one-dimensional band-gap materials be-

cause waves traveling parallel to the grating lines will not exhibit a frequency dependent response. The idea for two-dimensional photonic band-gaps was introduced by Yablonovitch in 1987 [159]. This was followed up with experiments where designed a face-centered-cubic structure was designed with dielectric spheres in air [161]. These structures consist of periodicity of a unit cell in two dimensions. The unit cell generally consists of a simply shaped inclusion embedded in a host material. It has only been since this time that the terms photonic crystals or photonic materials have been used. In three dimensions a complete band-gap, where no propagation exists for any direction, was later predicted in a particular diamond lattice of dielectric spheres in air by Ho et al. [73] and experimentally shown by Yablonovitch [160]. This was a much more difficult search and largely relied on creating designs based on atomic lattice structures. Joannopoulos et al. [87] give a good overview of these findings in the field of photonic crystals.

The studies and design methods performed in the field of photonic crystals were eventually generalized to phononic materials, where most of the mathematical techniques are the same. As such, Sigalas and Economou [145, 143] as well as Kushwaha et al. [95] were the first to design two- and three-dimensional phononic band-gaps in 1992 and 1993. Later studies have investigated other forms of elastic wave propagation and include designs for two-dimensional phononic crystals for Rayleigh waves [152, 153] and Lamb modes [76, 77]. Much focus in this field has been on the design of two-dimensional structures with to manufacturability concerns and constraints in mind. As a result, many studies have looked at embedding cylinders or other prismatic shapes in a host matrix of another material and looking at the band-gap properties for propagation in the two-dimensional plane. As a natural next step, a large number of groups have performed parametric studies on these materials by changing various properties such as the composition of both the inclusion and host materials [73, 95], changing the size or filling ratio of the inclusion [73, 143, 161], and changing the shape of the inclusion

[73, 87]. These studies, as a result, provide a number of tools and methods for engineers to create photonic and phononic materials with various band-gap properties.

3.2.2 Piezoelectric structures

The design of piezoelectric structures largely focuses on the fields of actuation, sensing, or energy harvesting. Piezoelectric actuation and sensing of elastic waves are the means by which surface acoustic wave device operate. The design of these devices, as described earlier, focuses almost entirely on the patterning of electrodes on a piezoelectric substrate. Ultrasonic transducers also use piezoelectric actuation and sensing functions, but the focus of design is usually on the size and shape of the piezoelectric element, rather than the electrode patterning. These are the primary areas where piezoelectric materials are used in wave propagation applications.

A focus of this dissertation is the design of piezoelectric energy harvesters. Flat beam and plate structures are typically used for these problems because they allow for a large generation area that can be actively strained by the vibration of a host structure, ease of analysis, and ability to be "tuned" to the host structure vibration signature. Most piezoelectric energy harvesting approaches to date focus on the electromechanics of the piezoelectric transduction and use a transient or steady-state vibrational signature, usually at resonance, as input for the base excitation of the piezoelectric harvesting structure. Important aspects of this problem, however, are often neglected. Erturk and Inman [40] and Erturk et al. [45] demonstrate that while traditional lumped parameter analysis approaches provide much of the basic understanding, they lack important information about the coupled electromechanics, e.g., the existence of strain nodes at different resonances or the feedback of the circuit dynamics to the structural response. Their studies and other recent approaches have focused on improving on these failings by introducing segmented electrodes [117] or re-poled piezoelectric material distributions [91, 92]. Other design advances include creating segmented cantilever beam structures

that take advantage of both segmented electrodes and different structural dynamics [46].

3.3 Topology optimization

Topology optimization is a methodology for systematically solving design problems where some goal of optimal performance is sought. A commonly used example in structural mechanics is to maximize the stiffness of a truss for a given maximal weight. In solving this problem, topology optimization uses a mathematical measure of this goal to systematically distribute both material and void regions within some prescribed design domain such that this measure, and thus the goal, is maximized (or minimized). The formulation of this mathematical measure, or objective function and/or constraints, is of key importance as it must fully describe the goal, scope, and physics of the problem, yet not be so restrictive that it prevents exploration of alternative, even physically impossible, designs. As such, it is a focus of this dissertation as well as the development of topology optimization methodologies that take advantage of the physical phenomena in the three areas of interest.

This section describes the formulation of the topology optimization problem, how it is solved, and how it has been used previously in areas closely related to this dissertation.

3.3.1 Formulation

The formal topology optimization problem statement can be written as a constrained minimization problem:

$$\begin{aligned} \min_{\mathbf{s}} \quad & z\left(\mathbf{s}, \mathbf{u}\left(\mathbf{s}\right)\right) \\ \text{s.t.} \quad & \mathbf{K}\left(\mathbf{s}\right)\mathbf{u} = \mathbf{f} \\ & g_j\left(\mathbf{s}, \mathbf{u}\left(\mathbf{s}\right)\right) \geq 0 \quad j = 1 \ldots n_g \\ & h_k\left(\mathbf{s}, \mathbf{u}\left(\mathbf{s}\right)\right) = 0 \quad k = 1 \ldots n_h \\ & 0 \leq s_i \leq 1 \qquad\quad i = 1 \ldots n_s \end{aligned} \tag{3.1}$$

where z is the objective function depending on the n_s number of design variables $\mathbf{s} = (s_1, \ldots, s_{n_s})^T$ and n_g inequality and n_h equality constraints g_j and h_k, respectively. The solution $\mathbf{u}$ to the system $\mathbf{K}(\mathbf{s})\,\mathbf{u} = \mathbf{f}$ is assumed unique for every $\mathbf{s}$. The matrix $\mathbf{K}(\mathbf{s})$ usually does not depend on the design variables directly, but through the material properties, which are interpolated continuously with design variables s_i between two values as:

$$\begin{aligned} \lambda(s_i) &= \left(1 - s_i^\beta\right)\lambda_2 + s_i^\beta \lambda_1 \\ \mu(s_i) &= \left(1 - s_i^\beta\right)\mu_2 + s_i^\beta \mu_1 \\ \rho(s_i) &= \left(1 - s_i^\beta\right)\rho_2 + s_i^\beta \rho_1 \\ 0 &\leq s_i \leq 1 \end{aligned} \tag{3.2}$$

in which β is a parameter that in some situations can help push the design variables toward the end-points (box constraints) $s_i = [0, 1]$. Interpolated material properties allow for a smooth and continuous objective function and is a mathematical construct to allow for the solution of an otherwise discrete problem. As such, it is desirable to minimize the objective such that the design variables are at the box constraints. Such a set of design variables is often referred to as a "0-1" solution, where the physical feasibility is not prevented by the presence of so-called "gray" elements (i.e. those not at the box constraints), the material properties of which do not exist in nature. Assuming the functions z, g_j, and h_k are continuously differentiable for $s_i = [0, 1]$, the corresponding necessary optimality conditions (Karush-Kuhn-Tucker (KKT) conditions) of (3.1) are:

$$\begin{aligned} &\nabla_{\mathbf{s}} z(\mathbf{s}^*) + \textstyle\sum_{j=1}^{n_g} \lambda_j^g \nabla_{\mathbf{s}} g_j(\mathbf{s}^*) + \sum_{k=1}^{n_h} \mu_k^h \nabla_{\mathbf{s}} h_k(\mathbf{s}^*) = 0 \\ &g_j(\mathbf{s}^*) \geq 0 \qquad j = 1 \ldots n_g \\ &h_k(\mathbf{s}^*) = 0 \qquad k = 1 \ldots n_h \\ &\lambda_j^g \leq 0 \qquad j = 1 \ldots n_g \\ &\lambda_j^g g_j(\mathbf{s}^*) = 0 \quad j = 1 \ldots n_g \end{aligned} \tag{3.3}$$

where λ_j^g and μ_k^h are Lagrange multipliers for the inequality and equality constraints, respectively. If the constraints are active they take the value of zero (i.e. $\lambda_j^g < 0$,

$g_j(\mathbf{s}^*) = 0$ and $\mu_k^h \neq 0$, $h_k(\mathbf{s}^*) = 0$), while if they are passive the Lagrange multipliers are zero (i.e. $\lambda_j^g = 0$, $g_j(\mathbf{s}^*) > 0$ and $\mu_k^h = 0$, $h_k(\mathbf{s}^*) \neq 0$).

The algorithms for solving (3.1) in the scope of this dissertation fall into the category of Sequential Convex Programming (SCP). Generally, in these algorithms convex approximations of (3.1) are constructed and solved in an iterative fashion. The general process of an SCP is as follows:

(1) Construct a convex approximation of (3.1) at the current design point $\mathbf{s}_k$.

(2) Solve the convex subproblem for a search direction.

(3) Perform a line search in the search direction to minimize the convex approximation and find a new design point $\mathbf{s}_{k+1}$.

(4) Iterate steps 1 through 3 until $\mathbf{s}_{k+1} \simeq \mathbf{s}_k$ and the KKT conditions (3.3) are met within some tolerance or a maximum number of iterations are exceeded.

Within the structural optimization community, the most common algorithms used to solve (3.1) include the method of moving asymptotes (MMA) [150] and its relative the globally convergent method of moving asymptotes (GCMMA) [151] as well as the SQP algorithm SNOPT [60]. These are the specific algorithms used in this dissertation.

By formulating the objective and constraints as a smooth continuous functions it is possible to use the gradient-based SCP algorithm described above. A prominent and easily recognizable advantage of gradient-based algorithms over discrete methods, such as genetic or branch and bound algorithms, is the drastically smaller number of function evaluations that are needed to solve the optimization problem. This in turn allows for the use of more design variables and finer finite element discretizations, without which the problems solved in this manuscript would be intractable. The caveat of using gradient-based algorithms is that non-convexity is a persistent problem in which any acquired optimal solution may unknowingly be only a local optimum.

3.3.2 Sensitivity analysis

The gradients of both the objective function and the constraints with respect to the design variables must be computed for use in the gradient-based algorithm of choice. The focus here will be on the objective, although the discussion is equally valid for the constraints. There are three methods for evaluating gradients: numerical, analytical, and semi-analytical [157]. Numerical evaluation involves directly evaluating a finite difference approximation of the partial derivatives. When the evaluation of the objective involves a finite element evaluation, this method can become prohibitively computationally expensive because the objective must be calculated at least once more per design variable within each optimization step. For n design variables, this amounts to a minimum of $n+1$ finite element evaluations per optimization step.

The remedy for the expense of calculating numerical gradients is to calculate them analytically or semi-analytically. The analytical gradient of the objective function $z\left(s_i, \mathbf{u}\left(s_i\right)\right)$ can be written as:

$$\frac{dz}{ds_i} = \frac{\partial z}{\partial s_i} + \left(\frac{\partial z}{\partial \mathbf{u}}\right)^T \frac{d\mathbf{u}}{ds_i} \tag{3.4}$$

where s_i are the design variables and $\mathbf{u}$ is the displacement vector. Differentiating the system:

$$\mathbf{K}\mathbf{u} = \mathbf{f} \tag{3.5}$$

w.r.t. the design variables with independent load vector $\mathbf{f}$ yields:

$$\frac{d\mathbf{K}}{ds_i}\mathbf{u} + \mathbf{K}\frac{d\mathbf{u}}{ds_i} = \mathbf{0} \tag{3.6}$$

which can be rearranged to yield:

$$\frac{d\mathbf{u}}{ds_i} = -\mathbf{K}^{-1}\left(\frac{d\mathbf{K}}{ds_i}\mathbf{u}\right) = -\mathbf{K}^{-1}\left(\mathbf{P}_{pseudo}\right) \tag{3.7}$$

where $\mathbf{P}_{pseudo} = \frac{d\mathbf{K}}{ds_i}\mathbf{u}$ is the pseudo load vector. Inserting 3.7 into 3.6 yields:

$$\frac{dz}{ds_i} = \frac{\partial z}{\partial s_i} - \left(\frac{\partial z}{\partial \mathbf{u}}\right)^T \mathbf{K}^{-1}\mathbf{P}_{pseudo}. \tag{3.8}$$

In calculating semi-analytical gradients, the derivatives of the system matrix w.r.t. the design variables in the pseudo load vector are calculated numerically, which is a relatively computationally simple effort. Here, however, fully analytical gradients are used where $\frac{d\mathbf{K}}{ds_i}$ are formulated and calculated explicitly. These partial derivatives may depend on material parameters and/or nodal coordinates, however in this dissertation only material parameters are varied. Notice that the inverse of the system matrix $\mathbf{K}^{-1}$ now appears in the expression for the gradients (3.8). This can reduce the additional computational effort for the gradients when the system matrix $\tilde{\mathbf{K}}$ can be factorized and stored during the evaluation of (3.5). Generally, the factorization is a computationally expensive process for large problems, but when stored any additional computations with the inverse become relatively inexpensive.

From this point there are two methods for finishing the computation of the gradients: directly or via solving the adjoint system. Direct gradient computation solves (3.8) directly by creating a pseudo load vector $\mathbf{P}$ for each design variable, re-solving $\mathbf{K}^{-1}\mathbf{P}_{pseudo}$, and reinserting to find the objective gradients. The disadvantage to this method is that, even when the system $\mathbf{K}$ is already factorized, forward/backward substitutions must be computed for each unique pseudo load vector, the number of which is equal to the number of design variables. Direct gradient computation is therefore efficient only when there are few design variables. It does, however, have advantages with larger numbers of constraints because the pseudo load vector and the corresponding direct solution can be reused for each constraint gradient.

The second method for computing gradients involves solving the adjoint system:

$$\mathbf{K}^T\lambda = -\left(\frac{\partial z}{\partial \mathbf{u}}\right)^T \tag{3.9}$$

for λ and then inserting it into:

$$\frac{dz}{ds_i} = \frac{\partial z}{\partial s_i} + \lambda^T\mathbf{P}_{pseudo}. \tag{3.10}$$

An immediate advantage can be seen here for large numbers of design variables because

the adjoint system is only solved once per gradient evaluation and then only vector-vector products are computed. The disadvantage is that a new adjoint vector must be calculated for each gradient, so for large numbers of constraints this method is less efficient. This is the converse of the direct computation method. The work in this document primarily uses the adjoint computation method because of the large number of design variables and relatively few (if any) constraints in the problems.

This discussion is only valid for real linear systems and modifications must be made for complex-valued systems, which will be discussed in Section (4.2.3). Sensitivities of eigenvalue systems will also be discussed later in Section (5.2.2).

3.3.3 Existing topology optimization design methods

Waveguides

The waveguide design strategy of creating a line defect in a band-gap material is still the primary design method in use today, primarily because they work well and the concept behind their function is easy to understand. These designs, however, still suffer from loss and back-scattering caused by inefficiencies in sharp bends and corners. Without a strict methodology to reduce these inefficiencies, one is resigned to creatively moving and changing the size of inclusions near the bend and analyzing each configuration to find the best performing design. Work reported in a number of studies [14, 53, 85, 86] in photonics have provided an alternate methodology using topology optimization within the local area of a photonic crystal waveguide bend to maximize the efficiency of the device. Similarly, in attacking a different efficiency problem, Frei et al. [55] used topology optimization to adjust the end condition of a photonic crystal waveguide so that they could control the emission properties for a wave exiting the waveguide. A particularly interesting study by Stainko and Sigmund [148] used topology optimization to design a photonic crystal waveguide with a tailored the group velocity with the goal of creating slow light. Tailoring a dispersion diagram in such a way is one

of the primary and most difficult goals of band-gap and waveguide engineering.

Beyond line defect waveguides, there have also been studies in which a whole waveguide structure was designed using topology optimization with no initial design principle such as band-gap materials. The first examples were shown by [146] in which they created phononic waveguides that cause an elastic wave to bend a corner or focus the wave into a smaller location. Frenzel created a number of frequency selective devices akin to multiplexers and demultiplexers [56]. With the goal of dissipating elastic energy rather than reflecting it over a range of frequencies, Jensen [84] used the same techniques with absorptive materials. Larson et al. [100] use topology optimization to design plates that guide flexural wave energy to specific locations on the plate for vibration suppression and control. Notably missing from this group of work are any three-dimensional studies or any including the effects of wave interaction with free surfaces. It should be noted that all of these topology optimization studies involving waveguides used gradient-based algorithms to achieve their optimal solutions.

Band-gap materials

The creation of band-gap materials using the parametric studies noted previously is noticeably restricted by the available topologies and imagination of the engineer. This constraint was relieved when Cox and Dobson [29] used topology optimization and gradient-based algorithms to design the material layout within a two-dimensional photonic crystal unit cell with the objective of maximizing the size of pre-existing band-gaps defined through the dispersion relation. Using this approach they created material layouts that were drastically different from the simple circular and square inclusions that are typically used. Similar procedures with topology optimization were later used to create phononic crystals with maximized band-gaps using gradient-based algorithms [11, 146] as well as genetic algorithms [57, 80]. Rather than in-plane wave propagation, band-gap plate materials were designed and investigated experimentally by Halkjær et al. [68]. A number of studies also designed band-gap materials, not through inducing

changes in the dispersion diagram, but by other methods. Hussein et al. [81, 83] used genetic algorithms to create one-dimensional band-gap materials that tailor dispersion characteristics by maximizing the attenuation or the number and size of band-gaps and pass-bands. Using this method they created designs with various properties such as broadband band-gaps that can isolate shock waves. Hussein et al. [80] has also recently studied the influence of constituent material properties on the optimal design of two-dimensional band-gap materials. So far, optimization of band-gap materials has been limited to one and two dimensions, but three-dimensional band-gap material design using optimization is entirely possible and is sure to seen in the future.

Piezoelectric structures

The use of optimization techniques to design the material layouts of piezoelectric systems for actuation, resonator, or control systems has been studied previously, although topology optimization for vibrating piezoelectric harvesting systems has not yet been studied. For example, Donoso and Bellido [34] use topology optimization to find the polarization layout for piezoelectric plate actuators and sensors, while Abdalla et al. [1] optimize the layout of a compliant mechanism to maximize the efficiency of load transfer from a piezoelectric stack actuator. Other piezoelectric actuator design methodologies using topology optimization have been reported by Carbonari et al. [19, 20], and Drenckhan et al. [36]. Donoso and Sigmund [35] use shape optimization to find thickness and width profiles of piezoelectric layers on a cantilever bi-morph to minimize tip deflections both statically and dynamically. Ha and Cho [66] maximize the piezoelectric coupling strength by finding optimal material layouts for piezoelectric resonators, and Kang and Tong [89, 90] use topology optimization to find the layout of structural and piezoelectric layers, as well as the electric actuation voltages, to control the displacement field of piezoelectric plates. Zheng et al. [164] use topology optimization to maximize mechanical to electrical energy conversion in a static sense for piezoelectric plates, and Elka and Bucher [38] optimally distribute electrodes to tailor

electromechanical modal filtering. Frecker [54] provides a review of some of the earlier uses of optimization with piezoelectric actuators and structures. For control systems, Wang et al. [158] optimize the location of piezoelectric sensors and actuators to control the vibrations of composite plates.

Chapter 4

Topology Optimization of Elastic Waveguides

4.1 Introduction

In this chapter the methodology for the design of elastic waveguides using topology optimization is explored and expanded. While the bulk of the methodology is not new, certain aspects are not well developed or understood. For example, the drivers for design or the influence of free surfaces are aspects of the problem that have not yet been addressed. Also missing from the literature are general guidelines on computational needs for these types of problems as well as issues on mesh dependency and the influence of small feature sizes. The goal of this chapter is to investigate these issues and expand the methodology with new insight into the physical drivers behind the problem. The chapter is organized as follows: the general analysis methodology for time-harmonic problems is presented with explanation of specialized finite elements that are used to simulate infinite boundary conditions that are needed to solve infinite and semi-infinite domain problems. This is followed by a derivation of sensitivity analysis for complex valued time-harmonic problems. Next, verification of the modeling technique and numerous examples of the methodology are given. Deeper investigations into the methodology are then performed, illustrating various unreported aspects of the problem. Finally, a summary of the findings in this chapter is given.

4.2 Analysis

The partial differential equation governing the propagation of waves through an homogeneous or heterogeneous domain has analytical solutions, but only in simplified cases of propagation through homogeneous infinite (Equation (4.6)) and semi-infinite media (see Graff [62]) or through highly structured heterogeneous media (e.g. Bragg gratings or phononic/photonic crystals [87]). General heterogeneous structures, on the other hand, require the use of computational tools.

The analysis tool of choice for the problems presented in this document is the Finite Element Method (FEM) primarily because each individual finite element can be manipulated as a sole entity within the larger system. This is key for using topology optimization as will be seen in a later section. With the exception of a few special element types, which are given special consideration later, common isoparametric plane strain finite elements such as those found in Bathe [6] are used for computation.

4.2.1 Equations of motion

The propagation of waves in an elastic medium is governed by the equations of motion (ignoring body forces):

$$\rho\ddot{\mathbf{u}} = \nabla \cdot \mathbf{T} + \mathbf{f} \tag{4.1}$$

where ρ, $\ddot{(\cdot)}$, $\mathbf{u}$, ∇, $\mathbf{T}$, and $\mathbf{f}$ are the mass density of the material, second derivative with respect to time, displacement vector, gradient operator, stress tensor, and vector of traction forces, respectively. The stress tensor is related to the strain tensor $\mathbf{S}$ through the constitutive equation:

$$\mathbf{T} = \mathbf{c} : \mathbf{S} \tag{4.2}$$

where $\mathbf{c}^E$ is the elastic stiffness tensor, and the strain tensor is related to the displacement vector through the kinematic relationship:

$$\mathbf{S} = \frac{1}{2}\left(\nabla\mathbf{u} + (\nabla\mathbf{u})^T\right) \tag{4.3}$$

with $(\cdot)^T$ being the transpose operator. For an isotropic medium, the material properties can be reduced to three constants: material density ρ, and two of the many forms of the elastic constants. In wave propagation it is customary to represent the elastic constants in terms of the Lamé coefficients λ and μ, which are related to the better known elastic modulus E and Poisson's ratio ν through the equations:

$$\begin{aligned} \lambda &= \frac{E\nu}{(1+\nu)(1-2\nu)} \\ \mu &= \frac{E}{2(1+\nu)} \end{aligned}. \tag{4.4}$$

For wave propagation through an homogeneous isotropic medium, the reduction in the elastic stiffness tensor allows for simplification of equations (4.1), (4.2), and (4.3) to Navier's equations with forcing term:

$$\rho\ddot{\mathbf{u}}\left(\mathbf{x},t\right) = (\lambda+\mu)\nabla\nabla\cdot\mathbf{u}\left(\mathbf{x},t\right) + \mu\nabla^2\mathbf{u}\left(\mathbf{x},t\right) + \mathbf{f}\left(\mathbf{x},t\right) \tag{4.5}$$

with the displacement vector $\mathbf{u}$ and traction forces $\mathbf{f}$ a function of the location vector $\mathbf{x}$ and time t. The general solution to this set equations can be represented as a superposition of forward and backward traveling plane waves commonly known as the d'Alembert solution which takes the form:

$$\mathbf{u}\left(\mathbf{x},t\right) = \mathbf{A}_r\, f\left(\hat{\mathbf{n}}\cdot\mathbf{x} - ct\right) + \mathbf{A}_l\, f\left(\hat{\mathbf{n}}\cdot\mathbf{x} + ct\right) \tag{4.6}$$

where $f\left(\cdot\right)$ is a function of the propagation direction $\hat{\mathbf{n}}$, the spatial location vector, the wavespeed c, and time, while $\mathbf{A}_r$ and $\mathbf{A}_l$ are component vectors corresponding to the amplitudes of the forward (or rightward) and backward (or leftward) travelling plane waves, respectively. The specific form of $f\left(\cdot\right)$ depends on the mode of propagation, which are described in more detail in the following section.

4.2.2 Time-harmonic wave propagation problems

General wave propagation analysis requires the solution of the equations of motion in both space and time, but in many cases this is unnecessary or even prohibitive as

time-stepping algorithms can be computationally expensive. Analyses of linear systems can be simplified by solving in the frequency domain with a single excitation/response frequency ω. In doing so, the forcing function and displacements can be defined in complex notation as:

$$\mathbf{f}(\mathbf{x}, t) = \mathbf{f}(\mathbf{x})\ e^{i\omega t} \tag{4.7}$$

$$\mathbf{u}(\mathbf{x}, t) = \mathbf{u}(\mathbf{x})\ e^{i\omega t} \tag{4.8}$$

where i represents the imaginary unit. Inserting (4.7) and (4.8) into the wave equation (4.5) results in the time-harmonic wave equation:

$$\nabla(\lambda + \mu)\nabla \cdot \mathbf{u}(\mathbf{x}) + \mu\nabla^2\mathbf{u}(\mathbf{x}) + \omega^2\rho\mathbf{u}(\mathbf{x}) + \mathbf{f}(\mathbf{x}) = 0 \tag{4.9}$$

which is no longer a function of time. The weak form of this equation is written as:

$$\int_\Omega v \cdot \nabla(\lambda + \mu)\nabla \cdot \mathbf{u}(\mathbf{x}) + \mu\mathbf{v} \cdot \nabla^2\mathbf{u}(\mathbf{x}) + \omega^2\rho\mathbf{v} \cdot \mathbf{u}(\mathbf{x}) + \mathbf{v} \cdot \mathbf{f}(\mathbf{x})\, d\Omega = 0 \tag{4.10}$$

with test function $\mathbf{v}$ and integrated over the domain Ω. Using the Galerkin method, equation (4.10) can be discretized into a system of finite elements such that:

$$\left(\mathbf{K} - \omega^2\mathbf{M}\right)\mathbf{u} = \mathbf{f} \tag{4.11}$$

with global stiffness matrix $\mathbf{K}$ and global mass matrix $\mathbf{M}$, and is solved in complex-space for a phase-dependent forcing function $\mathbf{f}$. It is often necessary to include velocity proportional damping into the formulation, whether as material damping or as a boundary condition, which changes (4.11) into:

$$\left(\mathbf{K} + i\omega\mathbf{C} - \omega^2\mathbf{M}\right)\mathbf{u} = \mathbf{f} \tag{4.12}$$

with damping matrix $\mathbf{C}$. The form of these matrices (with the exception of the mass matrix as addressed later) can be found in a number of finite element references (e.g. Bathe [6]). The finite element method allows for variation in material properties on a per-element basis, so that while each element is homogeneous the material domain

described by (4.12) can be heterogeneous, an important feature when combined with topology optimization as will be shown later.

Mass matrix for wave propagation

There exist two methods for representing the mass matrix for a finite element, namely, the consistent and lumped mass matrices. The consistent mass matrix arises from integrating the density over the element domain in the same manner as is done for the stiffness matrix. For the lumped mass matrix, however, the terms of the consistent mass matrix are "lumped" onto the diagonal of the matrix. With respect to wave propagation, it has been shown by Belytschko and Mullen [9] that neither matrix accurately models wavespeed where the consistent mass matrix produces a wavespeed that is too high and the lumped mass matrix too low. Belytschko and Mullen additionally showed that an equally weighted average of the two matrices accurately models the wavespeed. It is this averaged mass matrix that is used for solving wave propagation problems in this document. When solving band-gap material problems, however, the lumped mass matrix is used as is customary with modal analysis problems of which this type of problem is closely related.

Non-reflecting boundary conditions

For time-harmonic wave propagation problems, it is often necessary to model more than the finite domain of interest through which a wave would travel. A finite domain works for time marching wave propagation problems where one can stop the simulation when the wavefront reaches a computational boundary for a sufficiently large computational domain, but for time harmonic problems the wavefield throughout the whole domain is calculated at once and boundary interactions are important. Therefore, boundary conditions that model the infinite domain without reflection are needed. Many methods exist for implementing so-called infinite or absorbing or non-reflecting boundary conditions including enclosing the finite element domain in boundary elements [15], doubly asymptotic expansions [58], viscous damping elements (discussed here), and

Perfectly Matched Layer (PML) elements (discussed in the next sub-section). A review of some of these methods as applied to time-harmonic acoustic problems can be found in [69].

The viscous damping elements of Lysmer and Kuhlemeyer [107] are formulated to damp out waves at a boundary and minimize the reflection at that boundary. The reflection is minimized by matching the damping coefficient to the incident wavespeed, propagation direction, and propagation mode. An underlying assumption of the method is that waves reach the interface at normal incidence. In this case the longitudinal wave displaces normal to the surface and so damping coefficients in that direction are matched to the longitudinal wavespeed and likewise for the shear wave where displacements are parallel to the surface. It is immediately apparent that for waves at other angles of incidence, the damping coefficients are not properly matched and so some reflection of the wave will occur. The reflection is still sufficiently small, however, with at least 96.5% of longitudinal and 89% of shear wave energy being damped out within 60 degrees of normal incidence.

Perfectly Matched Layers (PMLs)

To correct for the shortcomings of viscous damping elements without succumbing to the expense of boundary elements, one can use Perfectly Matched Layer elements (PMLs). Analytically, PMLs are perfect, but once discretized this is not true, although the error remains small and independent of angle of incidence. PMLs were first introduced by Bérenger [12] for electromagnetic wave problems and later by Chew and Weedon for elastodynamics [25]. PMLs work on the idea that the coordinates within a layer at the edge of computational domain are "stretched" to infinity so as to approximate an infinite boundary [25]. A finite element implementation, however, was not presented for elastodynamics until Basu and Chopra [5], who perform the coordinate stretching by modifying the shape function matrices in the finite element formulation. Zheng and Huang [165] and Harari and Albocher [70] provide a different approach where

the coordinate stretching occurs in the constitutive matrix, resulting in an element with complex-valued anisotropic material properties. Both approaches perform equally well, and use the same stretching function, but the anisotropic PMLs are much easier to implement. The work in this dissertation uses these anisotropic PML elements with parameters guided by the investigations of Harari and Albocher [70] and Basu and Chopra [5]. Specifically, the PMLs are typically 10 element layers deep with a stretching function ψ of the form:

$$\psi(x) = 1 - is_{max}\left(\frac{x}{L}\right)^2 \tag{4.13}$$

where x is the distance from the domain-PML interface to the element center, L is the total thickness of the PMLs, and s_{max} is the maximum attenuation coefficient which is given a empirical value of 10.

4.2.3 Sensitivity analysis for complex-valued time-harmonic problems

For a complex-valued, time-harmonic, linear system the objective sensitivities are re-derived here. The original time-harmonic system (4.12) can be written as:

$$\left(\mathbf{K} + i\omega\mathbf{C} - \omega^2\mathbf{M}\right)\mathbf{u} - \mathbf{f} = \tilde{\mathbf{K}}\mathbf{u} - \mathbf{f} = \mathbf{0} \tag{4.14}$$

where $\tilde{\mathbf{K}}$ is the system matrix to be factorized for a given frequency. The real and imaginary parts can be disassociated such that $\tilde{\mathbf{K}} = \mathbf{K}_\mathrm{r} + i\mathbf{K}_\mathrm{i}$ and $\mathbf{u} = \mathbf{u}_\mathrm{r} + i\mathbf{u}_\mathrm{i}$, where $(\cdot)_r$ and $(\cdot)_i$ are the real and imaginary parts, respectively, and the complex system (4.14) can be equivalently written as the real system:

$$\begin{bmatrix} \mathbf{K}_\mathrm{r} & -\mathbf{K}_\mathrm{i} \\ \mathbf{K}_\mathrm{i} & \mathbf{K}_\mathrm{r} \end{bmatrix} \begin{pmatrix} \mathbf{u}_\mathrm{r} \\ \mathbf{u}_\mathrm{i} \end{pmatrix} - \begin{pmatrix} \mathbf{f}_\mathrm{r} \\ \mathbf{f}_\mathrm{i} \end{pmatrix} = \mathbf{0}. \tag{4.15}$$

The gradient of the objective function $z(s_i, \mathbf{u}(s_i))$ with respect to the design variables s_i can be written using the chain rule:

$$\frac{dz}{ds_i} = \frac{\partial z}{\partial s_i} + \begin{pmatrix} \frac{\partial z}{\partial \mathbf{u}_\mathrm{r}} \\ \frac{\partial z}{\partial \mathbf{u}_\mathrm{i}} \end{pmatrix}^T \begin{pmatrix} \frac{d\mathbf{u}_\mathrm{r}}{ds_i} \\ \frac{d\mathbf{u}_\mathrm{i}}{ds_i} \end{pmatrix}. \tag{4.16}$$

Using the adjoint method described in [157], one can create an augmented objective function:

$$z_0 = z + \begin{pmatrix} \lambda_\mathrm{r} \\ \lambda_\mathrm{i} \end{pmatrix}^T \left(\begin{bmatrix} \mathbf{K}_\mathrm{r} & -\mathbf{K}_\mathrm{i} \\ \mathbf{K}_\mathrm{i} & \mathbf{K}_\mathrm{r} \end{bmatrix} \begin{pmatrix} \mathbf{u}_\mathrm{r} \\ \mathbf{u}_\mathrm{i} \end{pmatrix} - \begin{pmatrix} \mathbf{f}_\mathrm{r} \\ \mathbf{f}_\mathrm{i} \end{pmatrix} \right) \tag{4.17}$$

where λ is a vector of complex Lagrange multipliers. The augmented objective function (4.17) is equivalent to the original objective because the added terms from (4.15) are equal to zero. Taking the derivative of (4.17) and letting $(\cdot)' = \frac{d(\cdot)}{ds_i}$ while assuming that the load is independent of the design variables results in:

$$\begin{aligned} \tfrac{dz_0}{ds_i} = \quad & \tfrac{\partial z}{\partial s_i} + \begin{pmatrix} \frac{\partial z}{\partial \mathbf{u}_\mathrm{r}} \\ \frac{\partial z}{\partial \mathbf{u}_\mathrm{i}} \end{pmatrix}^T \begin{pmatrix} \mathbf{u}'_\mathrm{r} \\ \mathbf{u}'_\mathrm{i} \end{pmatrix} \\ & + \begin{pmatrix} \lambda_\mathrm{r} \\ \lambda_\mathrm{i} \end{pmatrix}^T \left(\begin{bmatrix} \mathbf{K}'_\mathrm{r} & -\mathbf{K}'_\mathrm{i} \\ \mathbf{K}'_\mathrm{i} & \mathbf{K}'_\mathrm{r} \end{bmatrix} \begin{pmatrix} \mathbf{u}_\mathrm{r} \\ \mathbf{u}_\mathrm{i} \end{pmatrix} + \begin{bmatrix} \mathbf{K}_\mathrm{r} & -\mathbf{K}_\mathrm{i} \\ \mathbf{K}_\mathrm{i} & \mathbf{K}_\mathrm{r} \end{bmatrix} \begin{pmatrix} \mathbf{u}'_\mathrm{r} \\ \mathbf{u}'_\mathrm{i} \end{pmatrix} \right) \end{aligned} . \tag{4.18}$$

Rearranging gives:

$$\begin{aligned} \tfrac{dz_0}{ds_i} = \quad & \tfrac{\partial z}{\partial s_i} + \begin{pmatrix} \lambda_\mathrm{r} \\ \lambda_\mathrm{i} \end{pmatrix}^T \begin{bmatrix} \mathbf{K}'_\mathrm{r} & -\mathbf{K}'_\mathrm{i} \\ \mathbf{K}'_\mathrm{i} & \mathbf{K}'_\mathrm{r} \end{bmatrix} \begin{pmatrix} \mathbf{u}_\mathrm{r} \\ \mathbf{u}_\mathrm{i} \end{pmatrix} \\ & + \left\{ \begin{pmatrix} \frac{\partial z}{\partial \mathbf{u}_\mathrm{r}} \\ \frac{\partial z}{\partial \mathbf{u}_\mathrm{i}} \end{pmatrix}^T + \begin{pmatrix} \lambda_\mathrm{r} \\ \lambda_\mathrm{i} \end{pmatrix}^T \begin{bmatrix} \mathbf{K}_\mathrm{r} & -\mathbf{K}_\mathrm{i} \\ \mathbf{K}_\mathrm{i} & \mathbf{K}_\mathrm{r} \end{bmatrix} \right\} \begin{pmatrix} \mathbf{u}'_\mathrm{r} \\ \mathbf{u}'_\mathrm{i} \end{pmatrix} \end{aligned} \tag{4.19}$$

where the Lagrange multipliers are arbitrary and can be selected to make the expression in the braces equal zero such that:

$$\frac{dz_0}{ds_i} = \frac{\partial z}{\partial s_i} + \begin{pmatrix} \lambda_\mathrm{r} \\ \lambda_\mathrm{i} \end{pmatrix}^T \begin{bmatrix} \mathbf{K}'_\mathrm{r} & -\mathbf{K}'_\mathrm{i} \\ \mathbf{K}'_\mathrm{i} & \mathbf{K}'_\mathrm{r} \end{bmatrix} \begin{pmatrix} \mathbf{u}_\mathrm{r} \\ \mathbf{u}_\mathrm{i} \end{pmatrix} = \frac{\partial z}{\partial s_i} + Re\left(\lambda^* \tilde{\mathbf{K}}' \mathbf{u}\right) \tag{4.20}$$

and

$$\begin{pmatrix} \lambda_\mathrm{r} \\ \lambda_\mathrm{i} \end{pmatrix}^T \begin{bmatrix} \mathbf{K}_\mathrm{r} & -\mathbf{K}_\mathrm{i} \\ \mathbf{K}_\mathrm{i} & \mathbf{K}_\mathrm{r} \end{bmatrix} = -\left(\frac{\partial z}{\partial \mathbf{u}_\mathrm{r}} + i \frac{\partial z}{\partial \mathbf{u}_\mathrm{i}} \right)^T \tag{4.21}$$

after which taking the transpose results in:

$$\begin{bmatrix} \mathbf{K}_\mathrm{r} & \mathbf{K}_\mathrm{i} \\ -\mathbf{K}_\mathrm{i} & \mathbf{K}_\mathrm{r} \end{bmatrix} \begin{pmatrix} \lambda_\mathrm{r} \\ \lambda_\mathrm{i} \end{pmatrix} = \tilde{\mathbf{K}}^* \lambda = -\left(\frac{\partial z}{\partial \mathbf{u}_\mathrm{r}} + i \frac{\partial z}{\partial \mathbf{u}_\mathrm{i}} \right). \tag{4.22}$$

Taking the conjugate of (4.22) results in the adjoint system:

$$\tilde{\mathbf{K}}^T\bar{\lambda} = -\left(\frac{\partial z}{\partial \mathbf{u}_\mathrm{r}} - i\frac{\partial z}{\partial \mathbf{u}_\mathrm{i}}\right) \tag{4.23}$$

for which if the system $\tilde{\mathbf{K}}$ is symmetric (i.e. $\tilde{\mathbf{K}}^T = \tilde{\mathbf{K}}$) then one can find $\bar{\lambda}$ from:

$$\tilde{\mathbf{K}}\bar{\lambda} = -\left(\frac{\partial z}{\partial \mathbf{u}_\mathrm{r}} - i\frac{\partial z}{\partial \mathbf{u}_\mathrm{i}}\right). \tag{4.24}$$

Solving for $\bar{\lambda}$ and inserting into (4.20) gives an expression for the gradient of the objective:

$$\frac{dz_0}{ds_i} = \frac{\partial z}{\partial s_i} - Re\left(\left(\frac{\partial z}{\partial \mathbf{u}_\mathrm{r}} - i\frac{\partial z}{\partial \mathbf{u}_\mathrm{i}}\right)^T \tilde{\mathbf{K}}^{-1}\frac{\partial \tilde{\mathbf{K}}}{\partial s_i}\mathbf{u}\right) \tag{4.25}$$

for which the partial derivatives of the system matrix can be written as:

$$\frac{\partial \tilde{\mathrm{K}}}{\partial s_i} = \sum_n \left(\frac{\partial \mathrm{K}_e}{\partial s_i} + i\omega\frac{\partial \mathrm{C}_e}{\partial s_i} - \omega^2\frac{\partial \mathrm{M}_e}{\partial s_i}\right) \tag{4.26}$$

where the partial derivatives can be evaluated on the n element matrices K_e, $\mathbf{C}_e$, and $\mathbf{M}_e$ and summed to create the global matrix.

4.3 Verification

Presented here are two verification examples showing that wave propagation in elastic structures is being properly modeled by the finite element implementation.

4.3.1 Material properties

The properties of materials used in this chapter are given in Table 4.1.

Table 4.1: Material Properties

Material	E-Elastic Modulus (GPa)	ν-Poisson's ratio	ρ-Density (kg/m^3)
Silicon	162.9	0.2226	2331
Aluminum	70.38	0.3454	2697

4.3.2 Pressure and shear wave propagation

Model verification for bulk waves is performed using a silicon computational domain of length 0.05 m and height 0.01 m with a 558x111 element mesh. Periodic boundary conditions are used on the top and bottom while non-reflecting boundary conditions are used at the left and right boundaries. A harmonic displacement of unit magnitude is applied to the left boundary in the right direction for the pressure wave verification case and in the vertical direction for the shear wave case. The displacement fields and a plot of displacements vs. length for the finite elements and the analytical solution are shown in Figure 4.1 for both the pressure and shear wave cases. The numerical results show excellent agreement with the analytical solution.

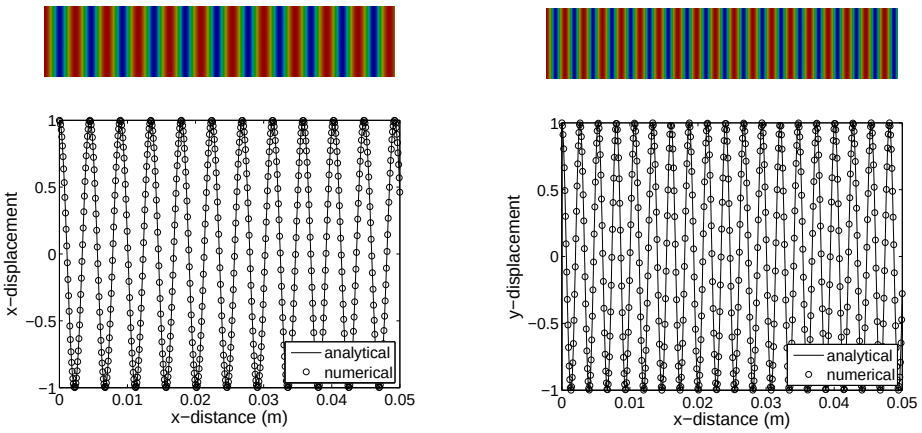

(a) (b)

Figure 4.1: Verification of bulk wave propagation. (top) Wavefield and (bottom) comparison with analytical results for (a) pressure waves and (b) shear waves.

4.3.3 Rayleigh wave propagation

Verification of Rayleigh wave propagation is performed using a computational domain of 0.1m length and 0.025m height with a 500x250 element mesh surrounded by PMLs 10 elements thick on the bottom and two sides. The top surface is free to

accommodate the surface wave. A Rayleigh wave is introduced on the left side inside the PMLs through appropriately varying harmonic displacements through the thickness. Figure 4.2 shows the wavefields for both displacement directions and a comparison with the analytical solution provided by Graff [62], which is in good agreement.

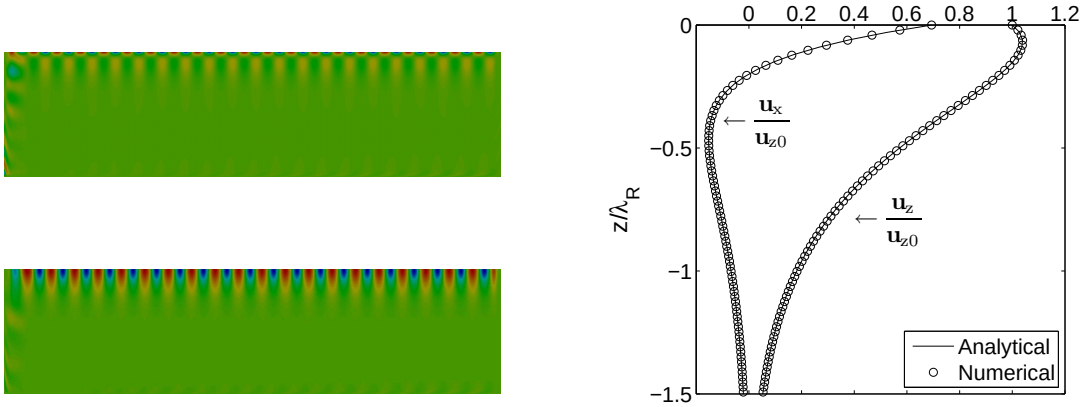

(a) (b)

Figure 4.2: (a) Wavefields for displacements in (top) x-direction and (bottom) y-direction. (b) Comparison of analytical and numerical solutions for Rayleigh wave propagation.

4.4 Applications

In this section a number of examples are presented for the design of waveguide structures using topology optimization. In general for waveguides it is desirable to have most or all of the incoming wave energy reach the end of the waveguide. To this end, two objective functions are used. The first is formulated as the complex displacement norm, which is related to the propagating energy. The second objective is the Poynting vector, a direct measure of the energy flow of a propagating wave. The following time-harmonic wave propagation examples and studies in the following section make use of

one of these two objective functions.

4.4.1 Objective functions and sensitivities

Displacement-based objective function

The displacement-based objective function is the same as that used in [11, 56, 146]. It is formulated as:

$$z = \sum_j \alpha_j |u_j|^2 = \mathbf{u}^* \mathbf{L} \mathbf{u} \tag{4.27}$$

where $\mathbf{L}$ is a diagonal matrix with non-zero entries $\alpha_j \in \Re$ corresponding to the degree(s) of freedom where the displacement norm is to be minimized ($\alpha_j > 0$) or maximized ($\alpha_j < 0$). From equation (4.25), it remains to find the gradient of the objective with respect to the design variables $\frac{\partial z}{\partial s_i}$ and the displacements $\frac{\partial z}{\partial \mathbf{u}_\mathrm{r}}$ and $\frac{\partial z}{\partial \mathbf{u}_\mathrm{i}}$. For this objective $\frac{\partial z}{\partial s_i} = 0$, and after a little math it can be shown that $\frac{\partial z}{\partial \mathbf{u}_\mathrm{r}} = 2\mathbf{L}\mathbf{u}_\mathrm{r}$ and $\frac{\partial z}{\partial \mathbf{u}_\mathrm{i}} = 2\mathbf{L}\mathbf{u}_\mathrm{i}$. It then follows that the gradient of the objective can be written as:

$$\frac{dz_0}{ds_i} = -2Re\left(\mathbf{u}^* \mathbf{L} \tilde{\mathbf{K}}^{-1} \frac{\partial \tilde{\mathbf{K}}}{\partial s_i} \mathbf{u}\right) \tag{4.28}$$

which can be solved using either the direct or adjoint method. Because the coefficients α_j operate on individual degrees of freedom then the displacement components can be minimized or maximized separately, a method commonly used in the following examples.

Poynting vector-based objective function

The Poynting vector $\mathbf{P}$ is a vector of wave energy flux and is written as:

$$\mathbf{P} = -\frac{1}{2} \dot{\mathbf{u}}^* \mathbf{T} \tag{4.29}$$

where $\mathbf{u}$ is a vector of displacements $\mathbf{u} = (u_x, u_y, u_z)^T$, $(\cdot)^*$ is the complex conjugate transpose, $\dot{(\cdot)}$ is differentiation w.r.t. time, and $\mathbf{T}$ is the stress tensor written as:

$$\mathbf{T} = \begin{bmatrix} T_{xx} & T_{xy} & T_{xz} \\ T_{yx} & T_{yy} & T_{yz} \\ T_{zx} & T_{zy} & T_{zz} \end{bmatrix}. \tag{4.30}$$

One can use the vector components of the Poynting vector to create a scalar objective function such as energy flux in a particular direction. Assuming time-harmonicity and re-writing (4.29) in terms of the real and imaginary parts as:

$$\mathbf{P} = -\frac{1}{2} i\omega \left(\mathbf{u}_\mathrm{r} \mathbf{T}_\mathrm{r} + i\mathbf{u}_\mathrm{r} \mathbf{T}_\mathrm{i} - i\mathbf{u}_\mathrm{i} \mathbf{T}_\mathrm{r} + \mathbf{u}_\mathrm{i} \mathbf{T}_\mathrm{i} \right) \tag{4.31}$$

allows for the use of equation (4.25) to calculate its gradients. In the finite element formulation the stress tensor can be written as a function of the displacements:

$$\mathbf{T} = \mathbf{cBu} \tag{4.32}$$

where $\mathbf{c}$ is the constitutive tensor and $\mathbf{B}$ is the strain-displacement matrix. Writing this in terms of the real and imaginary parts as:

$$\mathbf{T} = \mathbf{T}_\mathrm{r} + i\mathbf{T}_\mathrm{i} = \mathbf{cBu}_\mathrm{r} + i\mathbf{cBu}_\mathrm{i} \tag{4.33}$$

shows that $\frac{\partial \mathbf{T}_\mathrm{r}}{\partial \mathbf{u}_\mathrm{i}} = \frac{\partial \mathbf{T}_\mathrm{i}}{\partial \mathbf{u}_\mathrm{r}} = 0$, $\frac{\partial \mathbf{T}_\mathrm{r}}{\partial \mathbf{u}_\mathrm{r}} = \mathbf{cB}\vec{\mathbf{I}}$, and $\frac{\partial \mathbf{T}_\mathrm{i}}{\partial \mathbf{u}_\mathrm{i}} = i\mathbf{cB}\vec{\mathbf{I}}$ where $\vec{\mathbf{I}}$ is a vector of ones the size of the displacement vector. Differentiating (4.31) w.r.t. the real and imaginary displacement vectors results in:

$$\begin{aligned}
\frac{d\mathbf{P}}{d\mathbf{u}_\mathrm{r}} &= -\tfrac{1}{2} i\omega \left(\mathbf{T}_\mathrm{r} + i\mathbf{T}_\mathrm{i} + \mathbf{u}_\mathrm{r} \tfrac{\partial \mathbf{T}_\mathrm{r}}{\partial \mathbf{u}_\mathrm{r}} - i\mathbf{u}_\mathrm{i} \tfrac{\partial \mathbf{T}_\mathrm{r}}{\partial \mathbf{u}_\mathrm{r}} \right) = -\tfrac{1}{2} i\omega \left(\mathbf{T} + \mathbf{u}^* \tfrac{\partial \mathbf{T}_\mathrm{r}}{\partial \mathbf{u}_\mathrm{r}} \right) \\
&= -\tfrac{1}{2} i\omega \left(\mathbf{T} + \mathbf{u}^* \mathbf{cB}\vec{\mathbf{I}} \right) \\
i\frac{d\mathbf{P}}{d\mathbf{u}_\mathrm{i}} &= -\tfrac{1}{2} i\omega \left(\mathbf{T}_\mathrm{r} + i\mathbf{T}_\mathrm{i} - \mathbf{u}_\mathrm{r} \tfrac{\partial \mathbf{T}_\mathrm{i}}{\partial \mathbf{u}_\mathrm{i}} + i\mathbf{u}_\mathrm{i} \tfrac{\partial \mathbf{T}_\mathrm{i}}{\partial \mathbf{u}_\mathrm{i}} \right) = -\tfrac{1}{2} i\omega \left(\mathbf{T} - \mathbf{u}^* \tfrac{\partial \mathbf{T}_\mathrm{r}}{\partial \mathbf{u}_\mathrm{r}} \right) \\
&= -\tfrac{1}{2} i\omega \left(\mathbf{T} - i\mathbf{u}^* \mathbf{cB}\vec{\mathbf{I}} \right)
\end{aligned} \tag{4.34}$$

for which:

$$\left(\frac{d\mathbf{P}}{d\mathbf{u}_\mathrm{r}} - i\frac{d\mathbf{P}}{d\mathbf{u}_\mathrm{i}} \right) = -\frac{1}{2} i\omega \mathbf{u}^* \mathbf{cB} \left(1 + i \right) \vec{\mathbf{I}}. \tag{4.35}$$

Taking the partial derivative of the Poynting vector w.r.t. the design variables yields:

$$\frac{\partial \mathbf{P}}{\partial s_i} = -\frac{1}{2} i\omega \mathbf{u}^* \frac{d\mathbf{T}}{ds_i} = -\frac{1}{2} i\omega \mathbf{u}^* \frac{d\mathbf{c}}{ds_i} \mathbf{Bu}. \tag{4.36}$$

Combining equation (4.25) with the expressions (4.35) and (4.36) results in the following analytical expression for the gradients of the Poynting vector objective function:

$$\frac{d\mathbf{P}}{ds_i} = -\frac{1}{2} i\omega \mathbf{u}^* \frac{d\mathbf{c}}{ds_i} \mathbf{Bu} - Re \left(\left(-\frac{1}{2} i\omega \mathbf{u}^* \mathbf{cB} \left(1 + i \right) \vec{\mathbf{I}} \right) \tilde{\mathbf{K}}^{-1} \frac{\partial \tilde{\mathbf{K}}}{\partial s_i} \mathbf{u} \right). \tag{4.37}$$

4.4.2 Examples

Bulk wave in-plane bending waveguide

The design setup for a bending waveguide problem for in-plane bulk waves is shown in Figure 4.3a. An incoming elastic wave of frequency 2.8MHz enters the 1 cm square domain from a 2 mm port on the left boundary. A material layout of silicon and aluminum is sought such that a wave with only displacements normal to the exit surface will leave a 2 mm port located at the bottom of the domain. The objective is formulated so that vertical displacement norms are maximized while horizontal are minimized. Viscous damping non-reflecting boundary conditions are used along all boundaries. The domain is discretized into 400x400 elements. As is the case for all examples in this chapter, a linear material interpolation and no filtering is used.

The optimal silicon/aluminum material layout needed to form the waveguide is shown in Figure 4.3b. Figures 4.3c, d, e show the wavefields that results if the design domain consists of either a homogeneous material or the final design. As expected in the homogeneous design, the wavefield radiates from the source and is dissipated at the absorbing boundaries. In the optimal design, however, the waves clearly are focused toward the exit location. Similar to the results of Sigmund and Jensen [146] for scalar acoustics problems, the resulting material shows a bent striated structure that resembles a curved Bragg grating. This design has an energy efficiency of 94.8% based on integrating the Poynting vector along the input and output ports. Removing the "gray" elements from the final design by thresholding design variables at a value of 0.5 results in a change in objective of 0.27%, indicating that the unconverged regions do not have much influence on the operation of the device. Given the symmetric nature of the problem, it would be expected that the material layout would also be symmetric. This, however, does not occur because the displacements at the exit port are not constrained to mirror those of the input port.

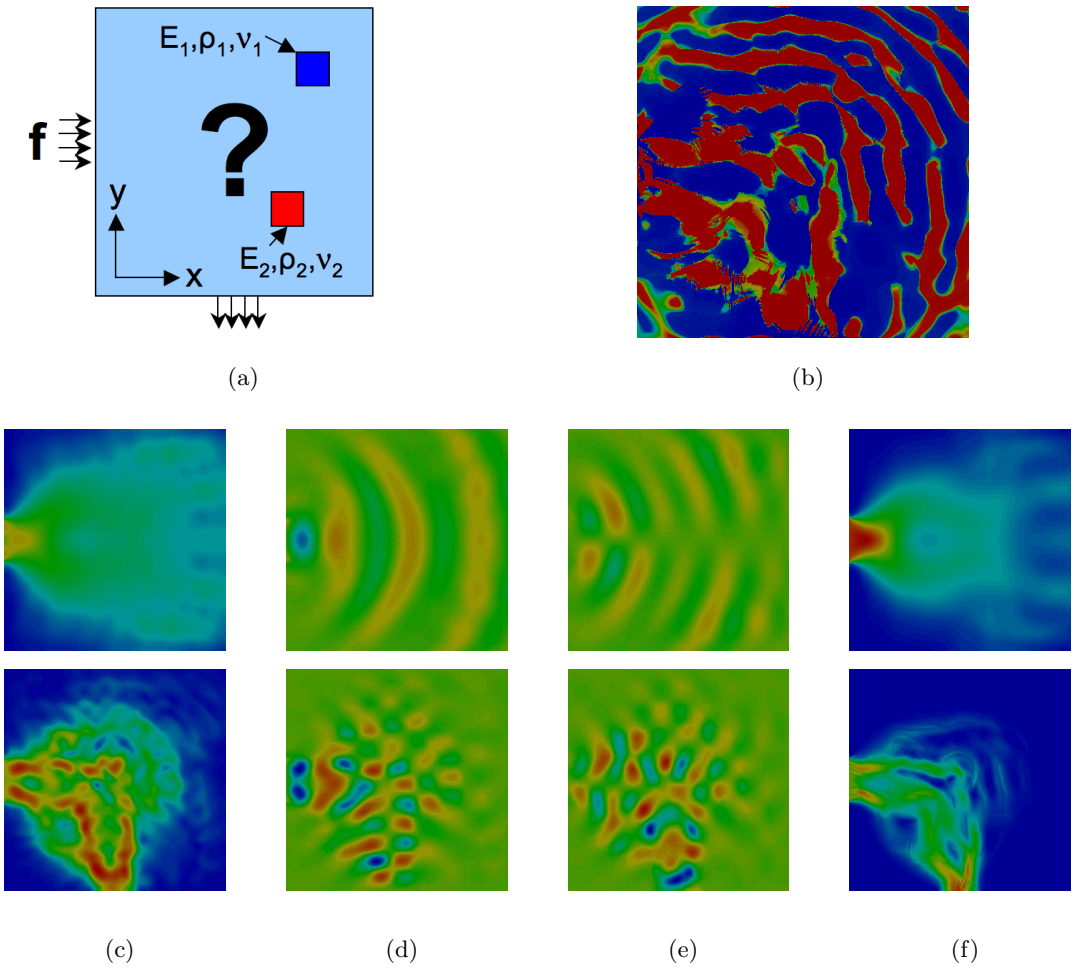

Figure 4.3: Topology optimization problem of an in-plane waveguide which bends an incoming pressure wave around a 90° bend. (a) Problem setup and (b) final material distribution of silicon (blue) and aluminum (red). Wavefield in (top) a homogeneous material and (bottom) the final design for the (c) complex norm magnitude, (d) real x-displacements, (e) real y-displacements, and (f) Poynting vector magnitude.

P-wave to S-wave mode converter

A curious unsolved wave propagation problem is to design a device that can perform full mode conversion of a pressure wave into a shear wave or vice-versa. While there is no other known solution to this problem, topology optimization provides a method of accomplishing this task. The setup for this problem consists of a 1cm x 1cm

domain of silicon and aluminum surrounded by viscous damping non-reflecting boundary conditions with a pressure wave excited at a 2mm port on the left side. The domain is discretized by a 150x150 element mesh with an initial design of an homogeneous material at the midpoint of the design space. The objective is formulated so that the vertical displacement norms are maximized while the horizontal are minimized at a 2mm output port on the right side of the domain. This effectively maximizes the shear wave component and minimizes the pressure wave component at the output. The results of this problem can be seen in Figure 4.4, which shows the final design and the horizontal and vertical complex norm wavefields. This problem also has a peculiar feature in that the optimization landscape seems to be symmetric, a feature that is discussed more in section 4.5.4.

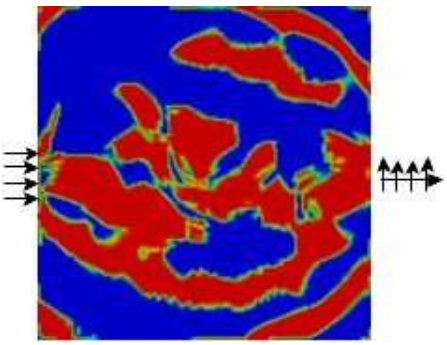

(a)

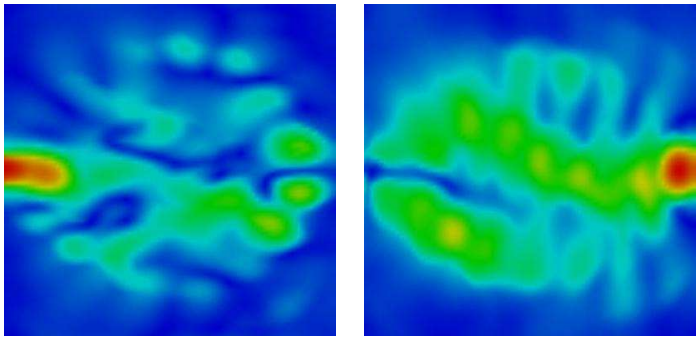

(b) (c)

Figure 4.4: (a) Final design of a pressure to shear wave mode converter composed of silicon (blue) and aluminum (red). It can be inferred through the complex norm plots for the (b) horizontal direction and (c) vertical direction that a pressure wave enters the domain at the left but a shear wave exits the domain at the right.

Three-dimensional surface wave focuser

The idea behind the design of a three-dimensional surface wave focuser is to transfer the energy created by a surface load into surface waves that are focused in a single direction. The design setup for this problem is shown in Figure 4.5a. The three-dimensional half space is created by surrounding a 1cm x 1cm x 2.5mm domain of 72000 eight-node brick elements by viscous damping boundary conditions on all sides except the top, which is free. Every element in the computational domain is assigned a design variable and viscous damping boundary condition elements have their material properties tied to their adjacent elements. A 1.6 MHz vertical harmonic load on a small

area (source) at the center of the top surface introduces wave energy into the domain. A material layout of silicon and aluminum is sought that focuses the surface wave to a small exit (output) region on the top surface. The objective function is posed in the usual manner (4.27) such that the displacements are maximized at a set of nodes (L) at the edge of the computational domain where the free surface meets the non-reflecting boundary conditions. The surface wave magnitude will then be maximized at this location.

The resulting material layout is shown in Figure 4.5b where it is visualized in the form of material isosurfaces. The isosurfaces are located where the material gradient is the largest, i.e. at material interfaces. The isosurfaces show a complex material layout throughout the domain, although there are some recognizable features. The materials tend to order like an alternating array of hyperbolic mirrors focusing the waves in one direction in a manner similar to how a headlamp focuses light. The wave fields in a homogeneous and the optimized material layout domains, Figures 4.5c and 4.5d respectively, suggest that this is a reasonable analogy. In the optimized structure, the surface waves, which in the homogeneous material propagate radially outward from the source, are strongly focused along the surface to the output location and out of the computational domain.

In studying this problem further, it is investigated whether the wavefield is significantly affected by the removal of gray elements by setting the design variables to a full "0-1" solution. To do this all design variables in the final solution at or below 0.5 are set to 0 and above 0.5 are set to 1. Removing gray elements results in a very small change in objective of about 0.3%. This not only shows that the solution is well converged but also that the solution is relatively insensitive to the presence of gray elements. In another study, the efficiency of the optimized structure with regards to energy transmission from the input load to the output port is analyzed. It is found that the optimized design is 74% efficient at transferring the energy from the harmonic load to the output port.

Although this is already quite good, higher efficiencies can be expected by choosing an energy-based objective or by enlarging the design domain and thus increasing the space for additional “mirrors”.

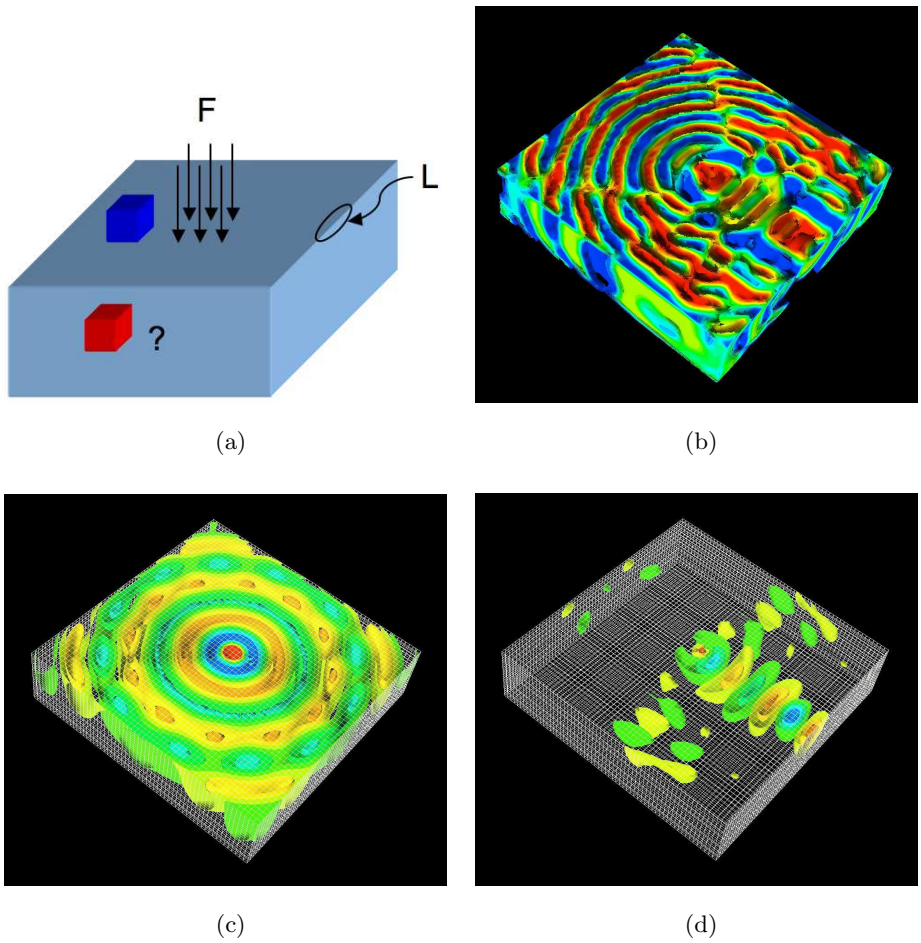

Figure 4.5: (a) Design setup for a surface wave device that focuses input energy from a normal surface load f into surface waves that exit the domain at location L. (b) Topology optimization results for the surface wave device problem. Material layout is presented in material isosurfaces that are generally located at material interfaces. (c) Surface waves seen as displacement isosurfaces propagate radially in a homogeneous material from the point of excitation as expected, but (d) are focused in one direction when they travel through the final design.

Manufacturable surface wave focuser

In a modification of the previous example, which in reality cannot be manufactured, this problem is set up to create a design that is manufacturable using lithography or thin film processes. The same problem as before is considered with the exception that the distribution of material (again silicon and aluminum) is confined to columns within a 1mm film on a substrate of silicon and the load is applied at 2.0 MHz. To confine the distribution, the material properties are "tied" vertically within the film layer to a single design variable. Again, the objective is to get as much surface wave energy as possible to exit the domain at a specific location.

The final optimized design layout as well as its wavefield and a homogeneous wavefield are shown in Figure 4.6. The layout of materials (Figure 4.6a) shows a non-intuitive design which effectively directs energy to the output port (Figure 4.6c) which would otherwise propagate radially (Figure 4.6b) from the input source. As was the case with the previous example, there are again the same recognizable features resembling the alternating series of curved mirrors that direct the energy in the proper direction. The difference here, however, is that in the previous problem the material distribution also created a bowl-like structure through the depth of the design. This bowl-like structure is able to also reflect bulk waves that are created by the harmonic load and propagate into the material, a capability not possible in the manufacturable design presented here.

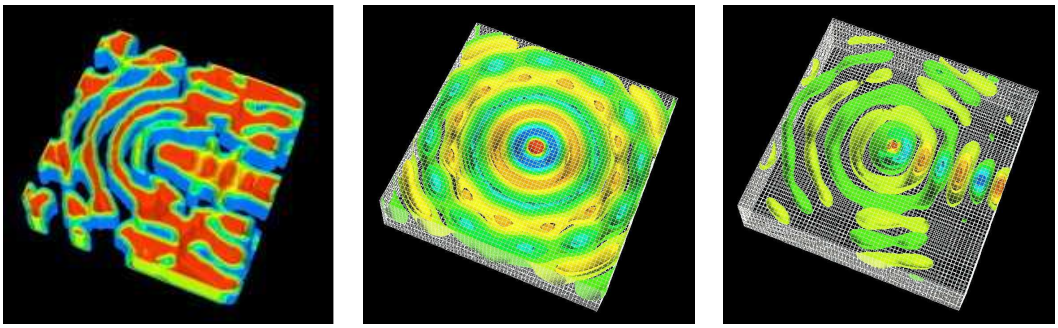

(a) (b) (c)

Figure 4.6: (a) Results of the surface waveguide problem reveal a non-intuitive distribution of silicon (blue) and aluminum (red). The wavefield, which (b) normally propagates radially from the source in a homogeneous material, is (c) guided to the output location in the final design.

Three dimensional surface wave bender

This example, analogous to the two-dimensional bending waveguide, is a surface wave bending waveguide situated on top of a three-dimensional halfspace. This example also demonstrates a FETI [49] large-scale topology optimization implementation for wave problems and is one of the largest problems ever demonstrated in the literature [47]. The problem is set up on a 10mm x 10mm x 4mm computational halfspace in which a 2mm to-be-determined layer of silicon and aluminum rests on a 2mm silicon substrate. A 2.0 MHz surface wave is excited at a 2mm port at the center of one of the edges and the objective is set to maximize the output at a 2mm port at the center of the edge perpendicular to the input edge. The domain is discretized into a 160x160x64 element mesh with a free top surface and non-reflecting boundary conditions on the other sides representing about 4.9 million complex, or 9.8 million real, degrees of freedom. To account for manufacturability, columns of elements within the film were tied to a single design variable resulting in a total of about 26,000 design variables. The solution of the wavefield is computed using the FETI solver and MMA is used for the optimization

problem.

The results are shown in Figure 4.7. The final material layout and wavefield are represented by isosurfaces. The wavefield shows that the surface wave bends and exits at a right angle to the input direction.

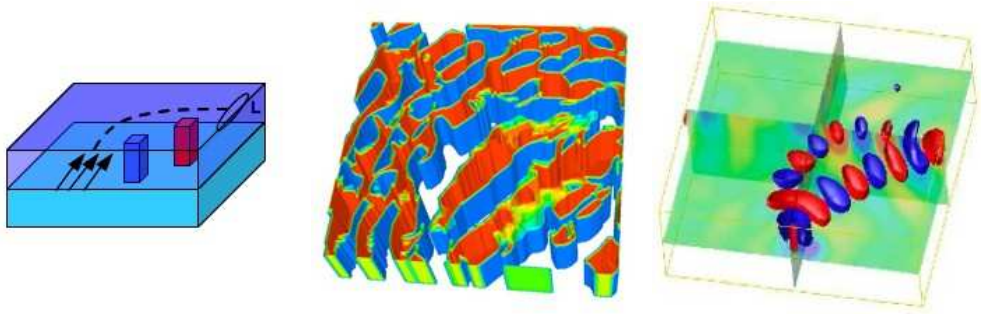

(a) (b) (c)

Figure 4.7: Results of a bending waveguide for surface waves showing the (a) design setup, (b) final material distribution of silicon (blue) and aluminum (red), and (c) the wavefield through the final design showing the surface wave bending to exit at the right.

4.5 Methodology Refinement Studies

The studies in this section focus on details of the methodology presented in this chapter and aim to expand it through increased understanding of the phenomena and requirements needed to solve these types of problems.

4.5.1 Optimization drivers and modeling needs

In general, topology optimization problems are driven to their optimal solution through the exploitation of a physical phenomenon. For example, many static structural optimization problems maximize the stiffness to mass ratio by creating a structure that is everywhere stressed at its maximum allowed stress value. For wave propagation problems Bellido and Donoso [8] have shown that "0-1" solutions are optimal in certain

cases of one-dimensional problems, but they do not investigate the physical phenomena behind the mathematics. Here, however, the physical phenomena drivers can be inferred through the example problems of this chapter. The first phenomena at work are wave reflection and transmission at a material interface, which are characterized by the impedance mismatch between two adjacent materials. The higher the impedance mismatch the higher the reflection coefficient (and lower the transmission coefficient) and thus the more wave energy that can be directed. A next phenomenon is the result of Bragg reflections. As stated earlier, this phenomenon exists when material interfaces are located at half-wavelength intervals of a traveling wave and collectively act as a mirror at certain frequencies. The effect is most prominently seen, but not necessarily expected, in the solutions to the bending waveguide problems which each look like an array of curved mirrors. The presence of these phenomena, both of which are influenced by material and geometric properties, are maximized when the material properties are as different as possible and together indirectly explain why "0-1" solutions in wave propagation optimization problems tend to be a natural occurrence. As such, these phenomena are the drivers for topology optimization problems involving wave propagation.

It may be noticed that some of the mesh sizes presented in the examples problems of this chapter are very large. The need for such a dense mesh is not immediately clear as many static structural optimization problems actually have difficulty with dense meshes (e.g. checkerboarding, small non-relevant features, etc.). The explanation also lies in the physics of the problem and can be explained through three factors. The first factor is caused by the Bragg condition. The effectiveness of this phenomenon is highly dependent on the precise placement material interfaces as evidenced by Figure 2.5 in section 2.2.1. As such, for static meshes, interface placement is directly dependent on the element size, thus dictates the need for a fine mesh. Poor placement, to a limited extent, only serves to reduce the effectiveness of the design rather than destroy it completely (i.e. the problem is not overly sensitive to changes). The second factor is the need to

resolve the wavefield. A very rough estimate for properly modeling a wavefield is to have ten elements per wavelength. In topology optimization problems, however, this is not enough as again the important factor is to define the location of material interfaces, the proper position of which is dependent on the wavelength. The third factor is the number of wavelengths one wants to fit into the domain, which depends on the problem of interest. Once all of these pieces are accounted for the problem quickly becomes very large as a necessity. As a rough minimal estimate, consider a three-dimensional surface wave problem with 20 elements per wavelength, 5 wavelengths in the domain, and a depth of 2 wavelengths. This results in a 100x100x40 mesh with approximately 1.25 million complex, or 2.5 million real, degrees of freedom. In general, this problem size is much larger than those performed with topology optimization for most other types of problems in the literature.

4.5.2 Mesh dependency study

A prominent issue in the design of structures using topology optimization is a phenomenon called "checkerboarding." It is characterized as an exploitation of the discretization of displacement-based finite elements in which adjacent elements within a mesh have an alternating pattern of "0" and "1" properties, which looks like a checkerboard for square meshes. The simplest explanation of their occurrence is that a "checkerboard" design has an artificially high stiffness due to the element formulation but still maintains a minimal mass to stiffness ratio, which is the usual form of the objective for these types of problems. Mesh refinement does not help the issue, as in most cases it just makes the checkerboarding finer. A number of methods exist for avoiding this problem such as various density filtering techniques or by using higher order displacement interpolation in the finite elements [11], but it has not yet been shown whether the same or similar problems occur in time harmonic wave propagation problems.

Based on physical principles, one can note the presence of a physical length scale

within wave propagation problems, namely the wavelength, that is noticeably absent in static structural problems. The presence of this inherent, mesh independent length scale has been noted before [146] and was used to explain the lack of mesh dependency for wave propagation problems. There have not been any studies in the literature, however, that have convincingly shown this argument to be true or false.

To study this question, the two-dimensional in-plane bending waveguide problem of section 4.4.2 was used to see what effect the degree of mesh refinement has on the solution to the optimization problem. The dimensions of the problem are kept constant with a loading force frequency of 2.8MHz while the size of the mesh is varied from a 50x50 to 400x400 element grid. No filtering or constraints are used on the problem, which would otherwise affect the presence of mesh-dependent effects. Figure 4.8 shows the elemental density distributions for the final design for this set of problems. As the figure shows, little change occurs in the predominant features of the structure with the exception of refinement in the details of the inclusions. This indicates that the design is generally converging as the mesh is refined, an observation in line with others [146]. Upon close inspection of the finest design, however, as shown in Figure 4.9, one can see that some features become much smaller than the smallest wavelength in the problem (the domain is about five wavelengths wide). These features are not, and cannot due to mesh size, be present in the coarser meshes, which indicates a mesh dependency.

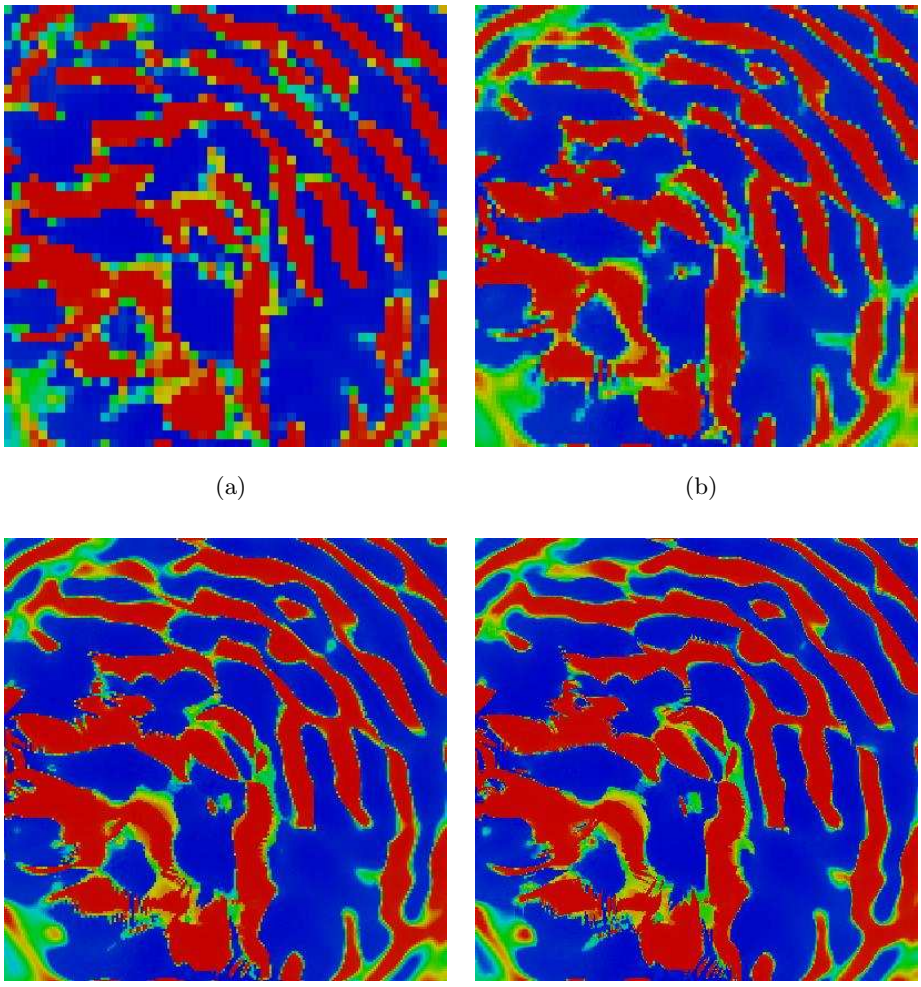

(a) (b)

(c) (d)

Figure 4.8: Bending waveguide optimization results for mesh sizes of (a) 50x50, (b) 100x100, (c) 200x200, and (d) 300x300. Little difference overall can be seen between the designs other than general refinement of the features.

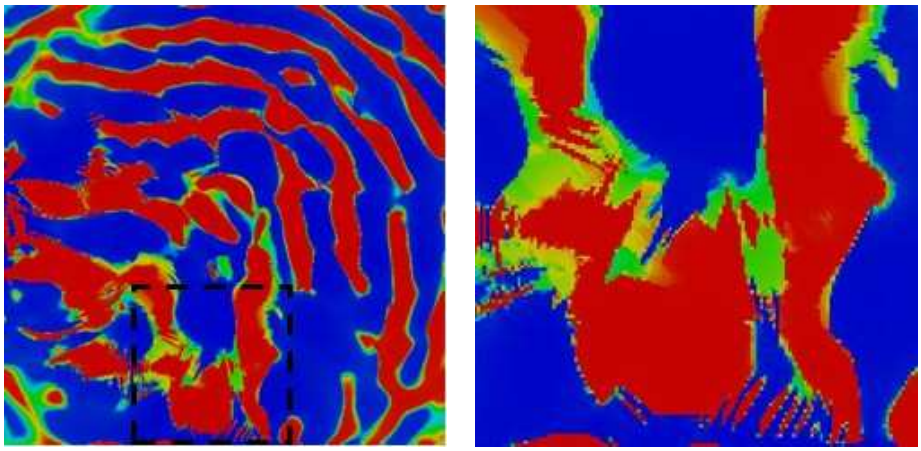

(a) (b)

Figure 4.9: Evidence of mesh-dependent effects in bending waveguide. (a) 400x400 mesh with (b) close-up view showing an area with effective material properties.

This study shows that there exists a mesh dependency for time harmonic wave propagation problems in topology optimization. As a mesh gets finer, there is a general convergence to a specific design due to the inherent length scale presented by the wavelength. Further mesh refinement, however, introduces regions where very small features appear. One can reasonably speculate that in these regions the optimization algorithm is trying to make a section of the design with effective material properties rather than use reflection and transmission as the driving factors for design. As a result of these two competing factors there likely exists for all harmonic wave propagation topology optimization problems a mesh density or range of mesh densities where major features with sizes on the order of the wavelength are sufficiently converged, but minor features with sizes much smaller than the wavelength have not yet appeared. Based on this study, a general guideline for preventing minor features is to use a mesh density that has between 15 and 40 elements per wavelength. This observation encompasses the high-end guideline for general wave propagation analysis (about 10 to 20 elements per wavelength) but also includes even finer discretizations necessary for accurate placement

of interfaces (as discussed in section 4.5.1).

4.5.3 Impact of small-sized features

As shown in the examples of this chapter, topology optimization can create elastic waveguides with very complex and intricate material layouts. While it is possible, depending on the length scale, to manufacture these designs using a variety of processing techniques including thin film deposition, questions arise as to whether such detailed features are really necessary for the waveguide to function. In particular, how much do small features contribute to the waveguiding ability and performance? If small features have a negligible impact then they can be removed from the design, thereby potentially simplifying and reducing manufacturing costs.

To study this question, the 200x200 element bending waveguide problem from section 4.5.2 is considered. A penalization of the non-converged design variables and then a thresholding is applied to this design to create a purely "0-1" solution. This process changed the efficiency of the waveguide from 94.4% to 94.0%, based on integrating the Poynting vector at the input and output ports. Starting with the thresholded design, image processing techniques are used to remove small features such as small inclusions or ragged edges in the design. Two image morphology functions are used on a binary image of the design where each pixel represents an individual element. The first is morphological closing where a disk of a given pixel radius is used to dilate and erode pixel boundaries, which essentially smooths the boundaries. The second function removes groups of pixels whose collective population is smaller than some threshold, which acts to remove small features from the design. The final image is then translated back into a finite element model that is then solved. Two levels of processing are considered here. This first is a medium level in which the morphological closing pixel radius is 1 and the pixel group threshold is 20 pixels. The second, high level of processing is more aggressive where the pixel radius is 2 and the group threshold is 30 pixels.

Figure 4.10 shows the designs and results of this study. The original design, the thresholded design, and the two processed designs are shown along with figures showing the differences between the processed and thresholded design. In the processed designs, the medium level produces changes where 0.94% of the total area of the design is altered whereas the high level changes the design by 2.32%. The efficiencies of the designs are 90.5% for medium processing and 80.2% for high processing. These results indicate that a moderate level of smoothing and small feature removal has little effect on the performance of the waveguide. Making too many adjustments to the design, however, can noticeably impair the device, although the vast majority of energy is still guided properly to the exit as shown in the magnitude of the Poynting vector magnitudes in Figure 4.10.

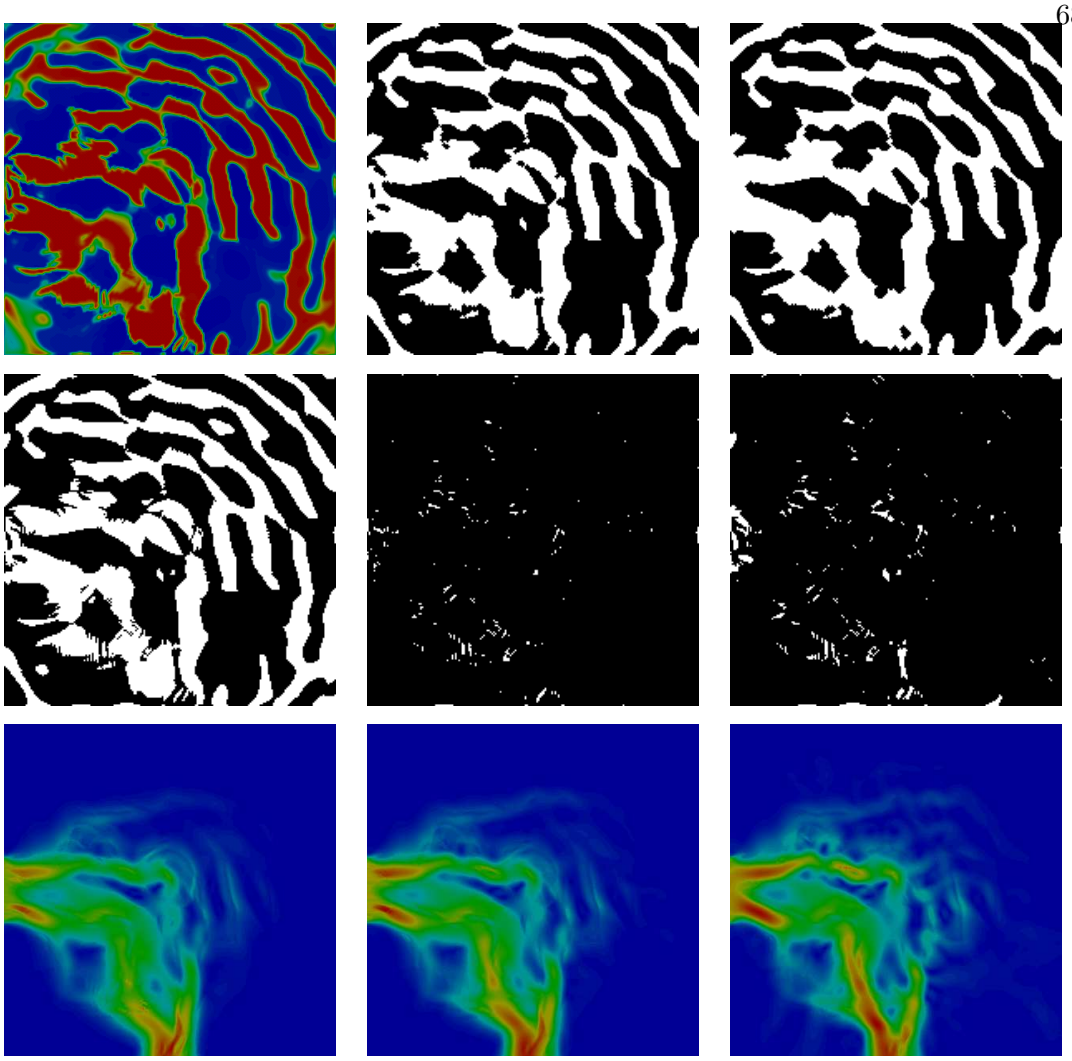

Figure 4.10: Bending waveguide design subject to post processing to remove small features. (a) (top) Original and (middle) thresholded material layouts of silicon (blue/black) and aluminum (red/white) for the bending waveguide. (b) Medium and (c) high levels of (top) post processed designs result in (middle) different degrees of design change from the thresholded design. (bottom) The Poynting vector magnitude of the wave field for each of these material layouts.

4.5.4 Symmetric optimization landscapes and non-optimal KKT points

It is well known that topology optimization problems may have multiple, even numerous, local optima. Most optimization algorithms find these optima by looking

for design points that satisfy the Karush-Kuhn-Tucker (KKT) optimality conditions. In this section, an example is given that exhibits behavior suggesting that the optimization landscape is symmetric; a fact that indicates the KKT point may be located at a saddle point rather than a convex local optimum.

The existence of a symmetric optimization landscape was first noticed when solving the P-wave to S-wave converter problem of section 4.4.2. In exploring this problem further, a mesh of 120 elements per side was used. In an unrelated mesh dependency study, three different final designs were found within the set of mesh size cases. Two designs were unsymmetric, but perfect mirror images of each other, while the third design was symmetric about a horizontal line through the center of the design domain (see Figure 4.11a-c). The two mirror image designs also had nearly equal objective values, which were significantly better than the symmetric design. The final scaled objectives for the non-symmetric designs were about $z \approx 51$ while for the symmetric design $z \approx 11$ (larger is better). Upon further inspection here, it was found that small perturbations (1% in a single design variable) in the initial design would cause the algorithm to end up at one of the unsymmetric designs. The perturbation direction also mattered, a positive perturbation would end up at one unsymmetric design while a negative perturbation would end up at the other mirrored image. It is important to note that the choice of perturbed design variable matters significantly since the gradient of the objective is different for each design variable, although it this generally only influenced the number of iterations it takes to move the design toward one of the unsymmetric design. These results indicate that the optimization landscape is symmetric, at least near the initial design at the center of the design space, and that the center is located on this symmetry. The fact that better local optima exist on either side of the symmetry also indicates the possibility that the final symmetric design lays at a KKT point that is a saddle within the optimization landscape rather than an optimum. To test this, the final symmetric design was restarted with a small perturbation in one of the design variables. The

result of this perturbation can be seen in Figure 4.11d where an unsymmetric design was reached. This new design is similar to the other unsymmetric designs, yet still with significant differences, and had a similar final objective value. These results indicate that the symmetric design is indeed at a non-optimal KKT point located at a saddle point.

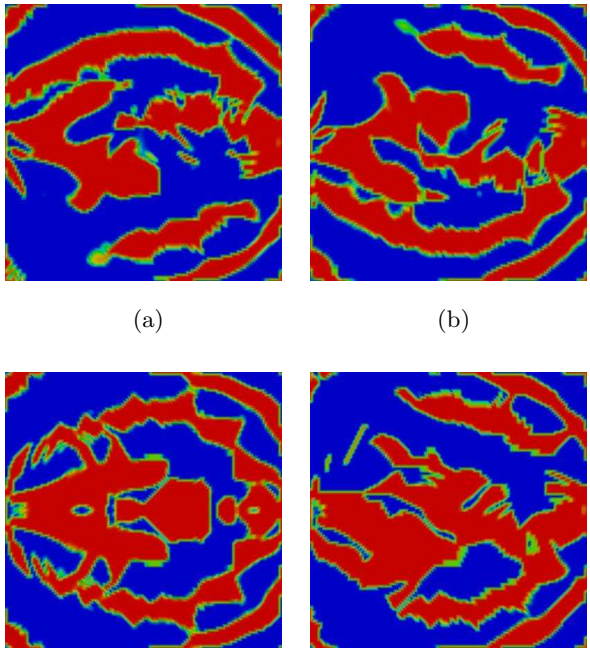

(a) (b)

(c) (d)

Figure 4.11: The three solutions to the P-wave to S-wave converter problem with a P-wave entering a port on the left and an S-wave exiting a port on the right. A small perturbation in the initial design space in the (a) positive and (b) negative directions will push the set of design variables off the symmetry and into one of the mirror image local optima which have equal and better objective values ($z \approx 51$) than a final design (c) that is symmetric ($z \approx 11$). This indicates that the problem has a symmetric optimization landscape. (d) A small perturbation in the final symmetric design pushes the problem to an improved objective with a different unsymmetric design, indicating that the symmetric design is located at a saddle point in the optimization landscape.

It turns out, as is evidenced by creating small perturbations in the initial wave converter design, that a design must be on a line of symmetry (or somehow land on one) within the optimization landscape in order for it to find a KKT point that is a saddle. If some set of design variables is on a symmetry in the optimization landscape then the gradient will always point in a direction that will also be on a symmetry. Therefore, ignoring information from the Hessian, the optimum will also be found on a symmetry. If the Hessian is positive definite at the KKT point then this is not a problem because the problem is locally convex, but if the Hessian is non-positive definite then a saddle point has been reached; unknowingly so if no Hessian information is computed. The Hessian, however, is expensive to compute, so it is usually avoided. Therefore the best way to get away from the symmetry saddle point problem is to avoid it altogether. Hence, this study shows that without a method to detect the presence of a symmetry, starting from a random set of design variables can be desirable, although this is not common practice in the field. It should be noted that this phenomenon is not unique to wave propagation optimization problems, but an issue in optimization problems in general.

4.5.5 Poynting vector objective function

In isotropic, homogeneous materials the direction of the Poynting vector coincides with a wave's direction of propagation. In heterogeneous materials, however, this may not be the case, as multiple reflections will create many waves traveling in different directions that may occupy the same space. As such, the complex norm of the displacements at a location is not necessarily a good indicator of energy propagation in elastic waves because of its lack of directionality and inability to differentiate between traveling and standing waves. A more appropriate measure is the Poynting vector, a measure of energy flux and direction at any location. While the physical advantages of the Poynting vector are obvious, it has yet to be shown that it is an improvement over

the complex norm objective function for elastic waveguide problems.

To study this issue, the bending waveguide problem with a 200x200 element mesh surrounded by viscous damping boundary conditions is considered. The problem is solved twice, once using the complex norm objective function and again using the Poynting vector objective function. The complex norm objective function maximizes the displacement norms normal to the exit port and minimizes those parallel to it. The Poynting vector objective function maximizes the Poynting vector in the direction leaving the exit port and minimizes its square in the direction parallel to the port. After 200 iterations the design variables are penalized so that a "0-1" solution results. The final material layouts, including the complex norm of the displacements and the norm Poynting vector, are shown in Figure 4.12. While the final designs are somewhat different, the effectiveness of the two objective functions is about equal as evidenced by 94.6% and 93.2% efficiencies for the complex norm and Poynting vector objective functions, respectively. This is also supported by Figure 4.13, which shows cross-section plots of the Poynting vector at the input and output ports for both objectives functions.

The significant finding of this study is that both objective functions perform well for solving elastic waveguide problems, regardless of the disadvantages of the complex norm objective function. The primary reason for this is likely the location of these functions at the boundary of the computational domain where viscous damping boundary conditions remove the wave energy. Because of this the wave energy can only have one direction (out of the domain) and so the complex norm objective cannot suffer from the formation of standing waves. Objective locations on the interior of the domain would likely produce a different result. In the waveguide examples, however, the goal is to have the energy exit the domain at a certain location, so this is not a problem. Another issue at hand is the computational expense of the Poynting vector objective function. Not only must the Poynting vector be computed each iteration, but its gradients must also be computed, both of which are computationally expensive tasks relative to the complex

norm objective function. These findings are the primary reason why the examples in this chapter use the complex norm objective function rather than the more physically relevant Poynting vector objective function.

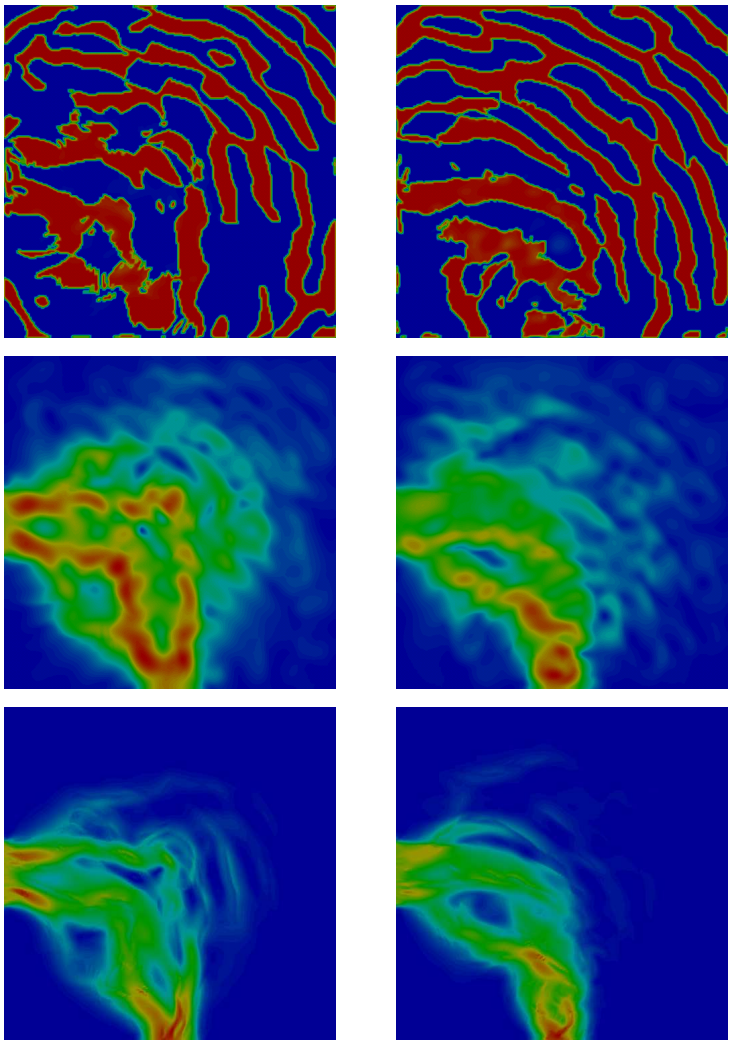

(a) (b)

Figure 4.12: Material layouts (top), complex norm displacement field (middle), and Poynting vector field (bottom) for topology optimization problems using (a) complex norm and (b) Poynting vector objective functions.

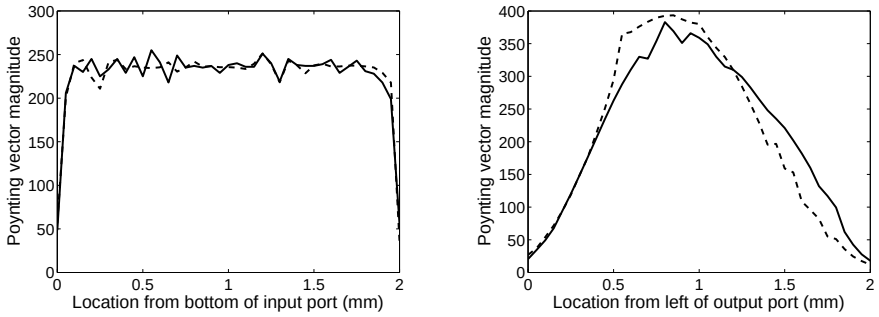

(a) (b)

Figure 4.13: Poynting vector profile at the (a) input and (b) output ports for the complex norm (solid) and Poynting vector (dashed) objective functions.

4.6 Summary

The work in this chapter investigates a number of aspects of topology optimization problems for wave propagation. In the examples, the most prominent and recurring feature was the presence of periodic material interfaces forming Bragg grating structures. This illustrates the importance of Bragg reflections as a design driver for waveguide problems. The influence of a free surface was also illustrated and showed how surface waves and their interaction with bulk waves had a significant impact on the final design. This is particularly evident in the differences between the normal and manufacturable surface wave focusing problems. For in-plane problems the interaction between different bulk modes was demonstrated and revealed that multiple mode conversions can also play an important role in the optimal design. When this problem was further investigated later in the chapter, it revealed that in some optimization problems a symmetric optimization landscape can result, an interesting and important finding for the existence of local optima in waveguide problems. Also discussed in this chapter are the limitations of waveguide designs posed by computational constraints from the extensive models needed to resolve wavefields. These limitations create constraints on the types

of waveguide problems that can be solved. Finally, it was shown that in the bending waveguide problem, and likely all waveguide problems, that while the Bragg condition is the primary design driver for the problem, in high-density meshes small features appear that cannot be explained by the Bragg condition. These features, which are a fraction of a wavelength is size, are suggested to cause local anisotropies in the design where a passing wave sees the effective properties that the features create rather than the features themselves. Creating these anisotropies could be beneficial for the objective, making the creation of such features another design driver. Fortunately, however, the impact of these small features on the efficiency of the design was shown to be very small and such issues can be largely ignored for end result purposes. Nevertheless, it raises an interesting and potentially useful aspect of wave propagation problems.

Chapter 5

Topology Optimization of Band-gap Materials

5.1 Introduction

The content of this chapter investigates the use of two techniques for the design of band-gap materials with topology optimization. To discern between these two design techniques a distinction is made between band-gap structures and band-gap materials, even though both can be considered band-gap materials in some sense. Band-gap structures correspond to topology optimization problems that are solved using time-harmonic analysis where the objective is to minimize the transmission of waves through the band-gap material design space, which may consist of a finite number of unit cells of the material embedded in a host structure. Because this configuration models only a finite number of unit cells, it is considered a band-gap structure. In a band-gap material, on the other hand, the band-gap material unit cell is modeled with indefinite repetition. This requires a different type of analysis and an objective function that operates directly on the dispersion relation of the material. The goal of this chapter is to investigate the connections between the design of band-gap structures and band-gap materials, the advantages and disadvantages of each, and to further develop the design methodology for band-gap materials by investigating some of its properties including the physical drivers of the problems.

This chapter is organized as follows: the analysis technique for band-gap material problems based on Bloch-Floquet theory is presented along with the development of spe-

cialized finite elements and sensitivity analysis to solve these problems. The modeling approaches for band-gap structure and band-gap material problems are then verified and followed with numerous examples of each technique used in design with topology optimization. Next, variations on the form of the objective function for band-gap materials is discussed and experiences with initial designs and solution techniques for band-gap material problems are shared. The chapter is ended with a summary.

5.2 Analysis

The following subsection outlines the analysis methodology for band-gap material problems based on Bloch-Floquet theory. This theory allows for the analysis of an infinitely periodic unit cell, the core component of a band-gap material. This subsection is followed by the sensitivity analysis procedure for this type of problem.

5.2.1 Band-gap material problems

Bloch-Floquet theory

The goal in the analysis of band-gap materials is to reproduce the dispersion relation for a structured periodic material. Mathematical analysis these types of phenomena first started when wave propagation with periodicity in time was studied by Floquet [52] in 1883, but it was Bloch [13] in 1928 who eventually generalized the findings to spatial periodicity, hence Bloch-Floquet theory. The analysis of periodic materials was further enhanced by the work done in solid state physics by Brillouin [17] in which he developed the concept of Brillouin zones specifically for analysis of electron mobility in atomic lattice structures. A number of methods exist for analyzing the band structure of a material including multiple scattering theory [106], the finite difference time domain (FDTD) method [75], and the transfer matrix method [16]. Here, it carried out using finite elements and Bloch-Floquet theory [72, 98]. The analysis starts by assuming that the structured material can be described by a single unit cell repeated indefinitely in at

least one direction. Infinite periodicity in one direction constitutes a one-dimensional band-gap material, whereas two independent directions a two-dimensional and three independent directions a three-dimensional band-gap material. This periodicity, called translational symmetry, is the primary underlying assumption when using Bloch-Floquet theory. Given a unit cell with domain $\Omega = \left[-\frac{a_i}{2}, \frac{a_i}{2}\right]^n \in \Re^n$ and material properties $\lambda = \lambda(\mathbf{x})$, $\mu = \mu(\mathbf{x})$, and $\rho = \rho(\mathbf{x})$ as functions of location within the unit cell and a lattice vector $\mathbf{R} = n_1 a_1 \hat{\mathbf{x}}_1 + n_2 a_2 \hat{\mathbf{x}}_2 + n_3 a_3 \hat{\mathbf{x}}_3$, where a_i are dimensions of the unit cell in the $\hat{\mathbf{x}}_i$ directions and n_i are independent integers, then it is true that $\lambda(\mathbf{x}+\mathbf{R}) = \lambda(\mathbf{x})$, $\mu(\mathbf{x}+\mathbf{R}) = \mu(\mathbf{x})$, and $\rho(\mathbf{x}+\mathbf{R}) = \rho(\mathbf{x})$. Defining a translation operator $T_{\mathbf{R}}$ such that $T_{\mathbf{R}} f(\mathbf{x}) = f(\mathbf{x}+\mathbf{R})$, one can show that its eigenfunctions are of the form $e^{i\mathbf{k}\cdot\mathbf{x}}$:

$$T_{\mathbf{R}} e^{i\mathbf{k}\cdot\mathbf{x}} = e^{i\mathbf{k}(\mathbf{x}+\mathbf{R})} = \left(e^{i\mathbf{k}\cdot\mathbf{R}}\right) e^{i\mathbf{k}\cdot\mathbf{x}}. \tag{5.1}$$

Under this periodicity, however, $\mathbf{k}$ forms a degenerate set. Given $\mathbf{k}^{new} = \mathbf{k} + \mathbf{G}$, where $\mathbf{G}$ is the reciprocal lattice vector $\mathbf{G} = \left(k_1 + m_1\frac{2\pi}{a_1}\right)\mathbf{x}_1 + \left(k_2 + m_2\frac{2\pi}{a_2}\right)\mathbf{x}_2 + \left(k_3 + m_3\frac{2\pi}{a_3}\right)\mathbf{x}_3$ with integers m_i, it can be shown that $\mathbf{k}$ and $\mathbf{k}^{new}$ yield the same eigenvalues. Thus it is only necessary to examine $\mathbf{k}$ within Ω, which is called the Brillouin zone. If one assumes a form for the wave displacements:

$$\mathbf{u}(\mathbf{x}, \mathbf{k}) = \mathbf{u}^{\mathbf{k}}(\mathbf{x}) e^{i\mathbf{k}\cdot\mathbf{x}} \tag{5.2}$$

then $\mathbf{k}$ becomes the wavevector and the displacements form harmonic plane waves traveling in the direction of the wavevector. The displacements $\mathbf{u}^{\mathbf{k}}$ are periodic such that $\mathbf{u}^{\mathbf{k}}(\mathbf{x}+\mathbf{R}) = \mathbf{u}^{\mathbf{k}}(\mathbf{x})$ (from (5.1)) and are called Bloch modes (or Bloch waves or Floquet modes/waves).

Brillouin finite elements

Specialized finite elements are needed to solve band-gap material problems because of the dependence of the stiffness matrix on the wavevector. Inserting (5.2) into the equations of motion (4.9) with null forcing function is equivalent to (after dropping

$e^{i\omega t}$ and $e^{i\mathbf{k}\cdot\mathbf{x}}$ terms) changing operators $\nabla \rightarrow \nabla + i\mathbf{k}$ resulting in a new form for the equations of motion:

$$(\nabla + i\mathbf{k})(\lambda + \mu)(\nabla + i\mathbf{k}) \cdot \mathbf{u}^{\mathbf{k}} + \mu(\nabla + i\mathbf{k})^2 \mathbf{u}^{\mathbf{k}} - \omega^2 \rho \mathbf{u}^{\mathbf{k}} = \mathbf{0}. \tag{5.3}$$

In weak form this is written as:

$$\int_{\Omega} \mathbf{v} \cdot (\nabla + i\mathbf{k})(\lambda + \mu)(\nabla + i\mathbf{k}) \cdot \mathbf{u}^{\mathbf{k}} + \mu \mathbf{v} \cdot (\nabla + i\mathbf{k})^2 \mathbf{u}^{\mathbf{k}} - \omega^2 \rho \mathbf{v} \cdot \mathbf{u}^{\mathbf{k}} d\Omega = \mathbf{0} \tag{5.4}$$

with test function $\mathbf{v}$ and integrated over the volume of the unit cell Ω. Using the Galerkin method, the resulting finite element equations yields the generalized eigenvalue problem:

$$\mathbf{K}(\mathbf{k})\mathbf{u}_j^{\mathbf{k}} = \omega_j^2 \mathbf{M}\mathbf{u}_j^{\mathbf{k}} \tag{5.5}$$

where the unit cell domain Ω is periodic with appropriate periodic boundary conditions applied to satisfy (5.1), which is now a function of the wave vector. The application of periodic boundary conditions can be performed in a number of ways. For example, Hofer et al. [74] describe two procedures for implementing periodic boundary conditions by using a Schur-complement method and a method that condenses boundary nodes. In this dissertation, linear multi-point constraint equations are used to tie boundary nodes. The stiffness matrix for isotropic materials can then be written with the material properties separated from the wavevector as $\mathbf{K}(\mathbf{k}) = \lambda \mathbf{K}_\lambda(\mathbf{k}) + \mu \mathbf{K}_\mu(\mathbf{k})$ while the mass matrix is formulated as usual. The resulting stiffness matrix $\mathbf{K}(\mathbf{k})$ is complex Hermitian for a non-zero wavevector (real symmetric otherwise) and the separation of the material properties from the wavevector makes calculation of the gradients simple, i.e. $\frac{\partial \mathbf{K}(\mathbf{k})}{\partial s_i} = \frac{\partial \lambda}{\partial s_i}\mathbf{K}_\lambda(\mathbf{k}) + \frac{\partial \mu}{\partial s_i}\mathbf{K}_\mu(\mathbf{k})$. This formulation has been used in numerous studies including for the formulation of photonic finite elements [4, 29] and was used by Halkjær et al. [68], Hussein et al. [80, 82], and Sigmund and Jensen [146] for band-gap material analysis and design.

Dispersion relation

It is now possible to find the dispersion relation between the wavevector $\mathbf{k}$ and the set of eigenvalues ω_j^2 that forms the dispersion relation for the band-gap material. To fully describe the dispersion relation, equation (5.5) must be solved for multiple values of $\mathbf{k} \in [-\pi/a_i, \pi/a_i]^n$ in the Brillouin zone. At this point it is possible to utilize symmetries in the material design to reduce the region in which $\mathbf{k}$ must be evaluated. As was the case with the translation operator, rotational and mirror symmetries in the design also cause symmetries in the eigenvalue problem in which redundant eigenvalues appear for a given wavevector. Thus the Brillouin zone can be reduced to a region in which $\mathbf{k}$ can be evaluated without redundancy called the irreducible Brillouin zone [87]. As an example, take a two-dimensional square unit cell in the x-y plane of size $2a$ with symmetries along the $(1,0)$, $(0,1)$, $(1,1)$, and $(1,-1)$ directions. The Brillouin zone is the whole square while the irreducible Brillouin zone is a triangular region one-eighth the size as seen in Figure 5.1(a). Scanning the whole space of the irreducible Brillouin zone is still costly, so it is customary to scan only its boundary, usually scanning from Γ to X to M and back to Γ, to produce the dispersion relation 5.1(b). Other combinations of symmetries may be used, including a one-dimensional symmetry for layered structures or when only concerned with one direction of propagation (e.g. bars or beams). Hexagonal arrays with triangular symmetries are also often used in these problems, but not in this dissertation.

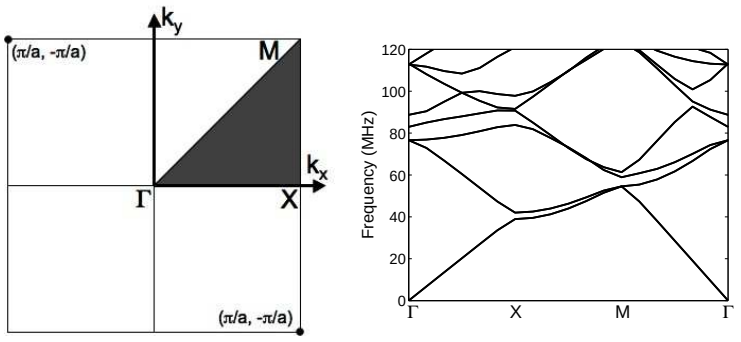

(a) (b)

Figure 5.1: (a) Brillouin zone and irreducible Brillouin zone (shaded region) for a material with unit cell size $2a$ and symmetries along the $(1,0)$, $(0,1)$, $(1,1)$, and $(1,-1)$ directions. (b) An example dispersion diagram showing the dependence of eigenvalues on the wavevector varying from Γ to $\mathbf{X}$ to $\mathbf{M}$ and back to Γ.

5.2.2 Sensitivity analysis for eigenvalue problems

The sensitivity analysis for eigenvalue problems is different that that for time-harmonic problems. Here the sensitivities of the eigenvalues w.r.t. the design variables are derived. Rearranging and reducing (5.5) for a single wavevector, the band-gap material eigenvalue problem can be written as:

$$(\mathbf{K} - \Lambda_j \mathbf{M})\, \mathbf{\Phi}_j = \mathbf{0} \tag{5.6}$$

where Λ_j are the eigenvalues and $\mathbf{\Phi}_j$ are the corresponding eigenvectors. Differentiating this with respect to the design variables s_i results in:

$$(\mathbf{K} - \Lambda_j \mathbf{M})\, \frac{\partial \mathbf{\Phi}_j}{\partial s_i} + \left(\frac{\partial \mathbf{K}}{\partial s_i} - \frac{\partial \Lambda_j}{\partial s_i} \mathbf{M} - \Lambda_j \frac{\partial \mathbf{M}}{\partial s_i} \right) \mathbf{\Phi}_j = \mathbf{0} \tag{5.7}$$

which can be pre-multiplied by the left eigenvector $\mathbf{\Phi}^L$ and rearranged to get the following equation.

$$\frac{\partial \Lambda_j}{\partial s_i} \mathbf{\Phi}_j^L \mathbf{M} \mathbf{\Phi}_j = \mathbf{\Phi}_j^L \left(\mathbf{K} - \Lambda_j \mathbf{M}\right) \frac{\partial \mathbf{\Phi}_j}{\partial s_i} + \mathbf{\Phi}_j^L \left(\frac{\partial \mathbf{K}}{\partial s_i} - \Lambda_j \frac{\partial \mathbf{M}}{\partial s_i} \right) \mathbf{\Phi}_j \tag{5.8}$$

The term $\mathbf{\Phi}_j^L\left(\mathbf{K}-\Lambda_j\mathbf{M}\right)$ satisfies the original eigenvalue equation and thus is a zero vector reducing (5.8) to:

$$\frac{\partial\Lambda_j}{\partial s_i}=\frac{\mathbf{\Phi}_j^L\left(\frac{\partial\mathbf{K}}{\partial s_i}-\Lambda_j\frac{\partial\mathbf{M}}{\partial s_i}\right)\mathbf{\Phi}_j}{\mathbf{\Phi}_j^L\mathbf{M}\mathbf{\Phi}_j} \tag{5.9}$$

for which if the mass and stiffness matrix are both self-adjoint (Hermitian) then the right and left eigenvectors are also adjoint (i.e. conjugate transposes of each other, $\Phi_j^L=\Phi_j^*$, where $(\cdot)^*$ denotes the conjugate transpose) and thus easily found as long as the eigenvalues are simple, otherwise the derivative does not exist. If the eigenvectors have been normalized to the mass matrix then $\mathbf{\Phi}_j^*\mathbf{M}\mathbf{\Phi}_j=1$ and (5.9) can be rewritten as:

$$\frac{\partial\Lambda_j}{\partial s_i}=\mathbf{\Phi}_j^*\left(\frac{\partial\mathbf{K}}{\partial s_i}-\Lambda_j\frac{\partial\mathbf{M}}{\partial s_i}\right)\mathbf{\Phi}_j \tag{5.10}$$

where the partial derivatives of the stiffness and mass matrices can be evaluated either analytically or numerically at an elemental level as described in the previous section. With this expression, it is easy to use the eigenvalues and eigenvectors obtained from (5.6) and on an elemental level obtain the eigenvalue sensitivities. In the case of degenerate eigenvalues, their gradients do not exist because the eigenvectors are not unique. This can be fixed by using a method for computing directional derivatives for non-simple eigenvalues [137]. In this document eigenvalue multiplicity is not treated differently as eigenvalues in most cases become unique after a couple iterations of the optimization algorithm or with the use of a random initial topology.

5.3 Verification

5.3.1 Material properties

The properties of materials used in this chapter are given in Table 5.1.

Table 5.1: Material Properties

Material	E-Elastic Modulus (GPa)	ν-Poisson's ratio	ρ-Density (kg/m^3)
Silicon	162.9	0.2226	2331
Aluminum	70.38	0.3454	2697
Tungsten	409.83	0.2799	19260
Silica	73.0	0.17	2200
Material 1	4e9	0.34	1000
Material 2	20e9	0.34	2000

5.3.2 Verification with the classical Bragg grating

While the analysis of time-harmonic wave propagation was verified in the previous chapter, the classical Bragg grating band-gap structure provides the perfect example to verify the topology optimization procedure. This problem is solved on a 5cm long x 1cm wide domain with periodic boundary conditions on the top and bottom and viscous damping non-reflecting boundary conditions on the left and right boundaries. The design domain is discretized with 9768 finite elements with each element assigned to its own design variable. A 400 kHz harmonic load is applied at the left boundary, which introduces a pressure wave into the domain. The objective function consists of minimizing the sum of the squares of the displacement norms (4.27) along the right boundary (see Figure 5.2a) by finding the optimal pattern of aluminum and silicon. The solution yields a repeated pattern of silicon and aluminum layers (Figure 5.2b). These layers are the same dimension as would be provided by using the Bragg condition 2.7 for these materials and at this frequency (i.e. the unit cell spans one-half wavelength). A frequency spectrum analysis (Figure 5.2e) reveals that the transmission of elastic waves through the optimized design exhibits the expected band-gap around the applied frequency within which the wave gets reflected but outside of which other frequencies

pass through the structure with little to no loss.

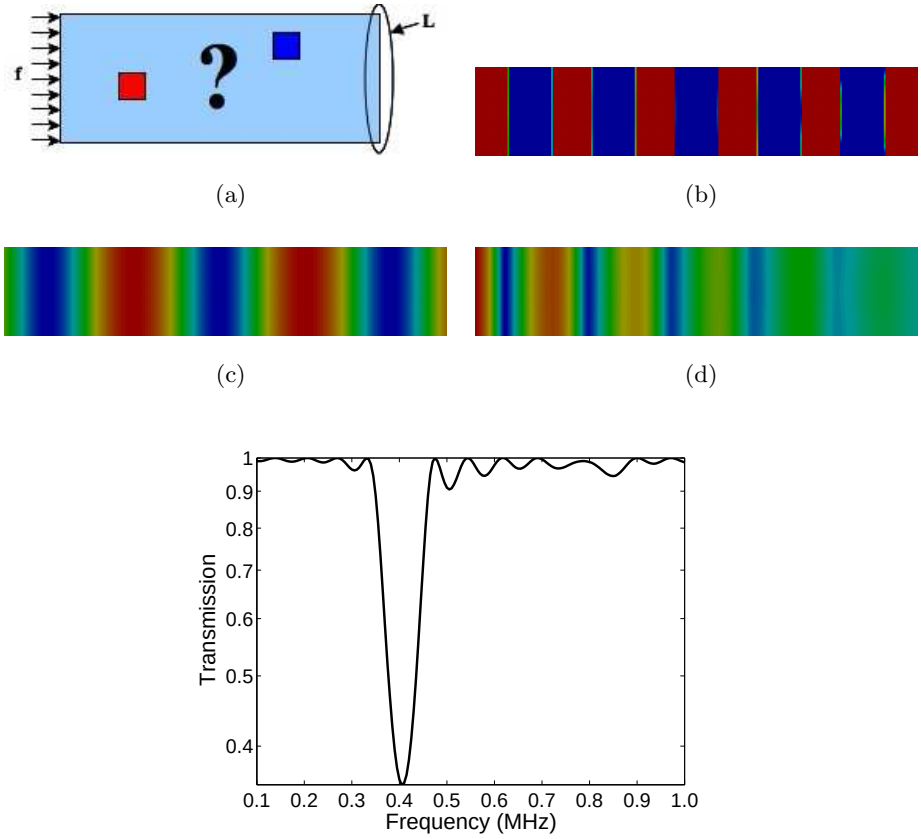

Figure 5.2: (a) Problem setup for the validation of the classic Bragg grating with elastic waves. (b) The final design shows alternating layers of silicon (red) and aluminum (blue). (c) Wavefield in a homogeneous structure shows the energy passing through, while in the final structure the waves are attenuated as shown in the (d) complex norm of the wavefield. This is also shown by a (e) frequency sweep of the wave transmission through the structure.

5.3.3 Comparison with published experimental results

To verify the eigenvalue analysis methodology for band-gap material problems the technique is compared to the published results of an experimental study of a bulk wave

band-gap material made of silica with tungsten scatterers [121]. The unit cell for this design consists of a square with $45\mu m$ lattice constant and circular scatterers of radius $14.4\mu m$ concentric around a manufacturing release hole of $5\mu m$ as shown in Figure 5.3a. The band-gap material is suspended above the substrate to prevent the creation of surface waves and bulk waves were excited and received by piezoelectric couplers. Using the Bloch-Floquet analysis technique for in-plane modes of propagation, the dispersion diagram in Figure 5.3b is found, revealing a large band-gap from 57-75 MHz between modes five and six. A smaller band-gap between modes three and four is also seen. Overlaying this with the transmission measurements of the experiment (Figure 5.3c, reproduced from [121]) shows very good agreement between the two.

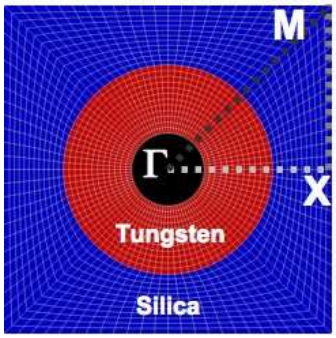

(a)

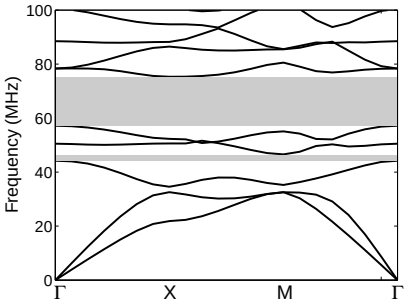

(b)

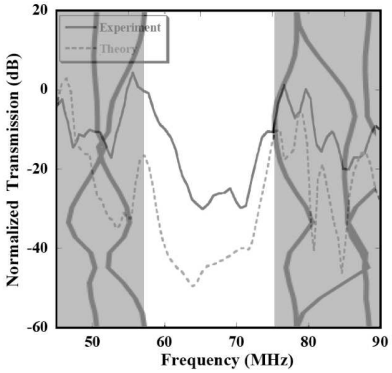

(c)

Figure 5.3: (a) This unit cell design results in (b) a dispersion diagram with three distinct band-gaps (gray regions). (c) A comparison with the experimental results of Olsson et al. shows good agreement where gray areas are bands of existing modes which lie on either side of the band-gap.

5.4 Applications

5.4.1 Objective functions

Band-gap structures

Band-gap structure topology optimization problems are treated in the same way as for the waveguide problems in the previous chapter in that the complex norm objective function 4.27 is used. Here, however, the objective is minimized at a location opposite to the incoming wave with the idea that the absence of the wave indicates that it was

reflected and that the intervening material/structure acts as a band-gap material for the frequency of interest. The globally convergent method of moving asymptotes [151] is used as the optimization algorithm.

Band-gap materials

The objective function used in the band-gap material examples to maximize band-gaps is a modification of that used by Bendsøe and Sigmund [11] and Sigmund and Jensen [146]. The formulation is:

$$\begin{aligned} &\max_{s_i} \beta_2 - \beta_1 \\ &s.t. \ \left(\mathbf{K}\left(\mathbf{k}\right) - \omega^2 \mathbf{M}\right)\mathbf{u} = \mathbf{0} \quad \mathbf{k} \in [\Gamma - X - M - \Gamma] \\ &\left[\omega_{j+1}^2\left(\mathbf{k}\right)\right]_m \geq \beta_2 \qquad\qquad m = 1 \ldots n_m \\ &\left[\omega_{j}^2\left(\mathbf{k}\right)\right]_m \leq \beta_1 \qquad\qquad m = 1 \ldots n_m \end{aligned} \tag{5.11}$$

where ω_j is the j^{th} eigenfrequency in order of increasing frequency, m corresponds to the m^{th} wavevector in the n_m-times discretized wavevector space, and β_1 and β_2 are independent scalars that act individually on the lower and upper constraint bounds, which locate the edges of the band-gap. The sensitivities of this objective and set of constraints are found from (5.10). The value of the objective can be negative, indicating that a band-gap does not exist for the current design. The constraints, however, change with the design and their formulation does not require a pre-existing band-gap, unlike other objective formulations [29, 30]. The optimization problems using this objective are solved with either a sequential quadratic programming algorithm [60, 135] or the globally convergent method of moving asymptotes [151].

5.4.2 Band-gap structure examples

The following examples illustrate the design of band-gap structures that are created with the same objective function that was formulated for waveguides. In essence, these structures are also waveguides (as opposed to band-gap materials), albeit with

frequency dependent characteristics. The goal of these problems is to alter the frequency response of the structure in a desired fashion by using (4.27) to minimize the complex displacement norms after the energy has passed through the region of interest. In some cases a multi-objective problem is formulated to solve the problem at multiple frequencies.

Three-dimensional wire Bragg grating

In this extension to the classic Bragg grating problem, a three-dimensional wire Bragg grating is considered. The problem setup is shown in Figure 5.4a and consists of a rod 4 cm long with a square cross section of 1cm x 1cm. The domain is discretized into 10,000 brick elements with free lateral sides and viscous damping boundary conditions at the two ends to make it effectively infinite in length. A uniform harmonic load of 1.6MHz is applied at one of the ends to introduce a pressure wave as well as more complicated surface and edge modes (see, for example, [120]) that travel down the length of the wire. Each element in the computational domain is assigned its own design variable allowing it to change its material properties independently between aluminum and silicon; however the non-reflecting boundary conditions have constant material properties of silicon. The objective function is formulated as (4.27) and minimized with the set of objective nodes being those that lie on the boundary of the computational domain opposite the harmonic load. The resulting material layout obtained from topology optimization is shown in Figure 5.4b, which shows material property isosurfaces. Parts of the wire enclosed by red surfaces indicate the presence of silicon while those between blue indicate aluminum. An important aspect of this result is the influence of the finite lateral boundaries and associated surface waves on the material distribution. Whereas using the Bragg condition would result in a series of planar material interfaces along the length of the wire, the presence of surface modes and the difference in wavespeed between the surface and bulk modes results in non-planar interfaces. Figures 5.4c and 5.4d show the wave field in the homogeneous and optimized material domains, respec-

tively. In the former the waves pass through the wire, while in the latter neither the bulk nor surface waves are able to pass and are reflected.

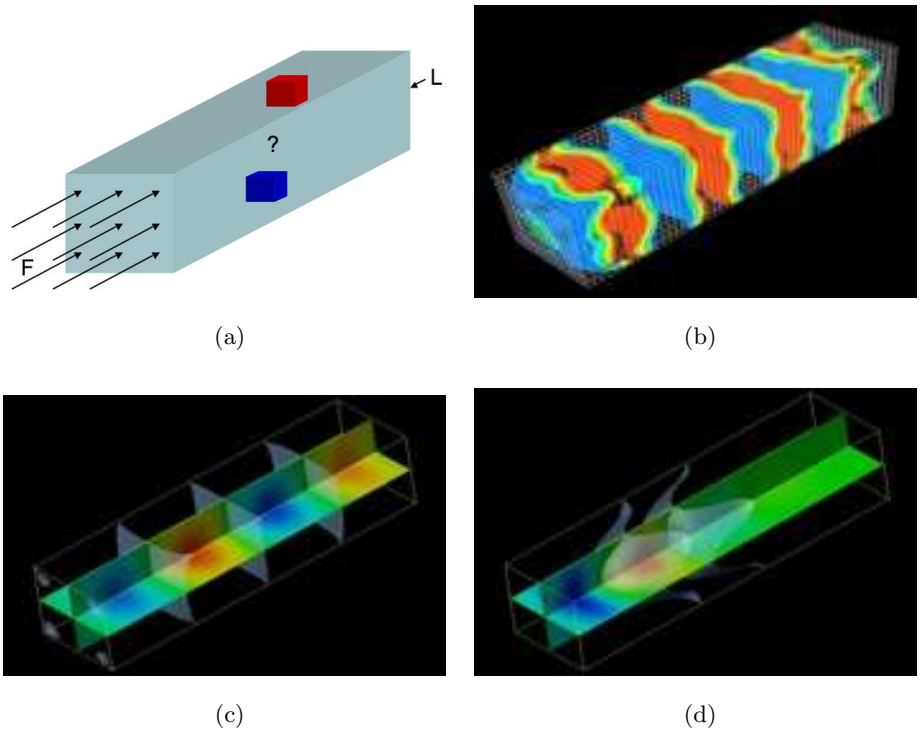

Figure 5.4: (a) Topology optimization problem setup for a long square wire Bragg grating with harmonic load on one end of the wire and optimization objective node set at the other end. (b) Results of topology optimization for a 3D Bragg grating wire. Surfaces indicate interfaces between volumes of silicon and aluminum. Volumes enclosed by red surfaces indicate the presence of silicon while blue surfaces indicate aluminum. The material distribution differs from a typical Bragg grating because of the influence of the surface waves. (c) Wave field shown by displacement magnitude isosurfaces and slices through a homogeneous material is (d) filtered when it passes through the final design.

Surface wave filter

In this example, a two-dimensional problem of a layer on a substrate is considered

and the use of a patterned thin film to impact the propagation characteristics of surface waves is explored. Specifically, a surface wave is excited via a harmonic load normal to the free surface. In a homogeneous half-space this will generate a Rayleigh wave that propagates outward from the source along the surface with the amplitude not being affected by the propagation distance. The Rayleigh wave will carry about two-thirds of the energy radiated from the source, but in addition, bulk shear and compression waves will be generated [62]. The objective is to seek the material layout of the thin film that will filter the surface wave at a given frequency or range of frequencies; this is analogous to the Bragg grating problem but for surface waves.

In the setup of the problem, the computational domain consists of a rectangular region 2.5 cm deep and 8 cm long with a free surface on top and PMLs surrounding the other three boundaries to create a computational two-dimensional half space (Figure 5.5). A 5mm film region at the top of the domain serves as the design domain within which the optimal layout of silicon and aluminum will be determined. The remainder of the computational domain, the substrate, is silicon with material properties fixed throughout the design optimization process. The entire computational domain is modeled with 120,000 elements. Within the film design variables are assigned to 0.1mm wide columns of elements so that each column will have the same material properties. This allows for what would be a manufacturable design using standard thin-film processes. The 0.61 MHz harmonic excitation load is applied in the vertical direction at the upper left corner of the computational domain. A "runway" region is created between the source and the design domain to allow for a Rayleigh wave to fully develop and to minimize the influence of bulk waves in the optimization process. Another runway is also created after the design domain and before the set of optimization objective nodes (denoted by L in Figure 5.5) for the same reasons. The wavefield in a homogeneous material for this geometry is shown in Figure 5.6a. The objective function is formulated as (4.27) and minimized so that surface wave energy will not reach this location at the

applied frequency.

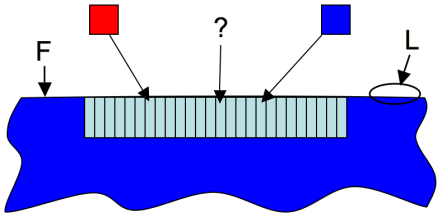

Figure 5.5: Problem setup for a surface wave filter based on thin film etching and deposition on a halfspace. Elastic surface waves are excited by a harmonic force f at the left, pass through the thin film with the objective of having no energy reach objective location L.

Two questions are investigated for the optimization of this surface wave filter. The first question is: How does the effectiveness of an optimized filter compare to that of a filter created from simple Bragg grating ideas, i.e. a regular, patterned structure based on the Bragg condition? The second question is: Using topology optimization is it possible to create a larger band-gap while keeping the same effectiveness, not increasing the domain size, and not changing the problem characteristics?

To answer the first question, a finite regular structure is first created using Bragg condition for the Rayleigh wavelength at the design frequency of 0.61 MHz. The transmission of energy through the domain is then calculated over a range of frequencies. This design is shown in Figure 5.6b, along with the wavefield through this structure. The results of the optimization problem are then shown in Figure 5.6c. The transmission spectrums comparing the two designs in Figure 5.7 show only a weak band-gap for the Bragg grating design while the optimized design is much more effective even though the design is not strictly periodic.

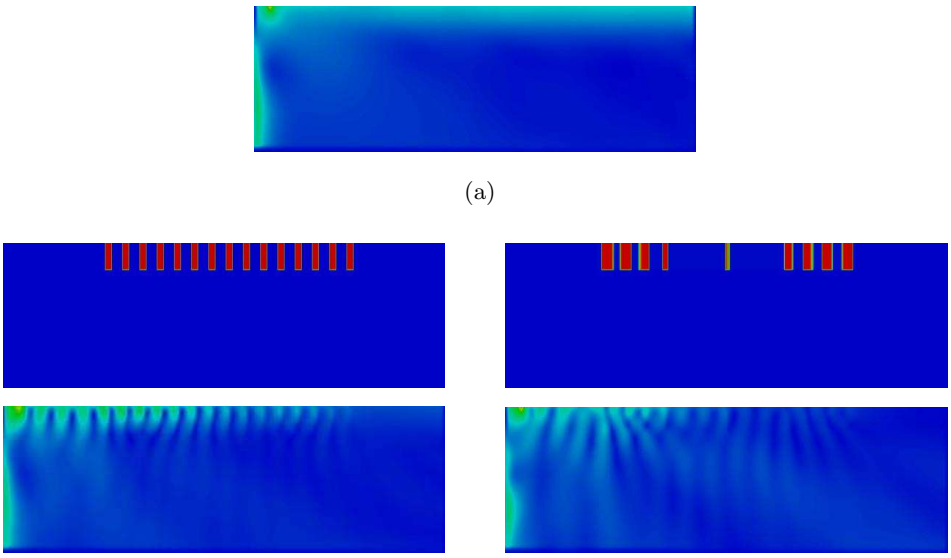

(a)

(b) (c)

Figure 5.6: (a) Wavefield in homogeneous medium of this configuration. Material layout of silicon (blue) and aluminum (red) for surface wave filters (top) and corresponding wavefield (bottom) for designs created using (a) the Bragg condition and (b) topology optimization.

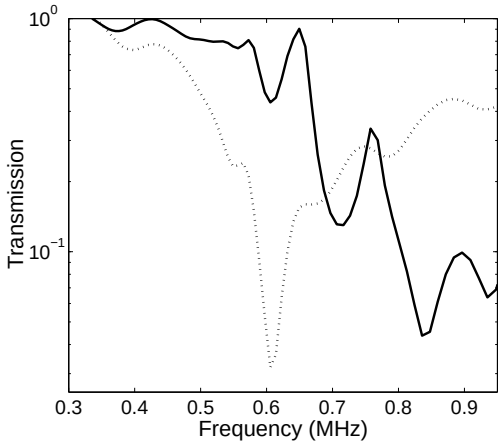

Figure 5.7: Transmission as a function of frequency for the Bragg grating (solid) and optimized (dots) designs.

In order to answer the second question, two additional optimized structures were

created at frequencies 5% below and 5% above the aforementioned design frequency. The resulting structures are shown in Figures 5.8a and 5.8b, respectively. If the three optimized structures of this example were lined up in series then a broader band-gap centered at the middle frequency would be created, but the structure would be three times the length. Instead of doing this, a new problem is formulated that takes all three frequencies (taken as three different load cases) into account but solves the problem on the same sized structure. This results in the material layout in Figure 5.8c and a transmission profile and associated band-gap shown in Figure 5.8d. While the widened band-gap design is not as effective as the individual optimized band-gap structures, it still performs better than the Bragg grating structure over that range of frequencies. It is important to note the non-regularity of the material layouts for the optimized designs. While a Bragg grating is intended to reflect an incoming wave by having material interfaces located at half-wavelength multiples for an incoming wave, a more complex mechanism seems to be at work in these designs.

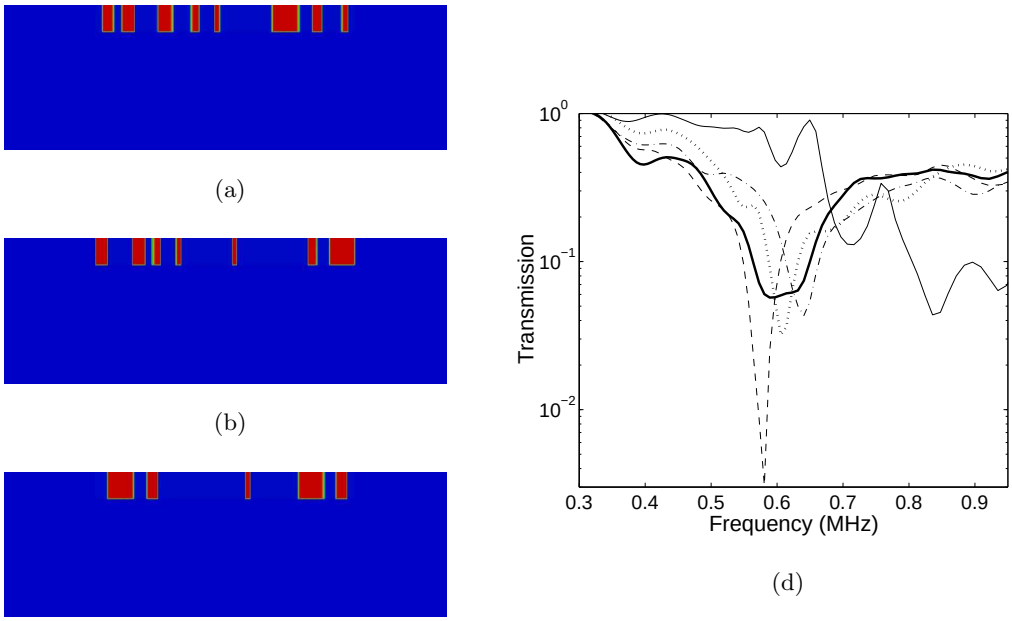

Figure 5.8: Optimized designs for surface wave filters at (a) -5% and (b) +5% of the original design frequency of 0.61 MHz as well as (c) the widened band-gap case that takes all three frequencies into account in the objective. (d) The frequency sweep of surface wave transmission through the Bragg condition structure (solid), the optimized structure at the same design frequency (dots), optimized structures at -5% (dash) and +5% (dash-dot) of the design frequency, and the optimized structure which provides a widened band-gap that covers all three frequencies and still improves on the regular structure (bold solid).

Surface wave band-gap material

With a similar goal in mind as the previous problem, the design of a unit cell for a surface wave band-gap material is desired here. The problem setup is similar to the previous problem with the exception that eight 1mm x 1mm unit cells are placed side by side within a 1mm thick layer on top of the substrate. The goal is to find the distribution of silicon and aluminum within the unit cell that minimizes the amount of wave energy that is allowed to pass through it. The substrate is modeled 1.5mm

thick and is surrounded by PMLs to simulate the computational halfspace. Within each unit cell, which is 50 elements thick and 25 elements wide, the design variables are mirrored so that each cell is symmetric, resulting in only 625 design variables in total. A 0.48MHz surface load and a 1mm runway precede the series of unit cells and another 1mm runway follows and contains location of the objective function, which serves to measure the surface wave transmission through the unit cells by measuring the norm of the displacements. The initial design is started with all design variables at a value of 0.5.

The resulting material layout for this optimization problem is shown in Figure 5.9a. The pattern that develops looks similar in structure to the typical band-gap material for bulk waves in that it is composed of alternating square-ish inclusions of aluminum embedded within the silicon host. This is unusual because the inclusions formed themselves independently within each of the larger unit cells. The important difference, however, is that at the free surface the inclusions are much thinner. The depth of these surface inclusions also seem to coincide with the depth of the characteristic crossing point for the surface wave displacements at this frequency. The crossing point is the location where surface wave displacements parallel to the surface are zero and the wave motion changes from retrograde to not retrograde (see Graff [62]). The importance or correctness of this observation, however, is unknown and has not been quantitatively verified. The wavefield in a homogeneous domain and the final design are shown in Figures 5.9b and 5.9c, respectively. A plot of wave transmission for a range of frequencies around the design frequency is also given in Figure 5.9d. The transmission at low frequencies that is higher than unity is likely due to reflections of bulk modes produced by the load that are either converted into surface waves or picked up at the receiver end of the structure. This inability to isolate certain modes of propagation is one of the concerns of using time-harmonic problems to design band-gap materials.

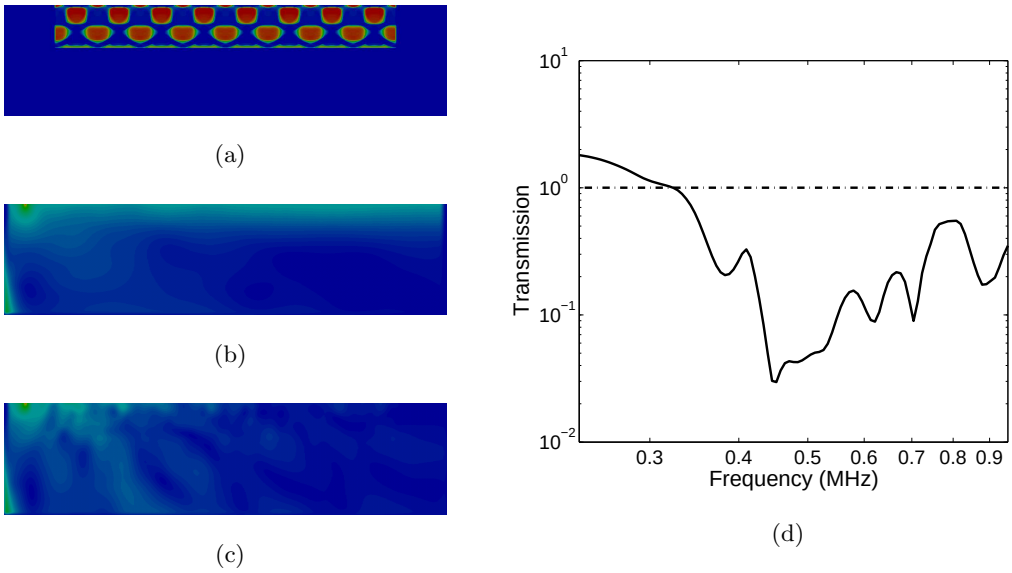

Figure 5.9: (a) Final design of a surface wave device using unit cells. (b) Wave field norm in homogeneous silicon. (c) Wave field norm in the final design showing a drastic decrease in wave energy reaching the far end of the domain. (d) Transmission plot of this design for a range of frequencies also shows a drop in wave transmission, particularly at the design frequency of 0.48 MHz.

5.4.3 Band-gap material examples

The following set of examples illustrate the creation of band-gap materials via topology optimization. The goal of these examples is to enlarge existing or create new band-gaps through manipulating the eigenvalues that make up the dispersion relation.

Optimization of published results for in-plane band-gap materials

Starting with the idea from the verification example of section 5.3.3, topology optimization is used to see if it is possible to create band-gaps without the restriction of using a circular inclusion as in the original design. Two problems are considered here, the first is formulated to create a band-gap between the fifth and sixth modes, while the second is to create a band-gap between the eighth and ninth. The problem setup for is shown in Figure 5.10. For both problems, the initial solution is randomly generated and

(5.11) is used as the objective function with the wavevector space discretized into eight wavevectors. In the solution to the first problem, the final band-gap is from 40-54 MHz, smaller than the band-gap for the circular inclusion in the verification example, but shifted significantly lower in frequency making the relative size of the band-gap larger. Additionally, the small band-gap between modes three and four disappears as compared to the original design. This is shown in Figure 5.11a. In the second problem, creating a band-gap between modes eight and nine resulted in a band-gap from 68-78 MHz. Interestingly, a large band-gap between modes five and six is also produced, as shown in Figure 5.11b. The final material layouts for these two examples are quite different with small feature sizes more prominent in the second problem due to higher frequency modes with shorter wavelengths that must interact with the material structure.

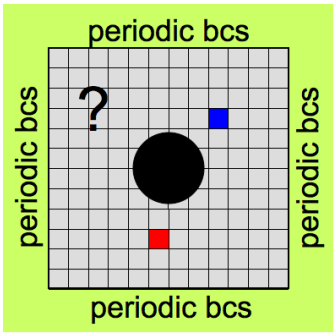

Figure 5.10: Setup for the design of a bulk wave band-gap material.

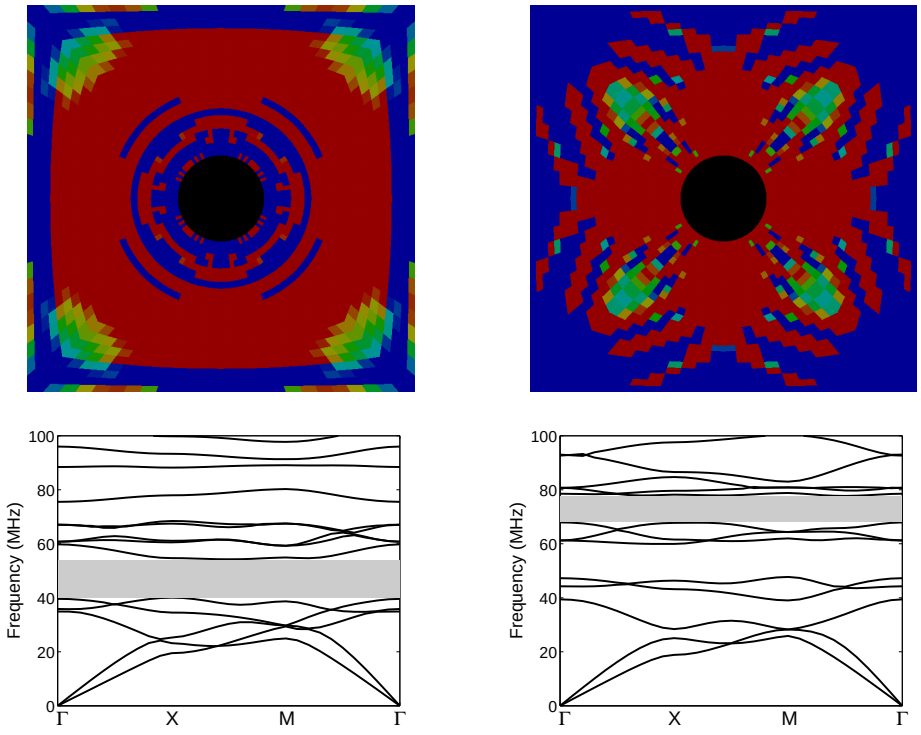

(a) (b)

Figure 5.11: Topology optimization modification of the verification problem design intended to (a) create a band-gap between modes 5 and 6 and (b) between modes 8 and 9. Shown are the (top) final material layouts of tungsten (red) and silica (blue) and (bottom) the corresponding dispersion relations.

Out-of-plane band-gap materials

The band-gap material design given by Olsson et al. [121] was based on an ad hoc design methodology that is typically seen in the literature [87]. In such designs, the band-gap is maximized by using materials with a large acoustic impedance mismatch, which creates more wave reflection at material interfaces. In the previous problem in-plane propagation modes were considered. Here, a series of problems consider out-of-plane wave propagation is considered for which only SH shear modes exist and are decoupled from the in-plane modes. The same geometry and materials are used as in

the previous problem. The goal is to find the material layouts for five unit cell problems such that band-gaps are created between two sequential bands for the first six bands in the dispersion relation. The optimization problem starts with an initial design of homogeneous silica and 18 wavevector points are used. The final material layouts are shown in Figure 5.12. The first few design solutions show a resemblance to many of the simple ad hoc methodology designs found in the literature in that they consist of simply shaped inclusions. For designs where higher modes are created, however, some of the features become smaller and less intuitive in their placement and shape. For example, in Figure 5.12e the features form a non-intuitive clover shape, which produces a very large band-gap of about 20MHz present between the fifth and sixth modes. In one case, shown in Figure 5.12d, a band-gap could not be directly created between two desired modes using topology optimization. Interestingly, however, the design in Figure 5.12a exhibits a band-gap between these modes, indicating that it is possible. The reasons for this are unknown, but it is likely that the algorithm is either stuck in a local optima or progresses to a design where it is not able to create a feasible design space. As will be demonstrated later, it may be possible to fix this situation by using a different initial design.

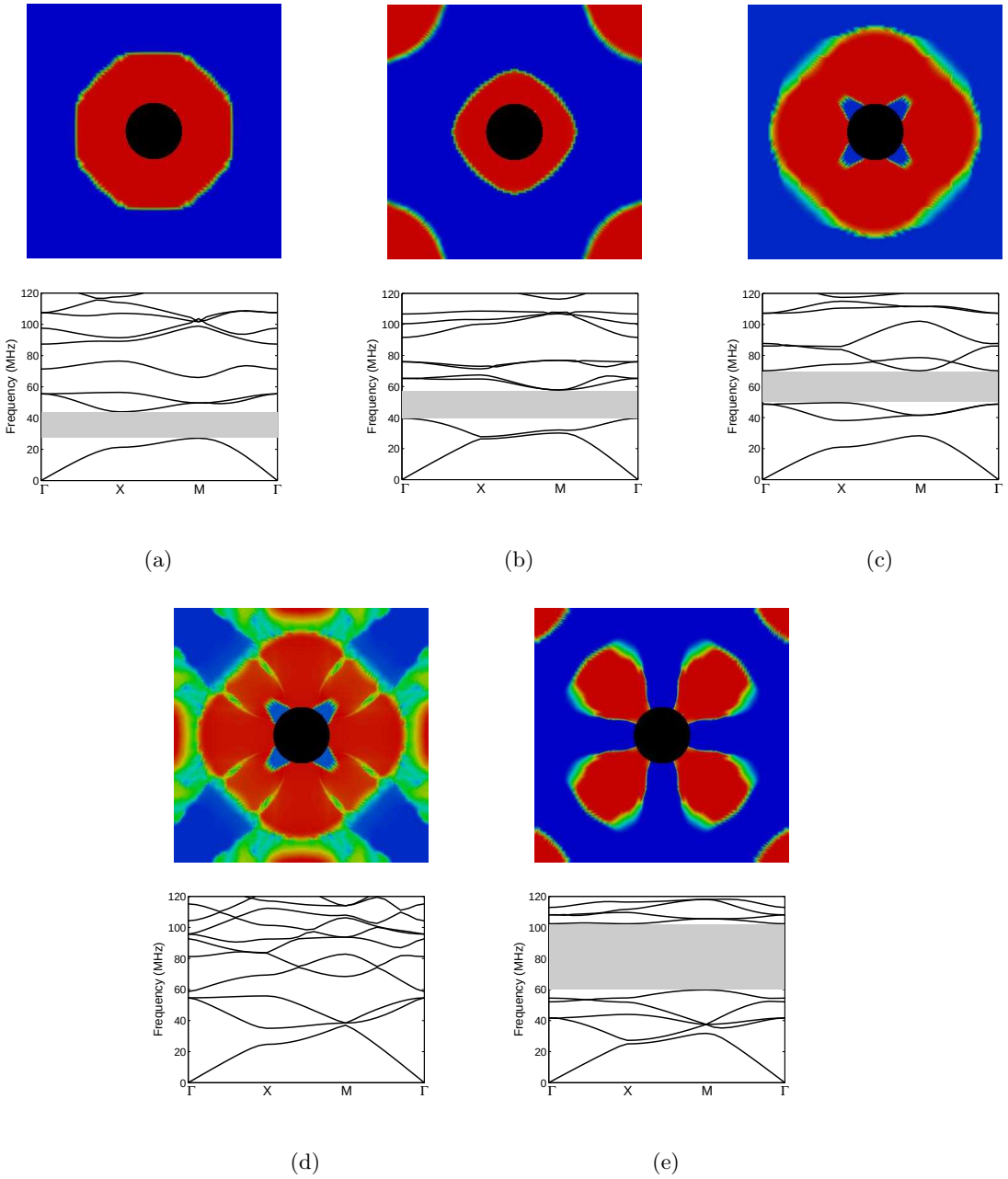

Figure 5.12: Material layouts of silica (blue) and tungsten (red) and dispersion curves for band-gaps created via topology optimization between modes: (a) 1-2, (b) 2-3, (c) 3-4, (d) 4-5 (no band-gap could be directly created), and (e) 5-6.

Beam/plate band-gap material

In a study of how free surfaces affect the band-gap material topology optimiza-

tion problem, a horizontally periodic array of unit cells with free surfaces on the top and bottom is considered. This configuration leads to an infinite beam or plate-like structure (with optimization performed on the through the thickness of the plate or beam) which has the capability of propagating bulk waves along its length as well as other modes including surface waves and Lamb or plate modes. This example therefore not only optimizes for bulk modes but these other modes as well. Periodic boundary conditions are placed only on the left and right sides of a 1m square domain of 50x50 in-plane Brillouin elements while free boundary conditions are on the top and bottom as shown in Figure 5.13. Horizontal mirror symmetry within the unit cell is used in assigning design variables so that the wavevector space can be reduced. The material properties are allowed to vary between Material 1 and Material 2 of Table 5.1. The optimization problem is formulated so that the third and fourth modes would be separated by a maximized band-gap. Figure 5.14 shows the results of this topology optimization problem including the dispersion diagram for a homogeneous material of Material 1, the final design, and the corresponding dispersion diagram with band-gap. The frequency values in the dispersion diagram are normalized such that $\Omega = \omega a/\sqrt{E/\rho}$ where a is the size of the unit cell and E and ρ correspond to the values for Material 1. The material layout of the unit cell clearly shows the influence of plate modes on the optimal solution where the material distribution is different near the free surfaces than in the middle. If only bulk modes were present then the layout would consist of only rectangular blocks of material, similar to that for the classical Bragg grating. This problem is also very similar to the Bragg grating wire example of the previous subsection.

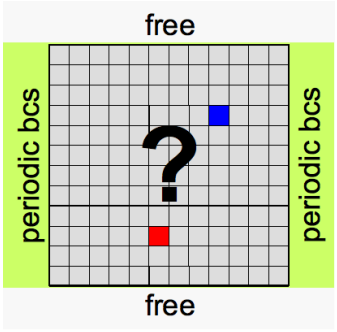

Figure 5.13: Problem setup for a beam or plate band-gap material.

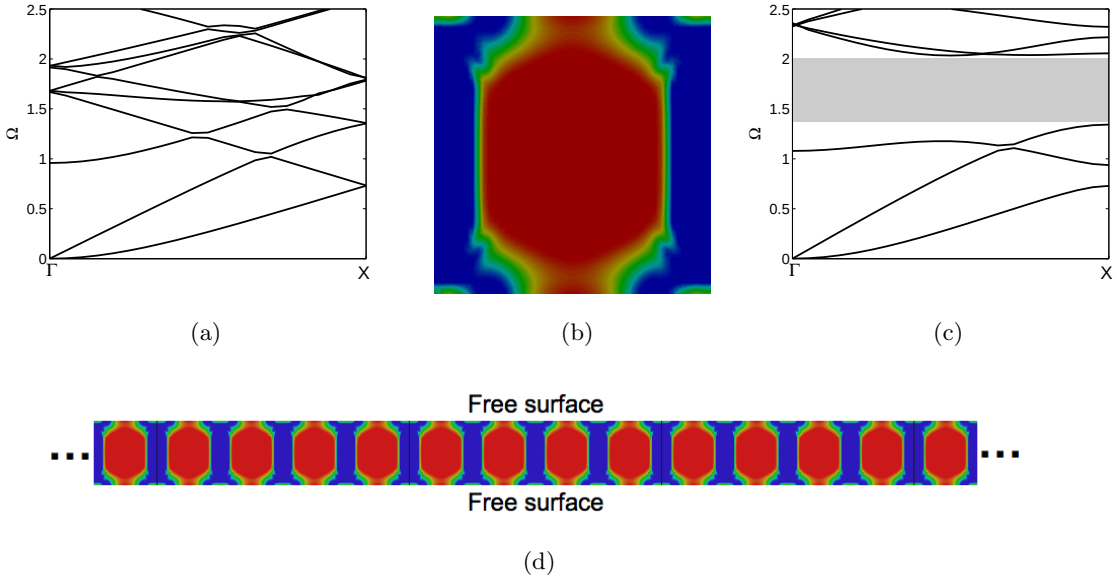

(a) (b) (c)

(d)

Figure 5.14: (a) Dispersion diagram in homogeneous silicon which includes the influence of plate modes. (b) Final material distribution (Material 1-blue, Material 2-red). (c) Dispersion diagram for the optimized band-gap material showing a band-gap between the third and fourth modes. (d) An example of what a structure would look like using this band-gap material. This beam/plate would not transmit wave energy within the frequency of the band-gap.

Mode filtering material

In this example the in-plane bulk band-gap material problem is revisited with a

twist on the objective function. The problem setup is shown in Figure 5.16 where the materials used are Material 1 and Material 2 of Table 5.1. Rather than trying to create a band-gap between two adjacent modes, the goal here is to create a band-gap such that only one mode of propagation exists within a certain frequency band. To do this, the objective function 5.11 is modified so that the third eigenvalue corresponding to the wavevector point Γ as well as the fourth eigenvalues elsewhere are pushed to higher values. At the same time, the third eigenvalues for the wavevector points between X and M and the second eigenvalues elsewhere are pushed to lower values. The idea is to create a region where only a single shear mode exists by creating a band-gap for all other modes. The resulting material layout and dispersion diagram are shown in Figure 5.16. In the dispersion relations a partial band-gap is present between 117 kHz and 135 kHz, where only a shear mode exists.

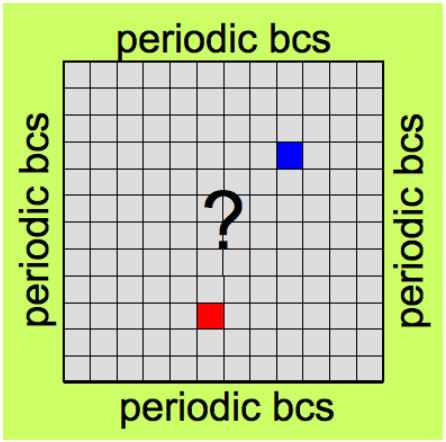

(a)

Figure 5.15: Problem setup for a mode filtering material.

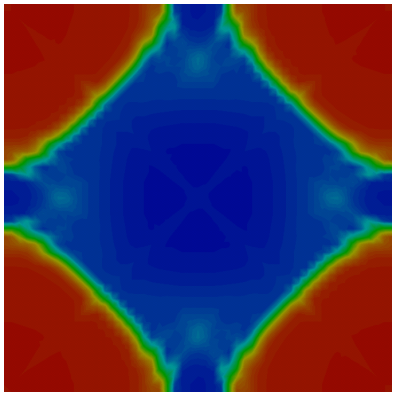

(a)

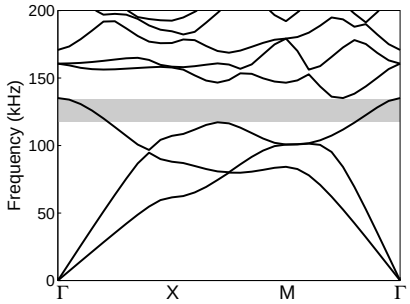

(b)

Figure 5.16: (a) Material layout of a mode filtering material results in a frequency band where only shear waves will pass through the material.

To illustrate the mode filtering capabilities of this material, a slab consisting of three layers of the mode filtering material is placed in a domain of Material 1 with periodic boundary conditions on top and bottom and viscous damping boundary conditions on the left and right as shown in Figure 5.17a. Time-harmonic pressure and shear waves are excited on the left side at a Frequency of 125.9 kHz, which corresponds to the middle of the filtering band. The resulting wavefields are also shown plots of the complex norm magnitude of the displacements and the Poynting vector magnitude in Figure 5.17. For the shear wave the wave passes through the material, while for the pressure wave the majority of the wave is reflected. More of the wave energy would be reflected if more layers of the mode filtering material were used. These examples

demonstrate how topology optimization can be used to design for not only frequency selective behavior but also a potentially desirable mode selective behavior in a material.

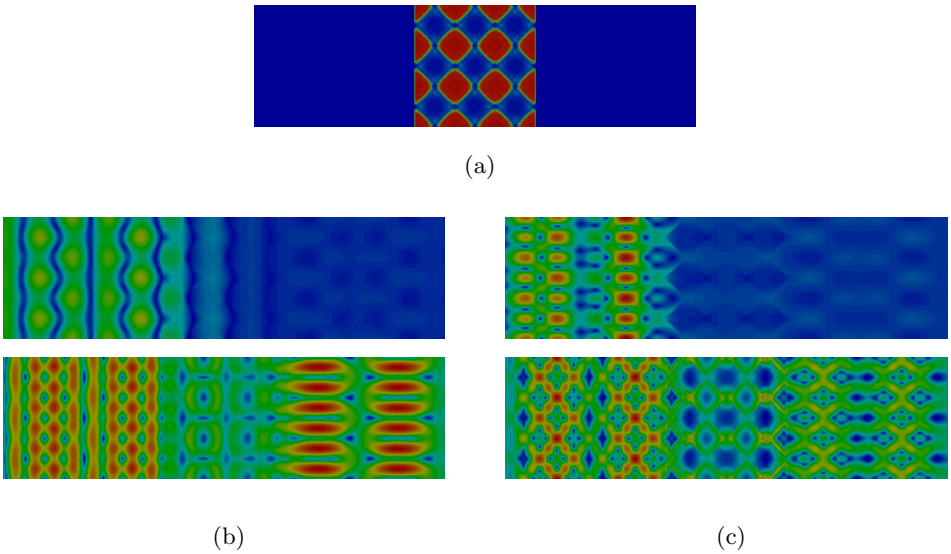

(a)

(b) (c)

Figure 5.17: (a) Illustration setup for a slab of mode filtering material. Pressure (top) waves pass through and shear (bottom) waves do not as shown in the fields for the (b) complex norm magnitude of the displacements and (c) Poynting vector magnitude.

5.5 Methodology Refinement Studies

This section details some unreported issues and observations in solving band-gap material topology optimization problems. These issues aim to provide a greater understanding of band-gap material topology optimization problems.

5.5.1 Band-gap material objective formulation

In previous uses of topology optimization to create band-gap materials, different objective functions were used. Bendsøe and Sigmund [11] and Sigmund and Jensen [146]

use an objective formulated as:

$$\begin{aligned} &\max_{s_i} \beta \\ &s.t. \ \left(\mathbf{K}\left(\mathbf{k}\right) - \omega^2 \mathbf{M}\right)\mathbf{u} = \mathbf{0} \quad \mathbf{k} \in [\Gamma - X - M - \Gamma] \\ &\left[\omega_{j+1}^2\left(\mathbf{k}\right)\right]_m \geq \beta \qquad\qquad m = 1 \ldots n_m \\ &\left[\omega_{j}^2\left(\mathbf{k}\right)\right]_m \leq \beta \qquad\qquad m = 1 \ldots n_m \end{aligned} \tag{5.12}$$

where β is a number corresponding to some squared frequency, j is the j^{th} eigenfrequency ω in order of increasing frequency, and m corresponds to the m^{th} wavevector in the n_m-times discretized wavevector space. This objective, they claim, is equivalent to that used Cox and Dobson [29]. This objective formulation, however, suffers from some serious drawbacks and limitations. Firstly, as β is maximized, it only pushes on the upper bound of the constraints (i.e. the smallest of the ω_{j+1}^2 eigenvalues), but the lower bound has no effect unless there is no band-gap in the first place at which point it can serve to create one. As far as can be inferred from the limited information given in the papers, however, the initial design started with a band-gap as was the intended case in [29], and so the lower bound was likely never used. Secondly, this objective is not guaranteed to produce a band-gap as the lower edge of the gap is allowed to follow the upper edge without penalty, thus the objective is never able measure whether a finite band-gap actually exists. The modified objective function 5.11, on the other hand, improves on the former in that β_2 pushes the upper bound up while at the same time β_1 pushed down on the lower bound independently. This allows a band-gap to be created directly between any two modes. It also has the advantage that it is a direct measure of the band-gap size and can be used where there is not initial band-gap in which a feasible solution is created in moving the constraints.

An interesting aspect of this problem exists for the special case when trying to separate two modes where one is tied to a rigid body mode (i.e. $\omega = 0$ at $\mathbf{k} = \Gamma$). In this situation there exists an inherent upper bound on the lower mode through the physics of the problem. As an informal proof: there exists an upper bound on the wavespeed in

the problem, which is equal to the wavespeed c of the faster mode (the pressure mode) of the two design materials. The longest path the wave can take corresponds to the wavevector point $\mathbf{k} = M$ on the unit cell (see Figure 5.1) for which the corresponding frequency is $\omega \leq \mathbf{k}c \mid_{\mathbf{k}=M}$, which creates an upper bound on the lower (rigid body rooted) mode. When this is the case then 5.12 works well because when β reaches this inherent upper limit a band-gap must be created in order for β to increase.

5.5.2 Band-gap material optimization guidelines and local optima

An important observation for band-gap material problems is that they are highly dependent on initial design. Starting with a design that already has a band-gap is an obvious advantage and can produce good results as shown by Cox and Dobson [29], Bendsoe and Sigmund [11], and Sigmund and Jensen [146]. But their ability to create a larger band-gap depends on a preliminary step of choosing a readily known band-gap structure, which already solves the band-gap problem. What if, however, one wants to create a band-gap either from a material with no pre-existing band-gap or between two modes where there is not a band-gap? In this case a more robust objective formulation that does not depend on the presence of pre-existing band-gaps or inherent physical bounds is needed, such as (5.11). The only condition that must be met is that eigenvalue degeneracies must not be present. The obvious solution to this is to start with a random set of design variables. Experience with a random initial designs have generally yielded a reluctance to converge to any solution, or at least have difficulty converging, and often result in designs that have little coherence and large areas of "gray" elements. Starting from a non-random design, however, seems to ease these troubles, not only when trying to make an existing band-gap larger when that case is applicable, but also when trying to create a band-gap between two modes where no band-gap exists.

An indication of the degree to which local optima are present for these problems is shown in Figure 5.18, which is based on the same problem from the out-of-plane

band-gap materials section of 5.4.3. The objective is to create and maximize band-gap between modes two and three, while considering three examples with different initial designs. The first of these examples already has a band-gap, but not between the modes of interest, while the other two start with different homogeneous designs. In the first example, a band-gap of about 18MHz is created, while a band-gap of 25MHz is created in the second example, although the two final designs are completely different and both well converged. In the third example, however, a band-gap is never created, even though the final design is well defined. These results indicate that 1) the final material layouts are not unique but depend on the initial design and 2) even if a well-defined structure develops a band-gap is not guaranteed to be present. Both of these facts reveal that band-gap material optimization problems are non-convex with strong local optima, an issue that must be taken into account when using gradient-based topology optimization to design these materials.

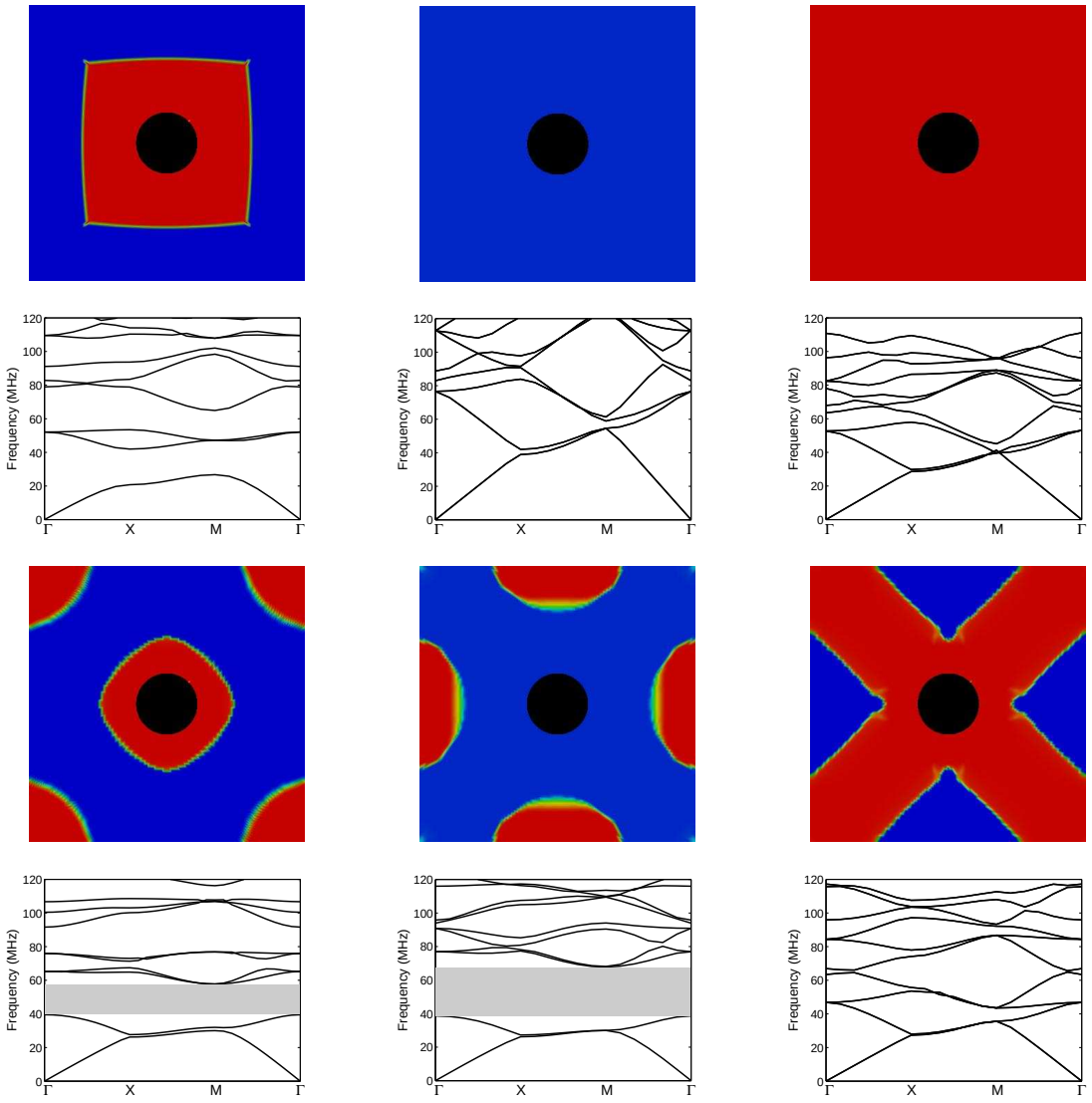

Figure 5.18: Examples of local optimal solutions in band-gap material optimization problems. The problem is set up to create a band-gap between modes two and three starting with three different initial designs. (a) Initial design that already has a band-gap, but not between the modes of interest, and so one must still be created. The final design has a band-gap of about 18MHz. (b) Design starting of material 1 with no initial band-gap results in a different final design with a band-gap that is larger at about 25MHz. (c) Even though a well-defined structure results using an initial design of material 2, a complete band-gap is never found because the optimization algorithm is unable to create a feasible domain.

Also important to note regarding this type of optimization problem is the discretization of the wavevector space. In a dispersion diagram at low frequency there are few modes present, but as frequency increases the number of modes (called the density of states) also increases drastically. As such, it takes a much finer discretization of the wavevector space to discern higher modes from one another. Under topology optimization this is especially true because the constraints depend on constraining the whole mode, which requires a high degree of resolution when a mode undulates significantly. Experience has shown that high modes with low wavevector resolution have difficulty converging to a clear "0-1" solution. Mesh resolution suffers from a similar issue, primarily because for higher modes the mode shapes and wavelengths are smaller, which often correlates with a smaller feature size in the band-gap material. As a result, designing band-gap materials with topology optimization at higher frequencies with the same unit cell size will require much higher resolution in both the physical and wavevector spaces.

5.5.3 Surface wave band-gap material problem

Given the successful design of a variety of band-gap materials using topology optimization in bulk wave and plate wave geometries, it is only natural to attempt to create surface wave band-gap materials using the same technique. The setup for this problem is shown in Figure 5.19. The difficulty with this problem is in modeling the infinite boundary condition at the bottom of the domain. There exist two options for this: viscous damping boundary conditions and PMLs. The analysis for this type of problem was shown previously by Hofer et al. [74] in which they use viscous damping boundary conditions. In replicating their results, it was found that while the correct eigenvalues were found, the viscous damping boundary conditions did not correctly model an infinite boundary as shown by the eigenvectors. The modes revealed by the eigenvectors are shown in Figure 5.20 for what should be a Rayleigh wave in a homogeneous material. From this figure, it is clear that two Rayleigh waves form, one

at the top and one at the bottom surface, which explains why the correct eigenvalues were found for the problem. Also noticeable from these figures is that the viscous dampers slow the surface wave on the bottom surface, which indicates that they are working, but not as intended. While it is possible to find the surface wave modes for this problem, using these results for design purposes is not possible because both the top and bottom surface waves would interact with the design domain, which would not provide the correct modeling conditions for the problem we want to solve.

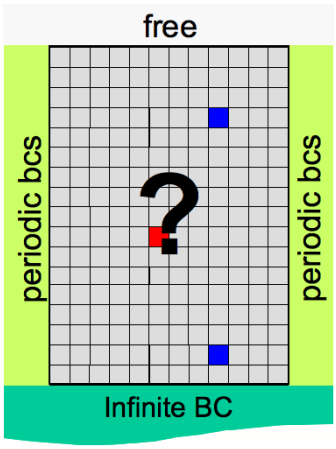

Figure 5.19: Unit cell setup for the design of a surface wave band-gap material.

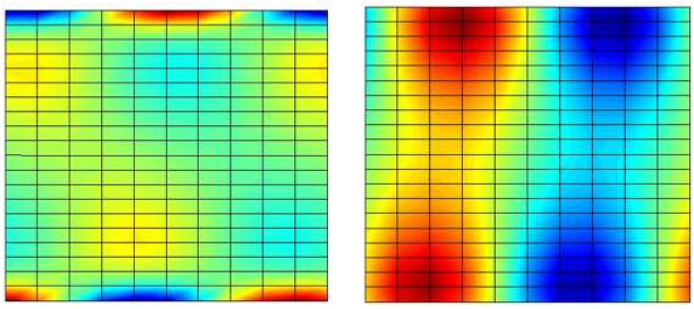

(a) (b)

Figure 5.20: Wavefields for (a) x- and (b) y-displacements from the eigenvector solution for the surface wave band-gap problem with viscous damping boundary conditions.

In another attempt to correctly model this problem, PMLs were used to model the infinite boundary condition. In this case, the PMLs create many spurious modes that are unfortunately not distinct from the modes of interest. The distribution of eigenvalues in complex space is shown in Figure 5.21 for both the viscous damping boundary conditions and the PMLs. While the viscous damping boundary conditions provide the correct eigenvalues as noted previously, the eigenvalues of the spurious modes of the PMLs are all over the place, although the eigenvalues of interest can be seen in the background of the figure. This makes the solution of this problem with PMLs intractable. As a result, the design of surface wave band-gap materials using topology optimization is not possible using these analysis techniques and a new analysis method will be needed in order to solve this problem.

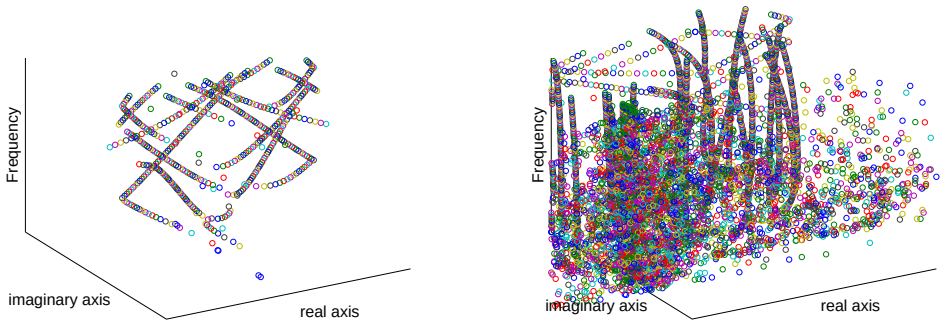

(a) (b)

Figure 5.21: Distribution of eigenvalues for real an imaginary parts of the wavevector for a homogeneous material using (a) viscous damping boundary conditions and (b) PMLs to approximate a semi-inifinite domain in the band-gap material problem.

5.6 Summary

In this chapter two variations of band-gap material topology optimization problems were investigated. The first, band-gap structures, were designed by minimizing the

amount of wave energy passing through the material through a measure of its transmission. In the second, band-gap materials, the dispersion relation was directly manipulated using a new objective function whose benefits over previous functions was discussed. While the solution methods for these two problems were completely different, similarities were found in the results. This was particularly illustrated through problems with free surfaces. In these problems, such as the wire Bragg grating and the beam/plate band-gap material, the presence of surface waves and modes had a significant effect on the final design, especially near the surfaces. These modes, and their variation on the Bragg condition, were thus the primary design drivers for these types of problems. In a variation of the band-gap material problem, the design of a mode filtering, or mode selective, material was demonstrated. This example showed that the band-gap material problem formulation is not limited to only band-gap material problems, but can be extended to serve other purposes. Also discussed were some limitations of the methodology for band-gap materials. First and foremost is the presence of strong local optima where it was shown that three different initial designs resulted in three different final designs, one of which is infeasible. A second issue with these problems was described in the attempt to design a surface wave band-gap material. While this may eventually be overcome, in its current state it represents an intractable problem for topology optimization.

Chapter 6

Topology Optimization of Wave Propagation and Vibration in Piezoelectric Solids

6.1 Introduction

In this chapter a general methodology is developed to analyze and design wave propagation and vibration phenomena in systems incorporating piezoelectric solids. These include vibrating piezoelectric energy harvesting systems based on multilayer plate and shell structures with piezoelectric layers coupled to an external harvesting circuit as well as waveguides and band-gap structures using piezoelectric materials. The approach facilitates the design of piezoelectric systems by tailoring the layout, both in the plane and through the thickness, of single or multilayer structures consisting of structural layers, piezoelectric layers, electrodes, and electrical circuit parameters. Objectives can be formulated in a flexible algebraic manner, and include, for example, open circuit voltage, power output/dissipation, and functions of displacements. While the design of waveguides and band-gap structures is not new, the methodology for using piezoelectric materials in such structures is new. This is also an original methodology for the optimal design of piezoelectric systems by using topology optimization to design both the layout of piezoelectric and structural materials on layered plate harvesting structures as well as the external circuit to which it is connected. The goal of this chapter is to explore the use of piezoelectric materials in dynamic systems, developing a methodology to solve both wave propagation and vibrations problems.

This chapter is organized as follows: the following section details the mechanical, piezoelectric, electrode, and circuit models and their formulation in the finite element method/lumped parameter approach, including how the various fields are coupled. This modeling approach is then validated through comparison to experiments in the literature for both vibrating beam and plate structures. This is followed with application examples that demonstrate the versatility of the approach and explore the behavior of piezoelectric energy harvesting and wave propagation systems. Finally, the findings of this chapter are summarized.

6.2 Analysis

Although the analysis approach outlined herein admits both shells and plates, the structures will be referred to as plates in the following, even if they are curved. In the analysis it is assumed that both the structural and electrical responses of the systems are linear and excited by a harmonic load, allowing for time-harmonic analysis. The finite element method is used to model the fully coupled components of the piezoelectric structure, namely the structural dynamics, electromechanics, and electrode conduction, while a lumped parameter approach is used to model the circuit dynamics (see Figure 6.1). An important feature of the approach is the explicit modeling of the feedback from the circuit to the piezoelectric structure in addition to the response of the circuit. The piezoelectric finite element is a layered plate formulation similar to that described by Marinkovic et al. [109], but extended to include electrode conductivity and for use with topology optimization.

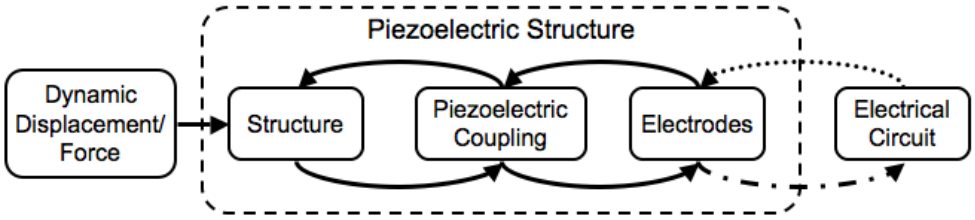

Figure 6.1: Components of a piezoelectric structure as well as their coupling, including the coupling to (dash-dot line) and feedback from (dotted line) the circuit.

6.2.1 Field equations

The piezoelectric model can be separated into three sub-models: the mechanics and coupled electromechanics of the piezoelectric structure, electrical conduction in the electrode, and the electrical circuit model. These sub-models are then coupled through their individual electrical interface conditions. The electrodes are explicitly modeled so that electrical connectivity is maintained between desired parts of the model (e.g. the piezoelectric material and circuit), especially as the model changes during the topology optimization procedure. In the piezoelectric mechanical/electrical model, the mechanical and electric field equations of the layered plate piezoelectric structure are written as:

$$\begin{aligned} \nabla \cdot \mathbf{T} &= \rho \ddot{\mathbf{u}} \\ \nabla \cdot \mathbf{D} &= 0 \end{aligned} \tag{6.1}$$

where $\mathbf{T}$ is the stress tensor, ρ is the mass density, $\mathbf{u}$ is the displacement vector, and $\mathbf{D}$ is the electrical displacement vector. The mechanical and electrical fields are coupled through the piezoelectric constitutive law:

$$\begin{aligned} \mathbf{T} &= \mathbf{c}^E : \mathbf{S} - \mathbf{e} \cdot \mathbf{E} \\ \mathbf{D} &= \mathbf{e} : \mathbf{S} + \epsilon^S \cdot \mathbf{E} \end{aligned} \tag{6.2}$$

where $\mathbf{c}^E$ is the stiffness tensor at constant electric field, $\mathbf{S}$ is the strain tensor, $\mathbf{e}$ is the piezoelectric coupling tensor, ϵ is the dielectric tensor at constant strain, and $\mathbf{E}$ is the

electric field vector. Following Kirchhoff plate theory where the out-of-plane normal (3-direction), shear, and inter-layer stresses are neglected ($T_{33} = 0$, $S_{32} = S_{31} = 0$) and by neglecting the in-plane electric fields ($E_1 = E_2 = 0$) the constitutive law can be reduced. Similar to Marinkovic et al. [109], the constitutive equation for the i^{th} layer can be written in matrix form as:

$$\begin{aligned}\begin{pmatrix} \mathbf{T}'^{(i)} \\ \mathbf{D}'^{(i)} \end{pmatrix} = \begin{pmatrix} T_{11}^{(i)} \\ T_{22}^{(i)} \\ T_{12}^{(i)} \\ D_3^{(i)} \end{pmatrix} &= \begin{bmatrix} Q_{11}^{(i)} & Q_{12}^{(i)} & 0 & e_{31}'^{(i)} \\ Q_{12}^{(i)} & Q_{11}^{(i)} & 0 & e_{31}'^{(i)} \\ 0 & 0 & Q_{66}^{(i)} & 0 \\ e_{31}'^{(i)} & e_{31}'^{(i)} & 0 & -\epsilon_{33}'^{(i)} \end{bmatrix} \begin{pmatrix} S_{11}^{(i)} \\ S_{22}^{(i)} \\ S_{12}^{(i)} \\ -E_3^{(i)} \end{pmatrix} \\ &= \begin{bmatrix} \mathbf{Q}^{(i)} & \mathbf{e}'^{(i)} \\ \left(\mathbf{e}'^{(i)}\right)^T & \epsilon'^{(i)} \end{bmatrix} \begin{pmatrix} \mathbf{S}'^{(i)} \\ -\mathbf{E}'^{(i)} \end{pmatrix}\end{aligned} \tag{6.3}$$

where $(\cdot)^T$ is the transpose operator and the primed notation $(\cdot)'$ indicates the coefficients are reduced, which are written as:

$$\begin{gathered} Q_{11}^{(i)} = c_{11}^{E(i)} - \frac{\left(c_{13}^{E(i)}\right)^2}{c_{33}^{E(i)}},\ Q_{12}^{(i)} = c_{12}^{E(i)} - \frac{\left(c_{13}^{E(i)}\right)^2}{c_{33}^{E(i)}},\ Q_{66}^{(i)} = \frac{1}{2}\left(c_{11}^{E(i)} - c_{12}^{E(i)}\right) \\ e_{31}'^{(i)} = e_{31}^{(i)} - \frac{c_{13}^{E(i)}}{c_{33}^{E(i)}} e_{33}^{(i)},\ \epsilon_{33}'^{(i)} = \epsilon_{33}^{S(i)} + \frac{\left(e_{33}^{(i)}\right)^2}{c_{33}^{E(i)}} \end{gathered} . \tag{6.4}$$

Using Kirchhoff kinematics, it is assumed that the strains through the total thickness can be written as the sum of the midplane strains $\mathbf{S}_0'$ and the product of the curvatures κ with the distance from the midplane z_c (i.e. $\mathbf{S}' = \mathbf{S}_0' + z_c\kappa$). A constant electric field and a linear potential $\phi^{(i)}$ through the thickness of each layer (i.e. $\mathbf{E}'^{(i)} = E_3^{(i)} = -\frac{d}{dz}\phi^{(i)}$) are also assumed. Applying Hamilton's principle for the layered system of piezoelectric equations results in:

$$\begin{aligned} &\int_S \sum_{i=1}^{n} \int_{h_-^{(i)}}^{h_+^{(i)}} \left(\mathbf{S}'\right)^T \left(\mathbf{Q}^{(i)}\mathbf{S}' - \mathbf{e}'^{(i)}\mathbf{E}'^{(i)}\right) + \mathbf{u}^T\rho^{(i)}\mathbf{u} + \left(\mathbf{E}'^{(i)}\right)^T \left(\mathbf{e}^{(i)}\mathbf{S}' - \epsilon'^{(i)}\mathbf{E}'^{(i)}\right) ds\, dS \\ &= \int_S \mathbf{u}^T\hat{\mathbf{t}} - \left(\phi^{(i)}\right)^T \bar{q}^{(i)} dS \end{aligned} \tag{6.5}$$

where the Neumann boundary conditions are:

$$\begin{aligned} \hat{\mathbf{t}} &= \mathbf{T} \cdot \hat{\mathbf{n}} \\ \bar{q}^{(i)} &= -\mathbf{D}^{(i)} \cdot \hat{\mathbf{n}} \end{aligned} \tag{6.6}$$

and $\hat{\mathbf{t}}$ are surface tractions, $\hat{\mathbf{n}}$ is the unit surface normal, and $\bar{q}^{(i)}$ is the charge per unit area of the i^{th} piezoelectric layer. The total charge $q^{(i)}_{piezo}$ produced by the piezoelectric layer material is then:

$$q^{(i)}_{piezo} = \int_S \bar{q}^{(i)} dS \tag{6.7}$$

where the integration is over the in-plane surface area. See Marinkovic et al. [109] for a similar treatment of the coupled piezoelectric equations.

In the electrode electrical conduction model only in-plane conduction is considered on a per-layer basis. The field equations for each electrode layer are developed using Maxwell's equations under quasi-static assumptions:

$$\nabla \cdot \mathbf{D}^{(i)} = \rho_e^{(i)} \tag{6.8}$$

$$\nabla \times \mathbf{H}^{(i)} = \mathbf{J}_f^{(i)} + \dot{\mathbf{D}}^{(i)} \tag{6.9}$$

with charge density ρ_e, magnetic field $\mathbf{H}$, and free current density $\mathbf{J}_f$. The constitutive law (Ohm's law) for electric conduction is:

$$\mathbf{J}_f^{(i)} = \sigma^{(i)} \mathbf{E}_e^{(i)} \tag{6.10}$$

with conductivity $\sigma^{(i)}$. Assuming an irrotational electric field such that $\mathbf{E}_e^{(i)} = -\nabla\phi^{(i)}$, integrating equation (6.9) over the volume of the electrode, and combining with equations (6.8) and (6.10), yields:

$$\dot{q}^{(i)}_{electrode} = \int_V \dot{\rho}_e^{(i)} dV = \int_V \nabla \cdot \sigma^{(i)} \nabla\phi^{(i)} dV \tag{6.11}$$

where $q^{(i)}_{electrode}$ is the total charge in the i^{th} electrode.

The final sub-model, the electrical circuit, is assumed to be linear and can be generalized as a RLC circuit with a series resistance R, capacitance C, and inductance

L subject to a potential difference $\Delta\phi$. A methodology for the analysis of piezoelectric systems connected to nonlinear circuits such as full-bridge rectifiers is described in appendix A. The analysis of nonlinear circuits is complex and beyond the scope of the work here, although many of the same principles discussed in this chapter are equally applicable. The dynamics of a linear circuit are described by:

$$\Delta\phi = \frac{1}{C} q_{circuit} + R\dot{q}_{circuit} + L\ddot{q}_{circuit} \tag{6.12}$$

where $q_{circuit}$ is the electric charge.

The equations of the three sub-models are combined by common Dirichlet boundary conditions and by the conservation of charge within the system:

$$q_{piezo} + q_{electrode} + q_{circuit} = 0 \tag{6.13}$$

which depends on the connectivity of the sub-models and combines equations (6.7), (6.11), and (6.12), integrated in time by assuming a time-harmonic response, to fully couple the piezoelectric structure, the electrodes, and the electric circuit.

6.2.2 Finite element formulation

The finite element method is used to discretize the equations for the electromechanics of the piezoelectric structure as well as the electrodynamics of the electrodes, while for the circuit a lumped parameter model is used. A four-node layered finite element is used where the layers may consist of either pure structural, piezoelectric, or electrode layers. The structural layers are built from four overlapping composite triangular elements [71] composed of coupled 9-dof ANDES membrane [51] and 9-dof bending [110] triangular elements, resulting in 24 structural degrees of freedom per element. The piezoelectric layers use the same structural components coupled to the electric field via piezoelectric coupling (see Marinkovic et al. [109]). In the formulation of the layered element, the middle in-plane strains, curvatures, and electric field are assumed constant

and integration through the thickness is performed in a piece-wise manner using constant constitutive properties for each layer [71]. An arbitrary number of potential degrees of freedom may exist per node through the thickness, allowing for multiple, independent piezoelectric layers. Figure 6.2 illustrates an example layer configuration showing the location of potential degrees of freedom on a layer basis and the linear interpolation of potential through the thickness.

Under time harmonic assumptions ($\mathbf{u} = \mathbf{u}_e e^{i\omega t}$, $\phi = \phi_e e^{i\omega t}$) with excitation frequency ω, the resulting piezoelectric finite element system with structural damping can be written as:

$$\begin{aligned} -\omega^2 \mathbf{M}_e \mathbf{u}_e + i\omega \mathbf{C}_e \mathbf{u}_e + \mathbf{K}_e \mathbf{u}_e \quad + \boldsymbol{\Theta}_e \phi_e \quad &= \mathbf{f}_e \\ \boldsymbol{\Theta}_e^T \mathbf{u}_e \quad + \mathbf{C}_p \phi_e \quad &= \mathbf{q}_e \end{aligned} \tag{6.14}$$

where $\mathbf{M}_e$, $\mathbf{C}_e$, $\mathbf{K}_e$, $\boldsymbol{\Theta}_e$, $\mathbf{C}_p$, $\mathbf{u}_e$, ϕ_e, $\mathbf{f}_e$, $\mathbf{q}_e$ are the elemental mass, damping, stiffness, piezoelectric coupling, and capacitance matrices, with the elemental nodal displacement, potential, force, and charge vectors.

The electrode layers conduct electricity in the plane of the element between voltage degrees of freedom of the same electrode layer with finite conductivity as described by equation (6.11). Each electrode layer is discretized with a four-node bi-linear finite element (see Bathe [6]), which when combined under time harmonic assumptions yields:

$$i\omega \left(-\frac{1}{\omega^2} \boldsymbol{\Psi}_e \right) \phi_e = \mathbf{q}_e \tag{6.15}$$

where $\boldsymbol{\Psi}_e$ is the elemental electrode conduction matrix for all the electrodes.

The time-harmonic form of the electric circuit equation (6.12) can be written as:

$$\left(-\omega^2 \mathbf{R}_e^{\mathbf{M}} + i\omega \mathbf{R}_e^{\mathbf{C}} + \mathbf{R}_e^{\mathbf{K}} \right) \phi_e = \mathbf{q}_e \tag{6.16}$$

where:

$$\begin{aligned} \mathbf{R}_e^{\mathbf{M}} &= \frac{L}{\left(\frac{1}{C} - \omega^2 L\right) + (\omega R)^2} \mathbf{R}^{\mathbf{I}} \\ \mathbf{R}_e^{\mathbf{C}} &= \frac{-R}{\left(\frac{1}{C} - \omega^2 L\right) + (\omega R)^2} \mathbf{R}^{\mathbf{I}} \\ \mathbf{R}_e^{\mathbf{K}} &= \frac{\frac{1}{C}}{\left(\frac{1}{C} - \omega^2 L\right) + (\omega R)^2} \mathbf{R}^{\mathbf{I}} \end{aligned} \tag{6.17}$$

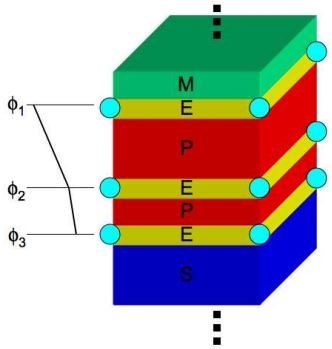

Figure 6.2: An example construction of a piezoelectric layered element composed of (S) structural, (P) piezoelectric, (E) electrode, and (M) mass layers. An arbitrary number of potential degrees of freedom ϕ, marked by blue circles, may exist through the thickness.

and $\mathbf{R^I}$ connects the potential field degrees of freedom in the lumped parameter formulation. Using equation (6.13) to connect equations (6.14), (6.15), and (6.16) yields the final system of equations:

$$\tilde{\mathbf{K}} \begin{pmatrix} \mathbf{u} \\ \phi \end{pmatrix} = \begin{bmatrix} \mathbf{K}_{11} & \mathbf{K}_{12} \\ \mathbf{K}_{21} & \mathbf{K}_{22} \end{bmatrix} \begin{pmatrix} \mathbf{u} \\ \phi \end{pmatrix} = \begin{pmatrix} \mathbf{f} \\ \mathbf{0} \end{pmatrix} \tag{6.18}$$

where:

$$\begin{aligned} \mathbf{K}_{11} &= -\omega^2 \mathbf{M} + i\omega \mathbf{C} + \mathbf{K} \\ \mathbf{K}_{12} &= \mathbf{\Theta} \\ \mathbf{K}_{21} &= \mathbf{\Theta}^T \\ \mathbf{K}_{22} &= -\omega^2 \mathbf{R^M} + i\omega \left(-\tfrac{1}{\omega^2} \mathbf{\Psi} + \mathbf{R^C} \right) + \left(\mathbf{R^K} + \mathbf{C}_p \right) \end{aligned} \tag{6.19}$$

for which the matrices are assembled in the global sense with global system matrix $\tilde{\mathbf{K}}$. The mechanical response of the structure is described by $\mathbf{K}_{11}$, which changes with the layout of materials both layer-wise and in the plane of the plate structure. The matrices $\mathbf{K}_{12}$ and $\mathbf{K}_{21}$ are the piezoelectric coupling matrices, which couple the structural and electrical responses and vary with piezoelectric material layout. The dynamics of the electrical response in $\mathbf{K}_{22}$ are provided by the interaction of the circuit matrices $\mathbf{R^M}$, $\mathbf{R^C}$, and $\mathbf{R^K}$ with the piezoelectric capacitance matrix $\mathbf{C}_p$, which varies with the material layout, and the electrode matrix Ψ, which varies with the electrode conductivity

and topology.

6.2.3 Material interpolation and associated issues

For the design of piezoelectric systems studied in this chapter, simple linear interpolations are used to define the mass density, the stiffness coefficients, and the piezoelectric coupling constant, and the electrode conductivity in each element / layer as explicit functions of the optimization variables:

$$\begin{aligned} \rho^{(i)} &= \left(\rho_{(1)} - \rho_{(0)}\right) s_i + \rho_{(0)} \\ Q_{kl}^{(i)} &= \left(Q_{kl(1)} - Q_{kl(0)}\right) s_i + Q_{kl(0)} \quad 0 \leq s_i \leq 1 \\ e_{31}^{\prime(i)} &= \left(e'_{31(1)} - e'_{31(0)}\right) s_i + e'_{31(0)} \quad i = 1 \ldots (n_s - 1) \end{aligned} \tag{6.20}$$

where the subscripts (0) and (1) denote the lower and upper bounds for the variable corresponding to design variable values of $s_i = [0, 1]$. An illustration of what the corresponding structure could look like is shown in Figure 6.3. It is possible with this framework, but not explored in our examples, to additionally treat the electrode conductivity as variable as a means to design the layout of electrodes on the piezoelectric layers.

When the circuit resistance is also varied in the energy harvester examples a nonlinear interpolation function is used as follows:

$$R = R_{(0)} \exp\left(\ln\left(\frac{R_{(1)}}{R_{(0)}}\right) s_j\right) \quad j = n_s \ . \tag{6.21}$$

This interpolation approach counteracts the large influence of the resistance on the energy harvesting performance that dominates over the influence of the material parameters described above, and thus mitigates numerical problems when solving the optimization problem.

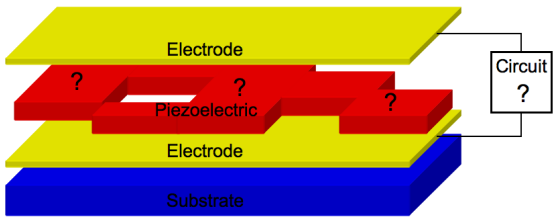

Figure 6.3: Illustration of the problem setup using topology optimization to determine the layout of the piezoelectric layer and the circuit parameters.

Note that in the problem-specific formulation of the topology optimization problem for energy harvesting systems, the dielectric permittivity of the piezoelectric layer is not varied with the other properties of the piezoelectric layer. This is done as a matter of stabilization for the optimization algorithm to overcome scaling differences between the inherent piezoelectric and electrical circuit problems that appear in the optimization problem. In this study only a purely resistive external circuit is investigated, although the piezoelectric material surrounded by electrodes acts as a capacitor thereby making the whole system act like an RC circuit. In standard RC circuits, the maximum power is dissipated for an oscillation frequency $\omega = 1/(RC)$. However, finding the optimal resistance in the case of piezoelectric harvesting is not as easy as satisfying the RC-circuit condition, as demonstrated by Erturk and Inman [41] and Renno et al. [131]. The logarithmic scaling of voltages and currents in RC-like circuits due to changes in capacitance through the dielectric constant is stark in contrast to the generally linear scaling of the voltages and currents from changes in the piezoelectric coupling constant and material layout. Because of this, the optimization process is dominated by the circuit problem and the piezoelectric topology changes little, if at all. To overcome this issue we keep the dielectric permittivity of the piezoelectric layer constant, which makes the system capacitance constant, regardless of piezoelectric layout. While this is a non-physical situation, it can be realized in practice by transferring any non-physical capacitance to an external capacitor in parallel with the piezoelectric plate. As a result,

in optimizing the piezoelectric layout, the capacitance value of this external capacitor is also optimized at the same time, albeit indirectly. This procedure effectively isolates the piezoelectric and electrical circuit problems from each other, thereby allowing the piezoelectric material layout to change without changing the properties of the RC-like circuit.

6.3 Verification

The numerical piezoelectric model is validated by analyzing two problems where analytical solutions and/or experimental results are given in the literature. The first problem is a cantilever beam harvester [40, 42, 44, 45] and the second problem a piezoelectric circular plate [91, 92]. In both of these cases, fully covered cantilevers and plates were considered as well as special cases where only part of the structure was covered by a piezoelectric patch and/or an electrode. In all cases excellent agreement was obtained between simulation results and the analytical solutions and/or experimental results reported in these papers. Two illustrative examples are shown here.

6.3.1 Material properties

The material properties used in the verification examples and the following application examples are given in Table 6.1.

Table 6.1: Material properties used for piezoelectric energy harvesting examples

	Mass density	Stiffness properties	Piezoelectric properties
Piezoelectric (PZT-5H)	$\rho = 5700\ kg/m^3$	$c_{11}^E = c_{22}^E = 127\ GPa$	$e_{31} = -6.63\ N/C$
		$c_{12}^E = 80.2\ GPa$	$e_{33} = 23.2\ N/C$
		$c_{13}^E = c_{23}^E = 84.7\ GPa$	$\epsilon_{33}^S = 1.27e-8\ F/m$
		$c_{33}^E = 117\ GPa$	
Aluminum	$\rho = 2700\ kg/m^3$	$E = 73.0\ GPa,\ \nu = 0.33$	
Mass layer	$\rho = 5700\ kg/m^3$	$E = 0\ GPa$	

6.3.2 Cantilever beam

The first validation example follows the study of Erturk and Inman [44] who use a vibrating bi-morph cantilever beam connected to a circuit for energy harvesting. In [44] the authors develop an analytical model that compares favorably with experimental data. Here the present finite element model is compared to their validated analytical model for the same setup thereby validating our model as well. The setup for the cantilever bi-morph consists of 0.14mm thick brass beam surrounded by 0.26mm PZT-5A piezoelectric layers and two 0.006kg tip masses. The beam is 50.8mm long and 31.8mm wide. The material properties can be found in Erturk and Inman [44]. In order to reproduce their results derived from beam theory with the plate formulation a Poisson's ratio of zero is used in the calculations.

The two piezoelectric layers are connected in series with each other and with an external circuit consisting of a resistor of variable resistance as shown in Figure 6.4. The finite element model consists of a 25 x 15 element mesh of the layered piezoelectric plate elements described earlier. A structural layer is sandwiched between two piezoelectric layers. At the bottom and top, electrode layers with a conductivity of 1.0e4 Ω^{-1} are placed; the conductivity is large enough to model nearly perfect conduction,

but small enough to prevent numerical issues due to ill-conditioned system matrices. The connections between electrodes are modeled with resistive elements, one with the load resistance and the other with a negligible resistance to connect the two inner layers. Lumped masses are included at the beam tip and mass proportional damping of 2.7% is applied, as determined from Erturk and Inman's experiments. Frequency sweeps are performed for harmonic base excitation and the output power through the resistor is calculated for resistivities of 1kΩ, 33kΩ, and 470kΩ. Figure 6.5 shows the power frequency response functions (FRFs) plotting the output power normalized to the square of acceleration, g2, over the excitation frequency. The results are in excellent agreement with Erturk and Inman's analytical solution. The largest output power is obtained for 33kΩ, suggesting that there is an optimal resistance for the external circuit that maximizes the output power.

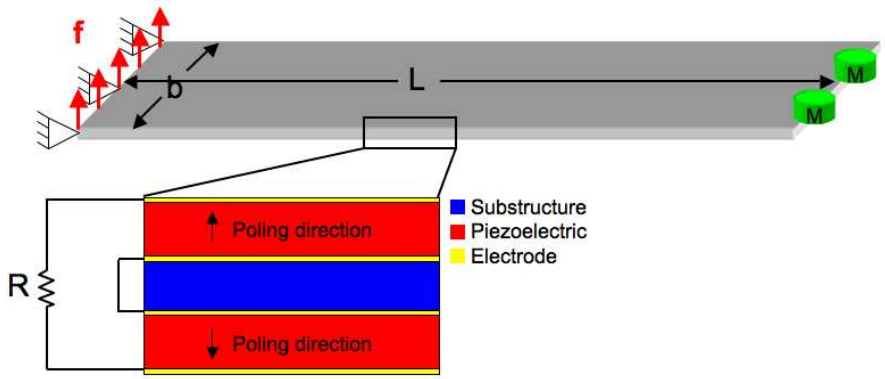

Figure 6.4: Schematic of a cantilever bi-morph used for validation of our modeling approach.

6.3.3 Clamped circular plate

In the second example a $R_2 = 25$mm diameter circular plate that is clamped at the outer edge is considered under static deformation. The plate consists of a 0.127mm thick piezoelectric PZT-5H layer on a 0.508mm thick aluminum substrate. The material

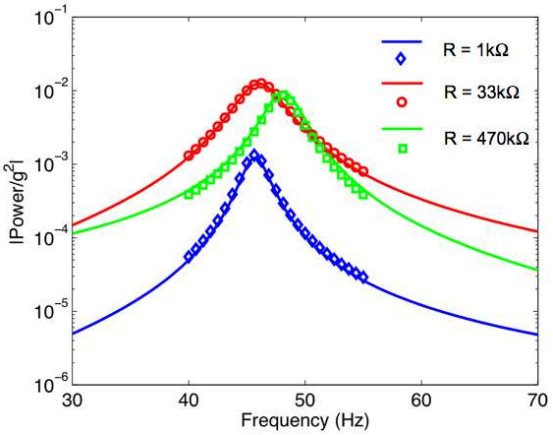

Figure 6.5: Power FRF for a piezoelectric bi-morph cantilever beam for resistances of 1kΩ, 33kΩ, and 470kΩ. Finite element calculations are shown as open symbols while the analytical solutions are shown as solid lines.

properties are given in Table 6.1. An external static pressure is applied to one side of the plate and the resulting open circuit voltage is calculated. This problem can be considered a special case of the dynamic finite element model setup (6.18) such that $\omega \to 0$ and $R \to \infty$. In order to increase the voltage generated by the plate, the material in the PZT-5H layer is arranged such that the piezoelectric polarization (polarity) changes sign/direction (i.e. the coupling constant changes sign) at R_1. Figure 6.6(a) shows the problem setup. This problem was studied by Kim et al. [91, 92] who provided an analytical solution and carried out supporting experiments. The finite element model consists of a mesh of 18,000 elements, which was determined to be adequate by a mesh refinement study. The results are in good agreement with the published experimental data as shown in Table 6.2.

Table 6.2: Generated V_{OC} (in V) vs. R_1/R_2 for ΔP=9.65kPa

R_1/R_2	Experiment	Analysis
0.40	5.31±0.014	5.61
	5.61±0.014	
0.72	8.84±0.039	9.29
	9.26±0.010	

To study the influence of the layout of the piezoelectric layer on the performance of the structure, the radius R_1 is varied and the open circuit voltage plotted as a function of R_1/R_2 in Figure 6.6(b). The open circuit voltage is maximum for $R_1/R_2 = 0.7$. Plotting the mean curvature (arithmetic mean of in-plane curvatures) as a function of radius in Figure 6.6(c) shows that curvature changes sign at $r/R_2 = 0.7$. To avoid charge and voltage cancellation, the polarity of the piezoelectric material needs to be switched at $R_1/R_2 = 0.7$. This finding is consistent with Erturk and Inman [40] and Erturk et al. [45].

In addition to determining the optimum value of R_1/R_2 through a parameter sweep, this example is used to test the topology optimization design methodology by letting the optimizer find the optimum material distribution. The optimization problem is defined to maximize the open circuit voltage by finding the optimal distribution of two materials that differ only in the sign of their piezoelectric coupling coefficients. The design variables interpolate the piezoelectric coupling constant linearly from a positive value to a negative value (i.e. it is either poled upward or downward). While for this axisymmetric problem it would be sufficient to consider only the variation of polarization as a function of radius, in the setup of this optimization problem the design variables define the polarity in the piezoelectric layer independently in each element. Figure 6.6(d) shows this optimal distribution which has a corresponding optimal open circuit

voltage of $9.31V$ at about $R_1/R_2 = 0.71$ (an estimate because of the finite element discretization), which correlates well with the analytical optimal solution provided by Kim et al. [91].

In this example, the layout of the piezoelectric layer has a negligible effect on structural response due to static pressure loading. The regions with positive and negative curvature can be determined and, neglecting small piezoelectric effects, the layout of the piezoelectric layer can be aligned with the curvature distribution. It is shown in the following section that this procedure is not necessarily applicable to problems where the structural response depends on the layout of piezoelectric material. In this case this optimization approach provides a useful tool to find the optimum distribution of piezoelectric material.

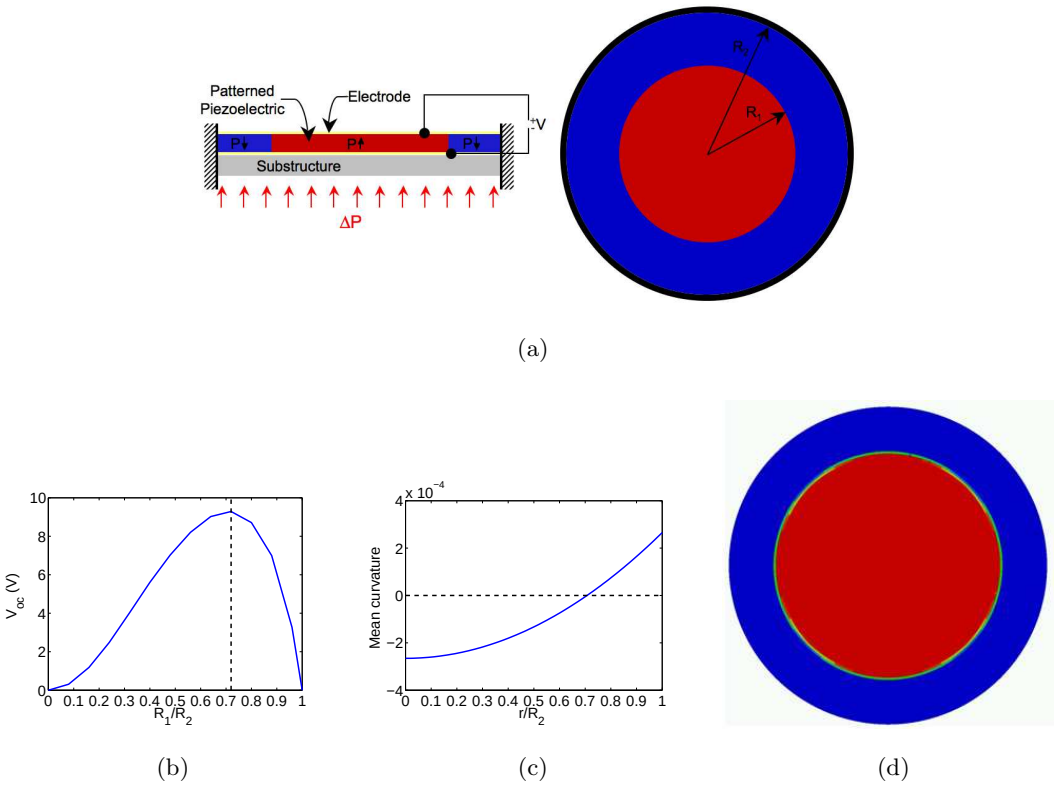

Figure 6.6: (a) Problem setup of a circular plate with a pressure load, (b) open circuit voltage as a function of polarization reversal radius, (c) mean curvature of the plate as a function of radius, (d) optimal piezoelectric polarization layout using topology optimization (red – positive polarization, blue – negative polarization).

6.4 Applications

6.4.1 Objective function and sensitivities

Piezoelectric energy harvesters

The formulation of the piezoelectric energy harvesting optimization problem is quite general and as such can be used to solve a wide range of design problems regarding piezoelectric energy harvesters. In the examples that follow a more restrictive suite of problems are solved that involve determining the layout of piezoelectric patches on an elastic substrate to maximize the harvested power for a given operating frequency (see

Figure 6.3). In addition, the optimal resistance of the harvesting circuit is determined. To this end the objective function is formulated as:

$$z = \frac{|\Delta\phi|^2}{2R} \tag{6.22}$$

which is a measure of the average power dissipated by the resistor. The gradients of the objective can be written as:

$$\frac{dz\left(s_i\right)}{ds_i} = \frac{\partial z}{\partial R}\frac{dR}{ds_i} + \frac{\partial z}{\partial \phi}\frac{d\phi}{ds_i} = -\frac{|\Delta\phi|^2}{2R^2}\frac{dR}{ds_i} + \frac{1}{R}\Re\left(\phi^*\tilde{\mathbf{K}}^{-1}\frac{\partial\tilde{\mathbf{K}}}{\partial s_i}\phi\right) \tag{6.23}$$

which are evaluated by the adjoint method. In the examples studied in the following no inequality or equality constraints are considered and no gradient filtering or penalization techniques are used. The optimization problems are solved with a sequential quadratic programming algorithm [135].

Piezoelectric waveguides and band-gap structure

The formulation of the objective function for the waveguide and band-gap structure problems is the same as that provided in previous chapters, namely complex norm objective function 4.27. The globally convergent method of moving asymptotes [151] is used as the optimization algorithm.

6.4.2 Piezoelectric energy harvester examples

In this subsection four examples are presented that demonstrate the capabilities of the presented approach. The focus is on a suite of examples that cannot yield solutions through analytical beam or plate analysis methods. It is shown how adding a piezoelectric energy harvesting layer can drastically change the response of a system and that simply placing material in regions of positive or negative curvature will not necessarily yield a design that effectively harvests energy. Optimal designs that overcome this problem using this methodology are presented and discussed. It is then shown how the parameters of the harvesting circuit, namely the resistance, affect the power

output of the energy harvesting system. This is followed by a study of how adding a mass layer to the structure changes the response and the optimal design of the plate structure and how it can improve results more than optimizing the piezoelectric layer alone. The final example demonstrates that the technique is applicable to a curved base structure and illustrates the versatility of our approach as not only a design tool but also as a tool for investigating physical trends associated with optimally designed structures. The intent is to show how the approach can be used to explore the general behavior and develop overarching principles through the study of a suite of particular problems in piezoelectric energy harvesting.

Clamped square plate – thickness effects

Here the design of a 10x10cm clamped square plate as shown in Figure 6.7 is considered. The plate is clamped at the middle two-fifths of one side and is subject to a harmonic excitation of 575Hz at the clamped location normal to the plane of the plate, actuated as a unit displacement. The objective of the example is to determine the optimal layout of piezoelectric material on top of a substrate such that the power dissipated by a constant $1.0k\Omega$ resistor is maximized. The initial design for the optimization problem is a plate fully covered with piezoelectric material. This optimization problem is solved for six different thickness ratios of piezoelectric to substrate materials. The piezoelectric is transversely isotropic PZT-5H with thicknesses of $h_p = [0.001, 0.025, 0.1, 0.2, 0.3, 0.5]$mm, while the substrate is aluminum with a constant thickness of $h_s = 1$mm. The finite element model is discretized into a 25x25 element mesh. It was found that for undamped structures, the sudden phase change in voltage and displacement at resonance creates a non-smooth optimization landscape that cannot be traversed efficiently by gradient-based algorithms. In order to alleviate this problem, as well as make it more practical, mass proportional damping of 1% is included.

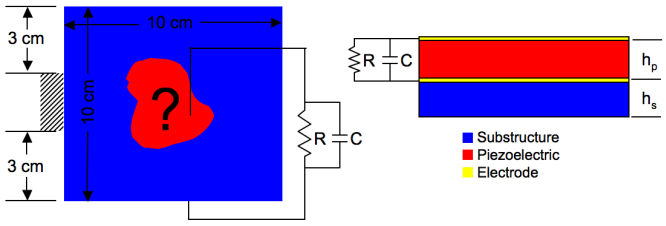

Figure 6.7: Design problem setup of a square plate subject to harmonic loading.

The resulting optimal material layouts are shown in Figure 6.8. As the thickness ratio increases the optimal design gradually changes. The designs optimized for the largest and smallest thickness ratios differ significantly. For a thin piezoelectric layer the material layout in the piezoelectric layer closely matches the signs of the strain distribution computed for a plate without piezoelectric layer (see Figure 6.8). With increasing thickness the material layout differs increasingly from this strain distribution as the piezoelectric layer adds stiffness and mass thereby changing the dynamic response of the structure. While the uniqueness of these designs cannot be guaranteed under our methodology, these problems were tested for local optima by solving them with a number of random initial designs, all of which converged to the same solution. These results suggest, but do not prove, that the optimization problem is globally convex.

The relationship between thickness ratio and optimal design is studied further by taking each piezoelectric pattern of Figure 6.8 (designs A-F), varying the piezoelectric thickness from $h_p/h_s = 0.001$ to 0.5, and computing the power generated in each case. These results are shown in Figure 6.9 where the output power for each design is normalized to the output power of the optimal design for that thickness ratio. For each thickness ratio the maximum power is produced by the design optimized for that thickness. This situation is not as intuitive as it might seem as evidenced by the non-monotonic behavior when moving away from the diagonal (which represents the family of optimal designs) in Figure 6.9, e.g., design D at $h_p/h_s = 0.5$ or design F at $h_p/h_s = 0.2$. The results also suggest an increasing sensitivity to design changes as thickness ratio

increases, for example in the noticeable drop in power output between designs F and E at $h_p/h_s = 0.5$. Although the two designs have somewhat similar features, the power output is significantly different because of the change in structural response caused by the additional thickness of the piezoelectric layer.

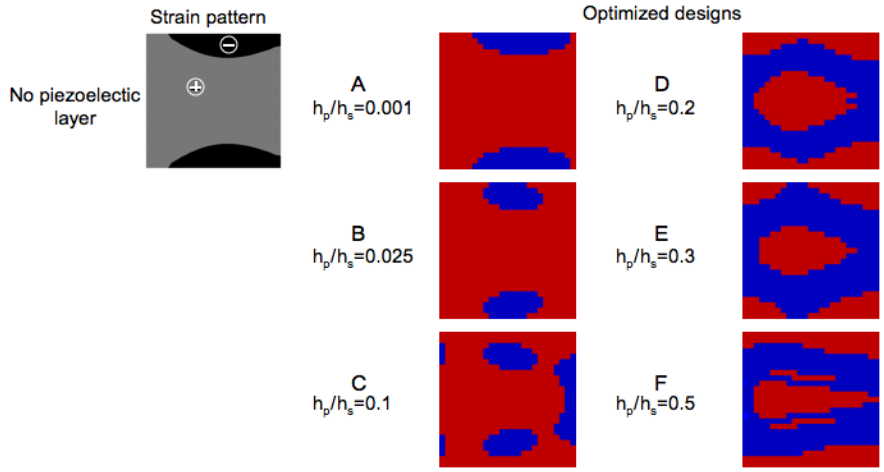

Figure 6.8: Comparison of the strain pattern for a plate without piezoelectric a layer with optimal distribution of piezoelectric material (red) on an aluminum substrate (blue) for six different ratios of piezoelectric to substrate thickness.

Figure 6.10 shows Frequency Response Functions (FRFs) of the output power encompassing the second through fourth modes for the fully covered and optimal plate designs for each of the thickness ratios. The FRFs for the fully covered plates show the general trend that an increase in thickness results in an increase in output power as well as a change in the response where the third mode shifts to lower frequencies. The driving frequency for this problem is consistently located between the second and third bending modes for these cases. For the optimal designs, the degree to which the FRF changes increases with thickness ratio. As the piezoelectric layer constitutes a larger fraction of the total structural makeup, the more its variation affects the overall structural response. For lower thickness ratios with less ability to change the structural response, the increase in output power is not caused by changes in the location of the natural frequencies, but the relative influence of the modes at the driving frequency.

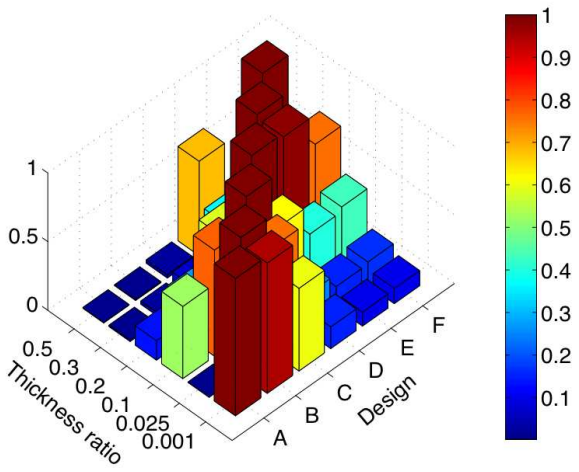

Figure 6.9: Power output for each design at each thickness ratio. The power magnitude of each thickness ratio is normalized to the power of the optimal design at that thickness ratio.

This is best seen for $h_p/h_s = 0.001$ and 0.025. As the thickness ratio increases, however, more freedom is allowed in the design to shift modes to different frequencies, specifically to move a mode toward the driving frequency such that the driving frequency becomes a resonant frequency. This is indicated in Figure 6.10 by the gradual shifting of the third mode to the driving frequency with increased thickness ratio, whereas more freedom to move the modes allows for the third mode to get closer to the driving frequency. As such, designs E and F of Figure 6.8 are structures with natural frequencies at the driving frequency of 575Hz and are akin to tuned cantilever beam harvesters typically used in energy harvesting applications, but without the need to change the shape or add an end mass.

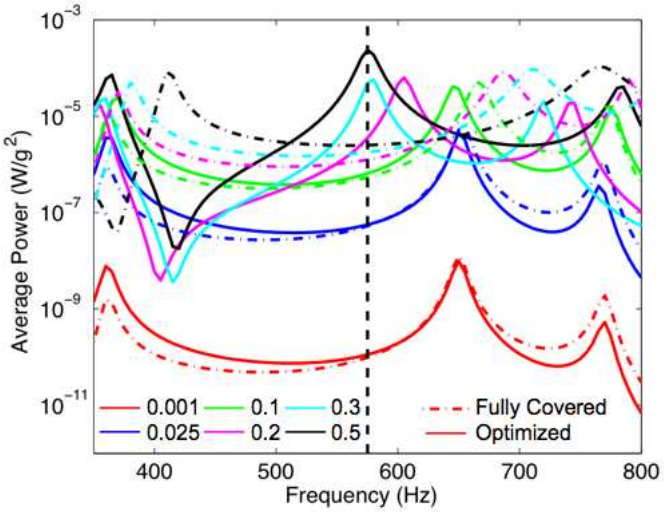

Figure 6.10: Power FRFs of both the fully covered (dots) and optimized designs (solid) for each of the thickness ratios. The vertical dashed line is the frequency at which the designs are optimized; it is located between the second and third modes for all of the fully covered plates.

In summary, these results show a strong influence of thickness ratio on the optimal layout of piezoelectric material on the plate. At larger thickness ratios the addition/removal of piezoelectric material significantly changes the mass and stiffness properties of the structure. The resulting material redistribution changes the structural modes in such a way that the structure simultaneously becomes "tuned" to the driving frequency and prevents charge cancellation, but only if the piezoelectric material constitutes a significant proportion of the structure. Not only do these results demonstrate the need to treat the coupled piezoelectric layer as an integral part of the system and its structural response when considering the design of piezoelectric energy harvesters, they also demonstrate the manner in which topology optimization can overcome the limitations of other existing design methods to improve the power output of such devices.

Simultaneous piezoharvester and circuit design

Here the same edge-clamped square plate as in the previous example is consid-

ered with the exception that the external circuit resistance is treated as a design variable along with the piezoelectric properties of the structure. In the previous example the electrical characteristics of the circuit were kept constant including the electrical capacitance of the system. As explained earlier, this is because the dielectric permittivity of the piezoelectric is not varied with its other properties, allowing for separation of the structural/material layout and electrical parts of the optimization problem. In this problem, the plate again is optimized for the six different thickness ratios with the same harmonic excitation of 575Hz. The optimization problem is started from an initial design with a fully covered piezoelectric layer. The material layout is kept variable along with the resistor to allow for simultaneous structure and circuit design.

The material distributions convergence to same layouts as obtained previously for a fixed resistivity of $1.0k\Omega$ and shown in Figure 6.8. Figure 6.11 shows the power output of the final optimized material layouts as a function of circuit load resistance as well as the individual optimized values for those designs at $R = 1.0k\Omega$ and the optimal resistances. This figure reveals the RC circuit-like behavior of power output as a function of resistance and shows that the final harvesting circuit resistance obtained via optimization coincides with the maxima of those curves. These data are also listed in Table 6.3, which provides a comparison of power output for all the designs including plates fully covered with piezoelectric. The data show that, while for small thickness ratios the optimal piezoelectric layout contributes little to improving the power output, as the thickness ratio increases the layout becomes increasingly important. This is particularly evident in the $h_p/h_s = 0.5$ design where the power output is improved by over 75 times. Also noted are that the optimal resistances between the fully covered and optimal designs are different even though the system capacitance is the same. This indicates, along with the calculated data shown in Table 6.4, that the optimal resistance obtained by applying the optimal circuit condition for an RC circuit does not correspond well with the results from our optimization. This finding is in agreement with those

of Erturk and Inman [41] and shows that obtaining the optimal parameters for the harvesting circuit is equally important as finding the proper structural design to provide that power, and that this approach yields both.

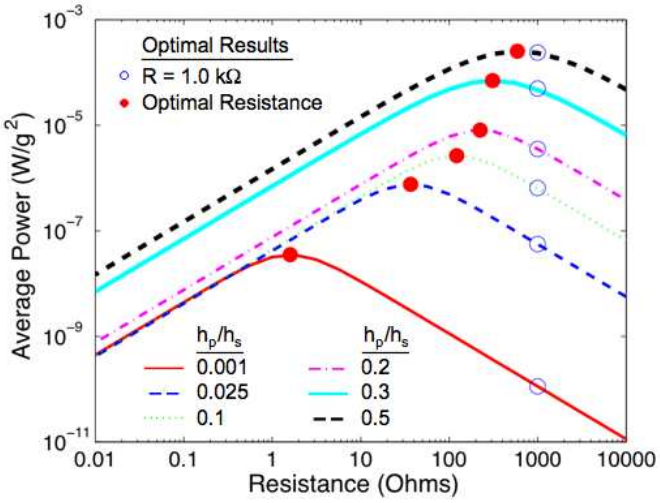

Figure 6.11: Power output as a function of resistance for all six thickness ratios including the optimal solutions obtained with R= 1kΩ (open circles) and with the resistance as an optimization variable as well (closed circles).

Table 6.3: Power output for various designs at a frequency of 575Hz

h_p/h_s	Fully covered with $R = 1.0k\Omega$ (Watts/g^2)	Fully covered with variable R (Watts/g^2)	Fully covered optimal resistance (Ω)	Optimized design with $R = 1.0k\Omega$ (Watts/g^2)	Optimized design with variable R (Watts/g^2)	Optimized design optimal resistance R (Ω)
0.001	9.83e-11	3.08e-8	1.59	1.13e-10	3.54e-8	1.60
0.025	5.29e-8	7.34e-7	35.9	5.60e-8	7.62e-7	36.6
0.1	5.37e-7	2.36e-6	114	6.49e-7	2.65e-6	121
0.2	1.25e-6	3.25e-6	198	3.55e-6	8.09e-6	223
0.3	1.78e-6	3.39e-6	282	4.95e-5	7.02e-5	309
0.5	2.51e-6	3.28e-6	465	2.39e-4	2.52e-4	591

Table 6.4: Calculated and optimal circuit resistances

h_p/h_s	Calculated piezoelectric capacitance (F)	Calculated optimal resistance $R = 1/\omega C$ (Ω)	Fully covered optimal resistance (Ω)	Optimized design optimal resistance R (Ω)
0.001	1.27e-4	2.18	1.59	1.60
0.025	5.08e-6	54.5	35.9	36.6
0.1	1.27e-6	218	114	121
0.2	6.35e-7	435	198	223
0.3	4.23e-7	654	282	309
0.5	2.54e-7	1090	465	591

Optimization with a mass load

In applications of piezoelectric cantilever beam harvesters, it is commonplace to tune the first resonant frequency of the beam to the primary ambient frequency to which it is exposed, thereby maximizing the transferable energy. This can be accomplished by altering the length or width of the beam or adjusting material parameters, but in practice this is often most easily achieved by adding a mass to the tip of the beam, which is particularly useful for manufactured beams with material properties and dimensions that are unalterable. Here it is illustrated how topology optimization can be used not only to determine the layout of the piezoelectric material, but also to determine how to spatially distribute a layer of non-stiffening mass to maximize the power output. The problem setup is the same as that for the first example with $R = 1.0k\Omega$, a thickness ratio $h_p/h_s = 0.1$, and an excitation frequency of 575Hz, but with an extra mass layer of thickness 0.1mm on top as shown in Figure 6.12. The density of the mass layer is the same as that of the piezoelectric. There is no constraint on placement of the mass

layer so it is possible that extra mass can be placed where there is no piezoelectric to support it, although this has little effect on the system response. These results can be used to determine the placement of an array of lumped masses or of a high density/low stiffness layer to improve harvester performance. The formulation could also be easily modified to allow for placing larger mass lumps in specific locations, similar to what is done in practice, but this option is not studied here.

The optimal material layouts of both the piezoelectric and mass layer are shown in Figure 6.12. Interestingly, the optimal layout of the piezoelectric material bears no resemblance to the optimal designs without the mass layer (specifically design C in Figure 6.8). The power FRFs of this and design C of Figure 6.8 are shown in Figure 6.13. In both cases, for the optimum designs, the third mode is shifted toward the driving frequency. As was shown before, the optimal layout of the piezoelectric layer alone is not sufficient to move the third mode all the way to the driving frequency at this thickness ratio, but the addition of the mass layer provides enough design freedom to achieve this in the optimal design. Indeed the added mass layer actually gives more freedom than the optimal structure with this same thickness ratio (i.e. $h_p/h_s = 0.2$, Figure 6.8, design C) and mass. The power output for this design at $R = 1.0k\Omega$ is $P = 6.34e-5\,W/g^2$, which is greater than the output for a piezoelectric layer twice as thick as shown in Table 6.3. This indicates that, for this example at least, optimizing an added mass layer in addition to the piezoelectric layer is more effective than increasing the thickness of a single piezoelectric layer and optimizing. One of the primary reasons for this is that the piezoelectric layer and mass layer can vary independently, which is not possible for the thicker piezoelectric layer and that the mass layer increases the inertia without adding stiffness. However, if stiffness were included with the mass layer, these results would likely be significantly different.

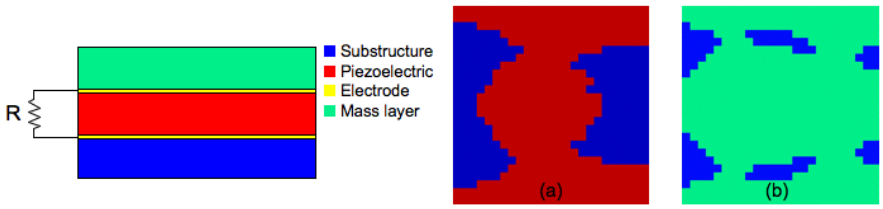

Figure 6.12: Through-thickness setup for a problem with a mass layer is the same as the flat plate problem but with a to-be-optimized layer of non-stiffening mass on the top. Optimal distribution of material in the (a) piezoelectric layer (red) and (b) mass layer (green).

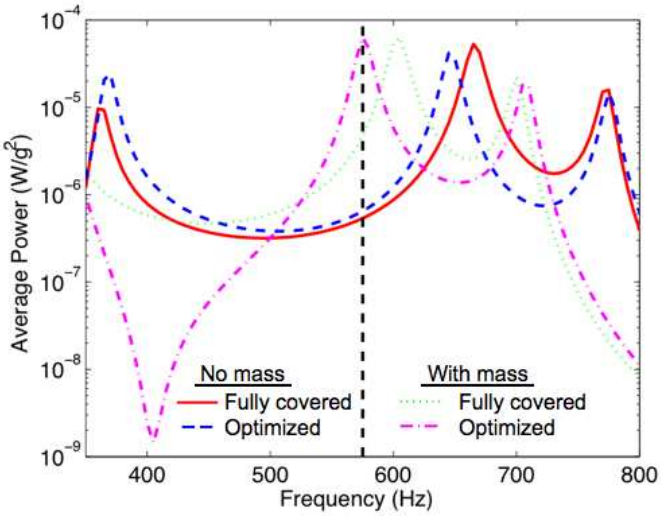

Figure 6.13: Power FRFs for fully covered and optimized designs with and without the added mass layer. The optimal design without the mass layer is design C of the previous examples.

Clamped curved plate

To further illustrate the versatility of the presented methodology, a series of structures with increasingly curved shapes are used as a substrate upon which a piezoelectric layer is deposited for energy harvesting. Curved devices may be required to accommodate design or configuration constraints. Alternatively, shape imperfections that occur

during fabrication or service may lead to curved shapes.

The base structure for this example is the same as the previous problems with a piezoelectric layer to substrate thickness ratio of $h_p/h_s = 0.1$, but the curvature of the base structure is varied as $\kappa L/\pi = [0, 0.02, 0.04, 0.1, 0.2, 0.4, 0.6, 0.8, 1.0]$ while the surface area is constant. The structure is clamped and vibrated as before and as shown in Figure 6.14. The optimal distribution of piezoelectric material located on the top of the plate (the inside of the curve) is sought that maximizes the harvested power through a $1.0k\Omega$ resistor for an excitation frequency of 575Hz, which is somewhere between the second and third bending modes for all curved structures. Figure 6.14 shows the optimized designs for a flat substrate and for two cases of curved substrates. The projections of the curved material layouts onto a flat plate for all curvatures considered are shown in Figure 6.15.

Figure 6.15 shows that the design changes with increasing base curvature. Some interesting trends are noted, such as the stark change in design with only a slight curvature added to the plate, which is due to the additional geometric stiffness and changes in mode shapes. The significant change in design as a function of base curvature implies that the optimal flat plate design is not efficient for energy harvesting on a slightly curved substrate and vice-versa. This is verified by the bar plot in Figure 6.16, which shows the power output for a given piezoelectric material layout for each structural curvature normalized by the power output of the optimal design for that base curvature, similar to that in Figure 6.9. The bar plot is diagonally dominant, meaning that each optimal design works best for the base curvature it is designed for, and reveals that the slightly curved design B will produce relatively little power on any base structure it was not designed for and vice versa. In contrast, curvatures at and above $\kappa L/\pi = 0.1$, which all have similar optimal material layouts as shown in Figure 6.15, produce similar amounts of power. As was the case of the flat plate in the first example, these results are related to the locations of the natural frequencies of

the structures relative to the excitation frequency. Figure 6.17 shows the relationship between the natural frequencies of the fully covered and optimal designs as a function of curvature. For the smaller base curvatures, large changes in natural frequency occur as a function of base curvature, while at the same time modes three and four nearly coincide. For larger base curvatures, however, the changes in natural frequency are less pronounced and the modes distinct. This correlates well with our earlier observation that differences in natural frequency and mode shape relative to the excitation frequency are significant drivers in the optimization process.

These results have general implications for manufacturing or handling of such structures due to the sensitivity of designs to small shape imperfections. For example, accidental bending or manufacturing flaws may have significant consequences in the performance of the piezoelectric harvesting system with small base curvature, but those with high base curvature would be more robust to such imperfections.

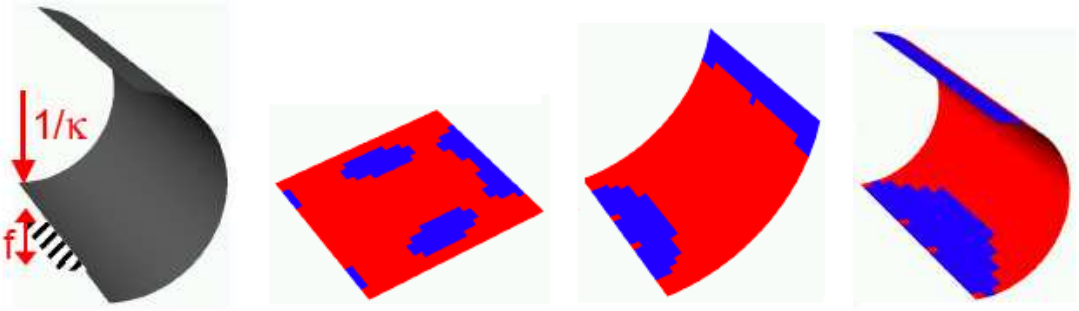

(a) (b) (c) (d)

Figure 6.14: (a) Problem setup and final material layouts of piezoelectric material ($h_p/h_s = 0.1$) on a curved substrate for a few different curvatures: (b) $\kappa L/\pi = 0$, (b) $\kappa L/\pi = 0.4$, (b) $\kappa L/\pi = 1.0$ (red – presence of piezoelectric material, blue – absence of piezoelectric material).

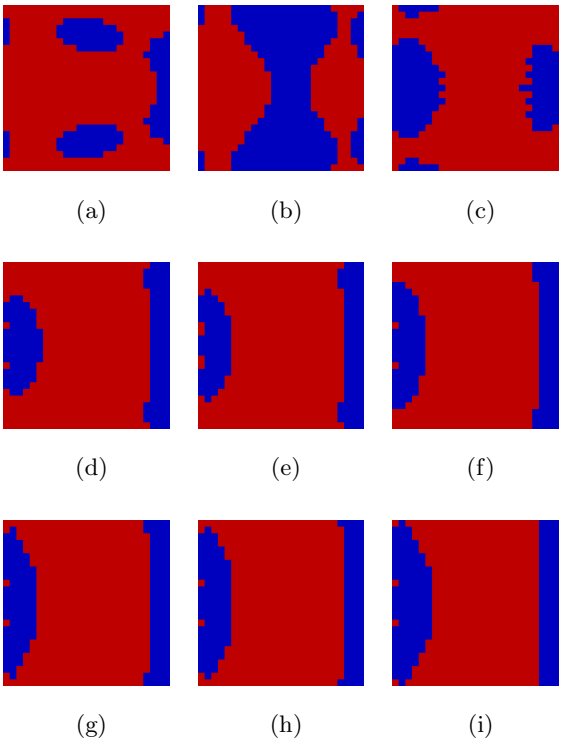

Figure 6.15: Optimal material layouts for curvatures ranging from a flat plate ($\kappa L/\pi$=0) to a half cylinder ($\kappa L/\pi$=1). (a)-(i) Final material layouts for curvatures $\kappa L/\pi$=[0,0.02,0.04,0.1,0.2,0.4,0.6,0.8,1.0] (red – presence of piezoelectric material, blue – its absence).

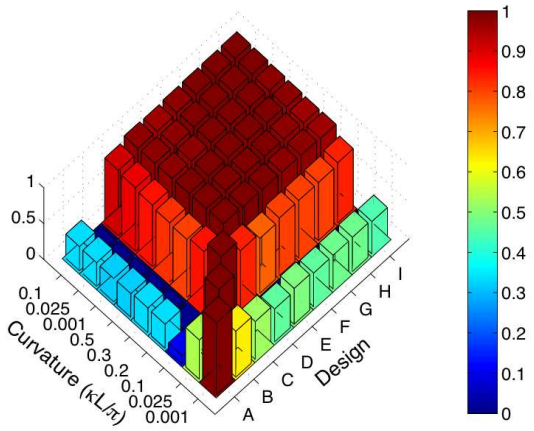

Figure 6.16: Power output for a given material layout and curvature normalized to the power outputs for the optimal design of the curvature.

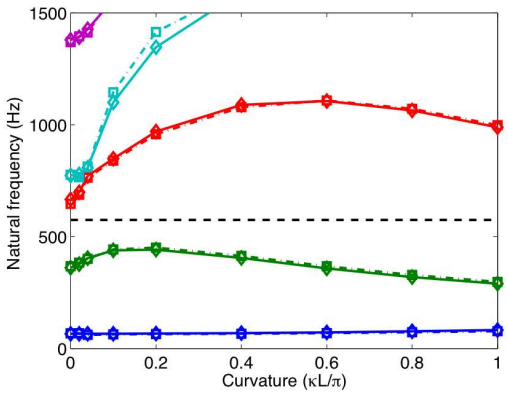

Figure 6.17: Natural frequencies of bending eigenmodes for structures fully covered with piezoelectric (solid with diamonds) and those of optimized designs (dash-dot with squares). The driving frequency (dashed line - 575Hz) is consistently between modes for all curvature values (solid bold line) with each mode a different color for comparison.

6.4.3 Piezoelectric waveguide and band-gap structure examples

Presented here are topology optimization problems and solutions for piezoelectric acoustic waveguides and a band-gap structure whose properties can be switched on and

off. The propagation of in-plane acoustic waves is considered, which travel through a 3-1 oriented piezoelectric slab covered by two electrodes on top and bottom as depicted in Fig. 1 for a bending waveguide setup. In this structure, the wave is traveling only through piezoelectric material, albeit with local differences in poling (either positive or negative). This situation disables the traditional means for waveguiding as there is effectively only a single elastic material and no material interfaces with which to interact, hence no reflection, transmission, or Bragg grating effects can occur. In fact, in a closed circuit situation where the top and bottom electrodes are connected, the piezoelectric effect is completely nullified and the structure will appear as an homogeneous medium to an acoustic incoming wave. In an open circuit situation, however, the wave will produce a voltage across the electrodes as the piezoelectric acts in a sensing mode. The electrodes, which cover the whole structure, will in turn simultaneously create an electric field everywhere else in the structure, thereby producing new acoustic waves in an actuation mode. Thus, the waveguiding and band-gap properties of these structures can be turned on and off by changing from open to closed circuit operation.

In these problems the piezoelectric material (PZT-5H) is modeled by the shell element described in section 6.2.2. The elements have a thickness of 1m (arbitrary; used for illustration purposes) and rotational and out-of-plate degrees of freedom are prescribed as zero, which approximates the plane stress condition. Electrodes surround the piezoelectric on the top and bottom out-of-plane surfaces in the shell element formulation with the bottom electrode grounded. The top surface of the piezoelectric thus has a constant voltage across the whole domain and all piezoelectric elements are hence directly coupled to each other, a much stronger coupling than the non-piezoelectric case. Design variables are tied to the piezoelectric coupling constant only, which varies linearly from a negative to a positive value, which corresponds to reversing the polarization. The goal is thus to determine the optimal layout of piezoelectric poling to maximize the objective. A penalization scheme was introduced after 200 iterations to help the design variables

converge to a "0-1" solution, although the designs were already close to converged and the objective did not change much.

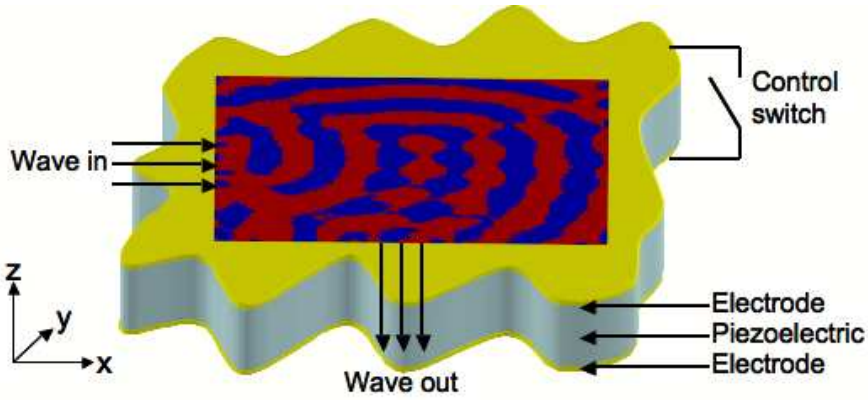

Figure 6.18: Schematic of a piezoelectric bending waveguide.

Piezoelectric bending waveguide

A bending waveguide composed of piezoelectric material is considered. The 1 cm x1 cm domain is meshed into a 100x100 grid surrounded by viscous damping non-reflecting boundary conditions. The input wave is excited at 2.0MHz at a 2 mm port in the middle of the left side of the domain. The objective function is formulated to maximize the vertical and minimize the horizontal displacement norms at the exit location, a 2 mm port in the middle of the bottom surface. The optimization is performed in an open circuit state.

The results of this example are shown in Figure 6.19. Similar to the non-piezoelectric bending waveguide, the complex norm wavefields of the homogeneous and final designs show that the wave enters the domain and exits as expected. The manner in which this occurs, however, is quite different as evidenced by the real part of the complex wavefields in the x- and y-directions. In the non-piezoelectric case the x-directional wavefields are very different from that in the homogeneous material whereas indicating that the wave energy is being guided toward the exit port. The same wavefield for

the piezoelectric case on the other hand is perturbed relatively little by the final distribution of piezoelectric material, although the field in the y-direction is significantly changed. This indicates that the device is working simultaneously as a sensor and actuator, whereby the incoming wave is "sensed" and its energy converted into an electric field that covers the whole domain, which is then used to directly actuate a separate wave in the y-direction. In fact, it is not possible to bend the wave by mechanical means using this setup because there is no impedance mismatch between the positively and negatively polarizations of the piezoelectric material. The efficiency of this device is calculated at 30%, based on the integrating the Poynting vector over the input and output ports. The low efficiency can be rationalized by the fact that the entire domain is covered in electrode and so any actuation occurs everywhere at once, even at the edges of the design domain where half of the actuated wave energy will enter the domain and the other half will immediately exit through the viscous damping boundary conditions. It is expected that the efficiency would increase and other functions could be created if a third, non-piezoelectric material with a different acoustic impedance were used for design in addition to finding the piezoelectric poling distribution. The significant aspect of this current design, however, is that the bending properties can be completely turned on and off.

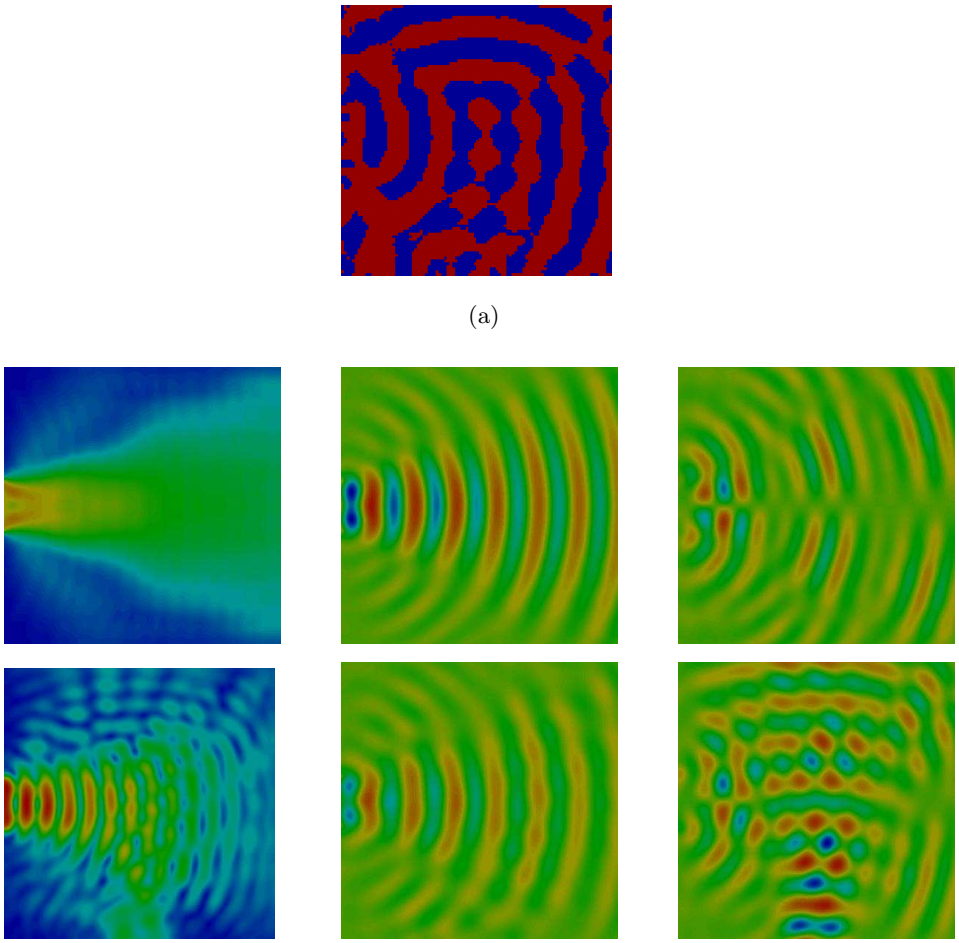

(a)

(b) (c) (d)

Figure 6.19: (a) Final layout of positive (blue) and negative (red) polarized piezoelectric. Wavefields in (top) a homogeneous material and (bottom) the final design for the (b) complex norm, (c) real x-direction, and (d) real y-direction.

Piezoelectric wave sensor and actuator

Here, two devices with complementary functions are designed: a device that converts elastic wave energy into electric field energy and another that does the opposite. In creating these devices, two separate domains are considered with the same properties as in the previous piezoelectric bending waveguide problem. The electrodes of each domain are connected with a wire so that they are electrically coupled, but not mechanically coupled. In the first domain an elastic wave enters the domain on the left

side while the objective function for the problem is formulated to maximize the complex norm displacements in the middle of the bottom side in the second domain in the same manner as the piezoelectric bending waveguide. As such, this setup essentially mimics the bending waveguide but through separation of the sensing and actuation functions. The final layouts of piezoelectric poling in the two domains are shown in Figure 6.20 as well as the complex norm displacement fields and pointing vector magnitudes. As the wave enters the first domain, the wave harmonically strains the piezoelectric creating an electric field whose energy is split between the first and second domains through the connection of their electrodes. This harmonic electric field then causes a strain in the second domain such that the resulting wave energy is focused toward the bottom of the domain. The plots of Poynting vector magnitude show a clear picture of sensing and actuation functions for these two devices.

The efficiency of this combination of sensor and actuator is 29% in transferring energy from the input port of the sensor to the exit port of the actuator. These designs also suffer from the setbacks described for the piezoelectric bending waveguide, and more so when combined due to the increased edges where wave energy can escape. As was the case previously, creating a closed circuit in the sensor design would cause the wave to pass through the sensor unimpeded, while no energy would be transferred to the actuator. The primary advantage of these designs is that they can be used separately whereas the sensor can be used as an energy harvester whose gathered energy could be used to power other devices, and the actuator could be powered by some other external source.

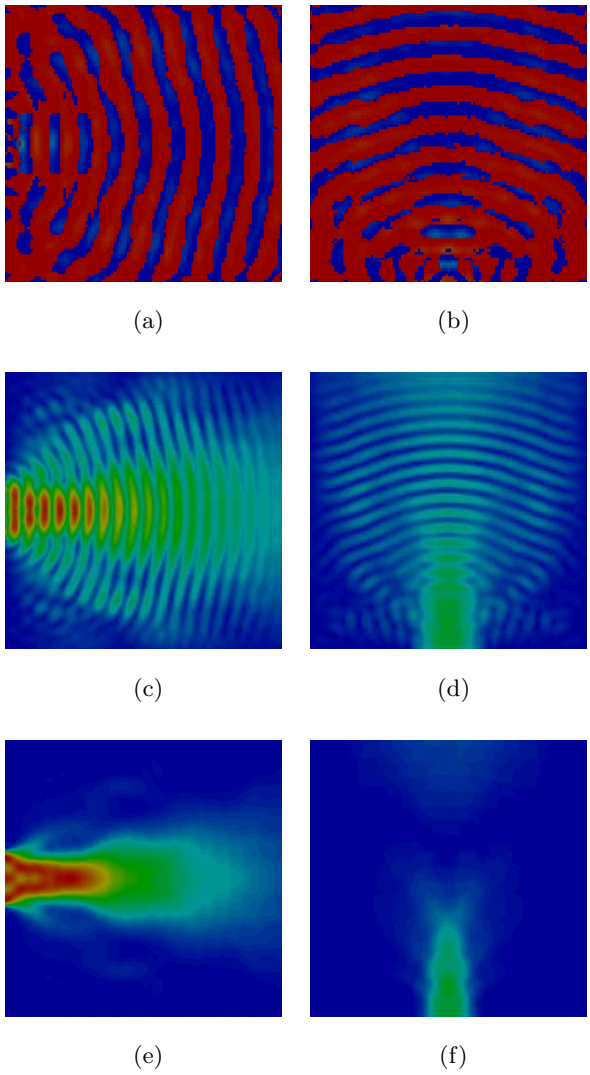

Figure 6.20: Final layout of piezoelectric polarization for the wave (a) sensor and (b) actuator with corresponding (c-d) displacement norm and (e-f) Poynting vector magnitude.

Piezoelectric Bragg grating

While a classical Bragg grating consists of alternating layers of two materials with different acoustic impedances, in the following design of a piezoelectric Bragg grating no impedance mismatch exists and therefore it is not clear how such a device should be designed. The goal of the problem is to find the distribution of piezoelectric poling that

creates the same effect as a Bragg grating. To facilitate this, a 5cm x 1cm rectangular domain is considered, similar to the Bragg grating verification problem in section 5.3. The computational domain is surrounded by periodic boundary conditions on top and bottom and viscous damping boundary conditions on the left and right. The domain is discretized into a mesh of 250 x 50 elements. A harmonic load at 500 MHz on the left side introduces a pressure wave into the domain. The objective function is to minimize the magnitude of the complex displacement norms on the right side of the domain.

The final distribution of piezoelectric poling is shown in Figure 6.21 along with the complex displacement norm field in both open circuit and closed circuit operation. Clearly the open circuit state blocks the wave while the closed circuit state lets the wave pass through uninhibited. This is verified in Figure 6.22, which shows the transmission of the wave as a function of frequency for both cases. While the final solution looks and acts like a classical Bragg grating, it is not actually a Bragg grating because Bragg reflections do not exist in the problem for lack of any impedance mismatch. Rather, the simultaneous sensing and actuation produces destructive interference of the wave. Regardless, the primary advantage of this design is that by merely changing from an open to closed circuit configuration the filtering properties of this structure can be completely turned off.

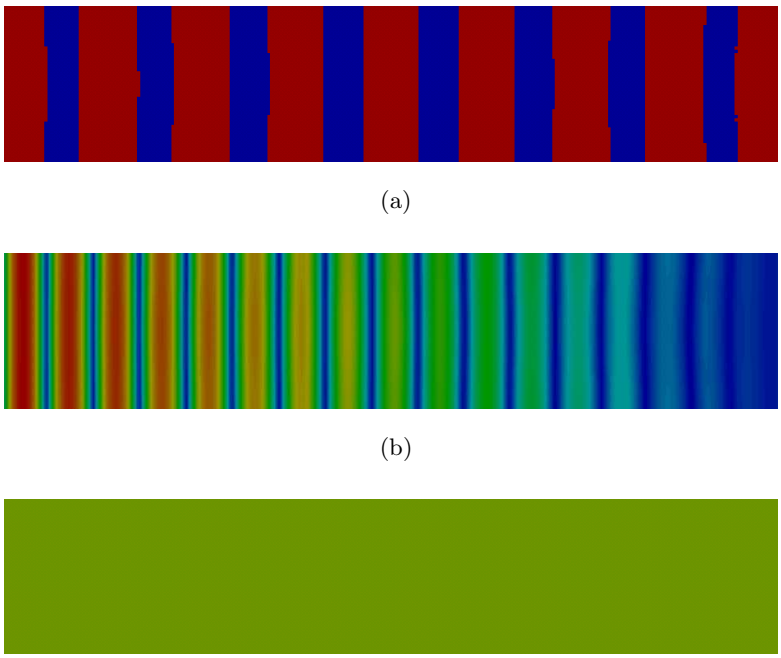

(a)

(b)

(c)

Figure 6.21: (a) Final layout of piezoelectric polarization (red – positive polarization, blue – negative polarization). Complex displacement norm field of the pressure wave propagating through the final structure in (b) open circuit and (c) closed circuit configurations.

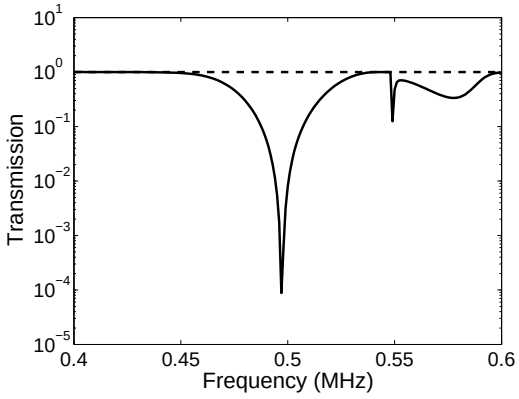

(a)

Figure 6.22: Wave transmission through the piezoelectric Bragg grating as a function of frequency for open circuit (solid) and closed circuit (dashed) configurations.

6.5 Summary

In this chapter a general methodology for the analysis and design of piezoelectric structures made from layered piezoelectric plates and their associated electrical circuits using topology optimization is presented. Using this approach it is possible to determine the material layout of structural, piezoelectric, and electrode components, along with circuit parameters to maximize the energy harvesting performance of piezoelectric harvesting systems and to synthesize piezoelectric waveguides and band-gap structures. The energy harvester example problems demonstrate the advantages, and in many cases the necessity, of such a design approach due to either the lack of an analytical theory to fully describe the structure or the large changes in response that the introduction of a piezoelectric layer may produce. In particular, it is found that a design methodology solely based on finding regions of positive and negative strain is inadequate for design purposes when the piezoelectric significantly changes the structural response. It is also found that it is possible for the sensitivity of a harvester's performance to shape imperfections to change significantly as a function curvature, an important result when considering design robustness. These results demonstrate that this methodology can be easily used to yield detailed designs for particular problems with application-specific objectives and constraints. For piezoelectric waveguide and band-gap structures, an important capability was demonstrated, namely the ability to design structures whose properties can be completely turned on or off depending on a simple open or closed circuit configuration. This is an ability for which there is currently no alternative method of design, making topology optimization with piezoelectric materials a particularly important tool for these novel problems.

Chapter 7

Conclusions and Future Work

7.1 Conclusions

The goal of the research presented in this dissertation was to develop and expand design methodologies using topology optimization for the generation of heterogeneous materials and structures subject to wave propagation, vibration, and piezoelectric phenomena. The phenomena at play in these systems include the various modes of wave propagation, how these modes interact with material interfaces and periodic arrays of material interfaces, the conversion of one mode into another, the electromechanical coupling of piezoelectric materials and how that affects wave propagation and vibrations, and the charge cancellation effects of electrodes piezoelectric structures. The effects of these phenomena and how they influenced the topology optimization design process were demonstrated in a number of examples and studies. In each of chapters 4, 5, and 6, key results were discussed. These are summarized here.

In chapter 4, topology optimization of elastic waveguides was investigated. It was found that the material layouts resulted in Bragg grating like structures, whether curved for the bending waveguide or shaped like a series of parabolic mirrors for the surface wave focuser. Investigations of the bending waveguide for high density meshes, however, revealed small, distinct features much smaller than the wavelength in the material, indicating that a phenomenon in addition to Bragg reflections was influencing the design. It was suggested that these features created a localized area of effective material

anisotropy as seen by the wave. In essence the optimizer is creating anisotropy in the design to improve the objective, although the individual materials used are isotropic. It was also shown, however, that the removal of these small features had little impact on the overall efficiency of the designs. Mode conversions were also a prominent phenomenon in these designs, in particular in the pressure to shear wave mode converter problem. An issue of symmetric optimization landscapes was also illustrated, revealing the definite possibility of local optima even though most waveguide problems have shown little dependence on initial design.

The work of chapter 5 illustrated the similarities and differences between two methodologies for the design of band-gap materials, namely band-gap structures and band-gap materials. The examples showed the significant effects that non-bulk propagating modes had on the material layout of the final designs using either methodology. Each methodology was also found to have its own drawbacks. Design of band-gap structures using time-harmonic analysis lacked the ability to isolate specific modes and as a result mode conversions would occur during analysis that would not be present in a true band-gap material. The Bloch-Floquet analysis and design methodology for band-gap materials, on the other hand, suffered from an inability to solve surface wave problems. It was also shown that the optimization landscape was full of local optima, where three different solutions were shown for three different initial designs. The redeeming quality of this methodology, however, is in the ability to directly manipulate the dispersion relation for the material. This was particularly illustrated with an example of a mode filtering material.

In the final chapter of methodologies and examples, chapter 6, piezoelectric structures were considered. The bulk of this chapter focused on the development of a new methodology for the design of piezoelectric energy harvesting structures. Through the examples it was shown that topology optimization is a necessary tool to find the optimal layout of piezoelectric material on the energy harvester because of the non-trivial

nature of the problem. This was evidenced by the balancing act that must be played between changing a structural mode and preventing charge cancellation. It was shown that optimization of the harvesting circuit is also of vital importance and that topology optimization of such structures can be a useful tool for design robustness. In addition to energy harvesters, piezoelectric materials in waveguides and band-gap structures were also investigated. This yielded new, novel designs using spatially distributed piezoelectric polarization for these types of devices with the ability to turn their waveguiding and band-gap properties on or off by merely changing from an open to a closed circuit configuration.

7.2 Future Work

The following projects constitute a set of largely unsolved problems in the areas of wave propagation, phononic materials, and vibrating piezoelectric energy harvesting systems. Outlined are descriptions of future work using topology optimization and the techniques discussed in this dissertation that may provide solutions to these problems. This work focuses on two problems: acoustic and elastic cloaking, including the cloaking structure and specialized meta-materials that may be used in such a structure, and the design of piezoelectric energy harvesting systems with nonlinear circuits.

7.2.1 Acoustic and elastic cloaking

The work described in this section focuses on the so-called cloaking problem. The cloaking problem, in which an object of finite size is hidden from external detection, has gained substantial attention over the past few years, especially in electromagnetics. Pendry et al. [126] has provided an analytical solution to the electromagnetic cloaking problem in three dimensions that uses a coordinate transformation of a sphere resulting in a spherical annulus constructed of exotic materials with negative permittivity and permeability. Milton et al. [114] subsequently analyzed how the form of the electromag-

netic and elastodynamic equations change under such coordinate transformations, and showed that they are invariant under such transformations. Cummer and Schurig [32] use a transformation of Maxwell's equations in applying Pendry's solution to acoustics which resulted in similar results that also use exotic properties including anisotropic density and bulk modulus materials, but is only applicable in two dimensions. Cai and Sanchez-Dehesa [18] have since analyzed Cummer and Schurig's two-dimensional solution and found that their acoustic cloak is less that perfect under more flexible situations such as when the cloaked region is not rigid. Recently, analytical solutions for acoustic waves in three dimensions have been provided independently by Chen and Chan [23] and Cummer et al. [31]. Chen and Chan apply Pendry's solution to a mapping and equivalence of the acoustic equation to the DC conductivity equation, while Cummer et al. arrived at the same solution through acoustic scattering theory, which is coincidentally used by Chen and Chan to verify their own solution. It should be noted, however, that these acoustic and the 2D electromagnetic (specifically not including the 3D electromagnetic case) solutions to the cloaking problem have singularities at the interior edge of the cloak, thereby introducing an inherent infeasibility in their solutions. In addition to this singularity, which can be mitigated by allowing for a less than perfect cloak, the cloaking formulations using Pendry's coordinate transformation solution are extremely sensitive to parameter changes, in particular the inner radius of the cloak as shown by Ruan et al. [134], primarily due to this singularity. Also, as noted by Chen et al. [24], the same types of solutions are valid only for a single frequency and scattering will dramatically increase away from that frequency. Chen et al. [24] rectify this problem in two-dimensional electromagnetic cloaks by mapping an annulus with a small scattering cross section to a larger annulus, rather than mapping a circle to an annulus. They showed that, as a result, the bandwidth of the cloak can be expanded, but at the expense of the scattering cross section and subsequent cloaking ability.

Aside from the issues of the cloaking structure, the major drawback of these solu-

tions is that they require the use of materials with properties such as anisotropic mass and stiffness, which are not found naturally in bulk materials. These authors claim, however, that advances in the design of meta-materials allows for the creation of new materials that exhibit the necessary properties. Meta-materials with such exotic properties have been described in a large number of studies for acoustics and elastodynamics [23, 33, 48, 63, 112, 115, 155]. The caveat, however, is that the dispersion that creates the exotic properties in meta-materials is generally able to perform as intended only within a small range of frequencies. This characteristic alone imposes severe limits on the bandwidth of any cloaking design. In other words, a cloak can be created (as shown by Schurig et al. [136] for electrodynamics in the microwave region), but will only be effective within the range of frequencies that the meta-materials hold their properties.

These limitations present two areas of research for which topology optimization is particularly suited; specifically the creation of different cloaking designs that operate in a finite frequency range (as admitted by Chen et al. [24] that other designs can exist) and the design of meta-materials that exhibit the properties required by those designs. Thus, three problems are proposed that use topology optimization: design of a cloaking structure with real materials, design of meta-materials with exotic properties, and design of a cloaking structure with exotic meta-materials.

Design of a cloaking structure with real materials

While nearly all of the work in the area of cloaking involves the use of exotic meta-materials one exception exists where Huang et al. [79] create an electromagnetic cloak in which they approximate the anisotropic behavior with a layered structure of homogeneous materials. For the acoustic or elastic cloaking problem, however, no work has been performed to show that a natural material is able or unable to provide some degree of acoustic cloaking ability. It has already been shown in this document that heterogeneous material designs created through topology optimization are capable of guiding wave energy from one location to another. It is therefore possible that a cloaking

structure could be created via the same principles in that the wave energy is guided around the cloaked region via waveguides. The goal of this project would be to determine in part the extent and conditions under which cloaking is possible with natural materials. The setup for this problem can be seen in Figure 7.1. A number of variations of this problem exist. Some possibilities include: changing the type of wave incident on the scatterer (e.g. P-wave, SH-wave, or SV-wave), different types of scatterers (e.g. rigid, non-rigid, void, arbitrary composition, etc.), ensuring cloaking for multiple angles of incidence (some solutions may have a direction bias), cloaking for multiple frequencies or a range of frequencies.

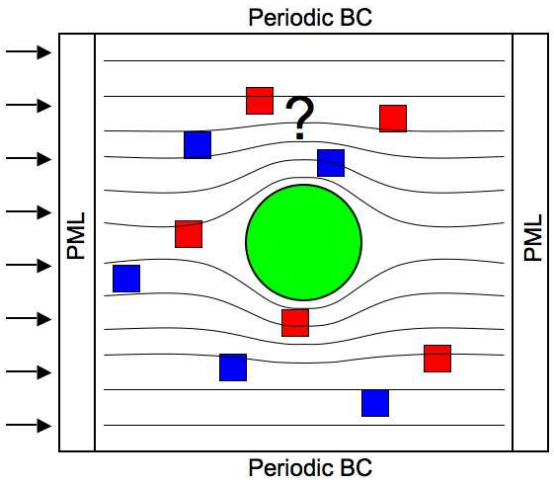

Figure 7.1: Problem setup for the cloaking problem with real material properties. A wave enters from the left into the domain which contains a circular scattering object of some material (green) different from the design materials (red and blue). The objective would minimize the difference in the value of the Poynting vector at the right edge with the same from a case without the scattering object.

Design of meta-materials with properties needed for cloaking

General work in the area of meta-materials started in the field of photonics where there the split-ring resonator has become a well-known implementation as well as an

easily explainable and reasonably intuitive model (see the review article by Lapine and Tretyakov [99] for a recent snapshot of the state of photonic meta-materials). The ideas from those studies have slowly progressed into the field of phononics, but the have largely been hampered by the increased complexity of the governing equations. It is therefore a ripe area for research, particularly in the design of new meta-materials using topology optimization.

Studies that have designed and analyzed elastic and acoustic meta-materials generally intend to create materials with exotic properties such as negative effective density or stiffness. The concept of negative effective mass density has been nicely summarized by Milton and Willis [116] in a simple model of springs and masses embedded in a rigid bar, the concept of which is shown in Figure 7.2. The simple derivation of the equations of motion for such a system results in an expression for total momentum that is a function of frequency:

$$P = \left(M_0 + \frac{2Knm}{2K - m\omega^2} \right) V = MV \tag{7.1}$$

where P, V, and M are the externally seen momentum, velocity, and mass, respectively, M_0 is the rigid bar mass, K is the internal spring stiffness, m is the individual mass of the n internal masses, and ω is the frequency of the forcing function. While internally the dynamics are consistent, the external observer would measure a negative dynamic mass because the bar would accelerate backward with a forward push (in a dynamic sense). Milton and Willis [116] also extend their model to demonstrate the concept of anisotropic effective mass density, a key need of meta-materials for cloaking structures.

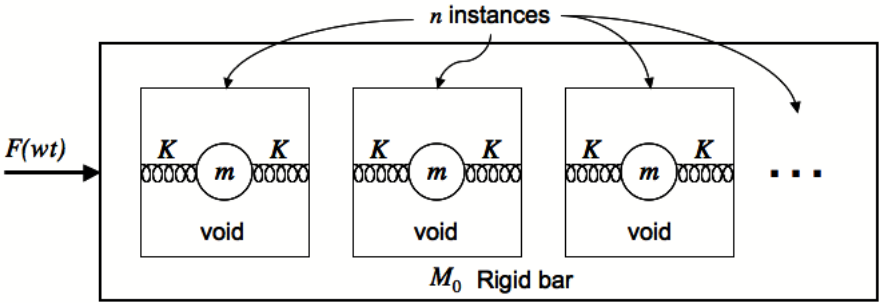

Figure 7.2: Schematic from Milton and Willis showing a "material" with a negative effective mass density.

Most studies of negative/anisotropic density and stiffness meta-materials concentrate on various arrangements of hard objects in a soft matrix or elastic and rigid solids in acoustic liquids [33, 112, 138, 155, 156]. Fang et al. [48], on the other hand use resonator cavities to produce a negative bulk modulus, while Geunneau et al. [63] demonstrate negative refraction using a specially structured meta-material that is designed to act like a spring-mass system. The authors of these papers base their designs directly on the idea of Helmholtz resonators, although the other studies can be represented in the same manner. The key idea is that when a number of Helmholtz resonators are combined in a periodic array, they can cause exotic and desirable dispersion characteristics in the properties of the whole, i.e. the meta-material, even for wavelengths much larger than the periodicity of the meta-material.

The goal of this project would be to create phononic meta-materials, specifically those with anisotropic density and stiffness as is required for the cloaking designs of Chen and Chan [23], Cummer and Schurig [32], and Cummer et al. [31]. Milton's studies on meta-materials [111, 113] provide a methodology for obtaining effective material properties from Bloch wave analysis that could be used to obtain and tailor phononic meta-materials. Doing this would likely require the development of new objective and constraint functions for use with topology optimization. These will likely include functions for the effective mass density and stiffness as well as multiple components of the

related effective mass and stiffness tensors. This project would not only demonstrate that such materials exist and can be designed, but also would provide a tool and methodology for that purpose.

Design of cloaking structures with meta-material properties

In the derivation of a finite bandwidth cloaking device, Chen et al. [24] openly state that their method, which is closely related to that of Pendry et al. [126], is not the only way to create a cloak with a finite bandwidth. As such, their basic assumptions may be the limiting factor in the performance of their device. By avoiding the regular coordinate transformation method used in all current publications on the subject and replacing it with the flexibility of topology optimization, it may be possible to improve upon the results and inherent drawbacks in designing a phononic cloak. The idea of this project is to investigate the capabilities of topology optimization in designing a cloaking structure using materials with exotic properties such as anisotropic/negative mass and stiffness like those provided by meta-materials. The problem setup will be similar to that of 7.1, but with the use of meta-materials. The same sets of problem variations would exist as well, but more focus could be spent on including various types of meta-material properties such as purely negative vs. anisotropic density and stiffness. Particular attention could be paid to materials that are successfully designed from other proposed work in this subsection.

7.2.2 Topology optimization of vibrating energy harvesting structures with nonlinear circuits

In chapter 5, vibrating piezoelectric energy harvesters were designed for harvesting circuits containing linear components only. The practicality of linear harvesting circuits is greatly limited by the fact that in nearly all energy harvesting situations the electrical energy must be transformed to be compatible with whatever device that energy is powering, a process that generally requires nonlinear circuit components such as

diodes in a rectifier. As such, the validity of the linear circuit analysis for the design of energy harvesters is questionable. This, however, should not negate the direct applicability of the methodology to create designs for mechanical damping through electrical shunting [67], control [118, 158, 163], or sensing/actuation [34, 35, 78].

Analysis of piezoelectric energy harvesters with nonlinear circuits has been performed by a number of groups [39, 97, 101, 102, 103, 96, 105, 104, 122, 123, 141, 140, 142, 139], but the methods used by these groups are incapable of incorporation with a finite element model and thus lack generality, high fidelity, and the ability to design the harvester using topology optimization. Appendix A details a methodology for analysis of piezoelectric energy harvesters with nonlinear circuits for which this is possible, wherein it is illustrated with examples some of the ways a linear harvesting circuit response differs from that of a nonlinear circuit. Due to the difference in harvesting system response between linear and nonlinear circuits it is highly likely that the optimal design for the linear circuit is no longer optimal for the nonlinear circuit. As such, a design methodology for piezoelectric energy harvesters with nonlinear circuits is needed. Using the methodology described in appendix A, which uses a series of time-harmonic finite element problems for its solution, it is possible to formulate an efficient topology optimization methodology that would otherwise require an intractable transient nonlinear analysis. Such a methodology would use a stationary point formulation common to other nonlinear topology optimization problems [124] and would allow for the design of piezoelectric harvesters that can take advantage of and account for the nonlinear effects not present in linear circuits.

Bibliography

[1] Mostafa Abdalla, Mary I. Frecker, Zafer Gurdal, Terrence Johnson, and Douglas K. Lindner. Design of a piezoelectric actuator and compliant mechanism combination for maximum energy efficiency. Smart Materials and Structures, 14:1421–1430, 2005.

[2] S. R. Anton and Henry A. Sodano. A review of power harvesting using piezoelectric materials (2003-2006). Smart Materials and Structures, 16:R1–R21, 2007.

[3] Bertram Alexander Auld. Acoustic fields and waves in solids. Krieger Publishing Co., Malabar, Florida, 2nd edition, 1973.

[4] Waldemar Axmann and Peter Kuchment. An efficient finite element method for computing spectra of photonic and acoustic band-gap materials. Journal of Computational Physics, 150:468–481, 1999.

[5] Ushnish Basu and Anil K. Chopra. Perfectly matched layers for time-harmonic elastodynamics of unbounded domains: theory and finite-element implementation. Computer Methods in Applied Mechanics and Engineering, 192:1337–1375, 2003.

[6] Klaus-Jürgen Bathe. Finite Element Procedures. Prentice Hall, Englewood Cliffs, 2007.

[7] S. P. Beeby, M. J. Tudor, and N. M. White. Energy harvesting vibration sources for microsystems applications. Measurement Science and Technology, 13:175–195, 2006.

[8] J. C. Bellido and A. Donoso. An optimal design problem in wave propagation. Journal of Optimization Theory and Applications, 134(2):339–352, 2007.

[9] T. Belytschko and R. Mullen. Modern problems in elastic wave propagation: International Union of Theoretical and Applied Mechanics symposium held at Northwestern University, Evanston, Illinois, USA, Septemeber 12-15, 1977, chapter On dispersive properties of finite element solutions. John Wiley, Chichester, 1978.

[10] Martin P. Bendsøe and Noboru Kikuchi. Generating optimal topologies in structural design using a homogenization method. Computer Methods in Applied Mechanics and Engineering, 71(2):197–224, 1988.

[11] Martin P. Bendsøe and Ole Sigmund. Topology Optimization: Theory, methods and applications. Springer, Berlin, 2003.

[12] Jean-Pierre Bérenger. A perfectly matched layer for the absorption of electromagnetic waves. Journal of Computational Physics, 114(2):185–200, 1994.

[13] F. Bloch. Uber die quantenmechanik der electron in kristallgittern. Zeifschrift für Physik, 52(555-600), 1928.

[14] P. I. Borel, A. Harpøth, L. H. Frandsen, M. Kristensen, P. Shi, J. S. Jensen, and O. Sigmund. Topology optimization and fabrication of photonic crystal structures. Optics Express, 12(9), 2004.

[15] C. A. Brebbia, J. C. F. Telles, and L. C. Wrobel. Boundary element techniques: Theory and applications in engineering. Springer, Berlin, 1984.

[16] L. M. Brekhovskikh. Waves in layered media. Academic Press, New York, 1980.

[17] Leon Brillouin. Wave propagation in periodic structures. Dover, New York, 2nd edition, 1953.

[18] Liang-Wu Cai and Jose Sanchez-Dehesa. Analysis of cummer-schurig acoustic cloaking. New Journal of Physics, 9(450), 2007.

[19] Ronny C. Carbonari, Emilio C. N. Silva, and Shinji Nishiwaki. Optimum placement of piezoelectric material in piezoactuator design. Smart Materials and Structures, 16:207–220, 2007.

[20] Ronny C. Carbonari, Emilio C. N. Silva, and Glaucio H. Paulino. Topology optimization design of functionally graded bimorph-type piezoelectric actuators. Smart Materials and Structures, 16:2605–2620, 2007.

[21] E. Centeno, B. Guizal, and D. Felbacq. Multiplexing and demultiplexing with photonic crystals. J. Opt. A.: Pure Appl. Opt., 1(5), 1999.

[22] J. David N. Cheeke. Fundamentals and applications of ultrasonic waves. CRC Press, 2002.

[23] Huanyang Chen and C. T. Chan. Acoustic cloaking in three dimensions using acoustic metamaterials. Applied Physics Letters, 91(183518), 2007.

[24] Huanyang Chen, Zixian Liang, Peigun Yao, Xunya Jiang, Hongru Ma, and C. T. Chan. Extending the bandwidth of electromagnetic cloaks. Physical Review B, 76(241104), 2007.

[25] W. C. Chew and W. H. Weedon. A 3d perfectly matched medium from modified maxwell's equations with stretched coordinates. Microwave and Optical Technology Letters, 7(13):599–604, 1994.

[26] Edmond Chow, S. Y. Lin, J. R. Wendt, S. G. Johnson, and John D. Joannopoulos. Quantitative analysis of bending efficiency in photonic-crystal waveguide bends at $\lambda = 1.55\mu$m wavelengths. Optics Letters, 26(5):286–288, 2001.

[27] Alongkarn Chutinan and Susumu Noda. Waveguides and waveguide bends in two-dimensional photonic crystal slabs. Physical Review B, 62(7):4488–4492, 2000.

[28] K. A. Cook-Chennault, N. Thambi, and A. M. Sastry. Powering mems portable devices - a review of non-regenerative and regenerative power supply systems with emphasis on piezoelectric energy harvesting systems. Smart Materials and Structures, 17(043001), 2008.

[29] Steven J. Cox and David C. Dobson. Maximizing band gaps in two-dimensional photonic crystals. SIAM Journal on Applied Mathematics, 59(6):2108–2120, 1999.

[30] Steven J. Cox and David C. Dobson. Band structure optimization of two-dimensional photonic crystals in h-polarization. Journal of Computational Physics, 158(2):214–224, 2000.

[31] Steven A. Cummer, Bogdan-Ioan Popa, David Schurig, David R. Smith, John Pendry, Marco Rahm, and Anthony Starr. Scattering theory derivation of a 3d acoustic cloaking shell. Physical Review Letters, 100(024301), 2008.

[32] Steven A. Cummer and David Schurig. One path to acoustic cloaking. New Journal of Physics, 9(45), 2007.

[33] Yiqun Ding, Zhengyou Liu, Chunyin Qiu, and Jing Shi. Metamaterial with simultaneously negative bulk modulus and mass density. Physical Review Letters, 99(093904), 2007.

[34] A. Donoso and J. C. Bellido. Systematic design of distributed piezoelectric modal sensors/actuators for rectangular plates by optimizing the polarization profile. Structural and Multidisciplinary Optimization, 38(4):347–356, 2009.

[35] A. Donoso and Ole Sigmund. Optimization of piezoelectric bimorph actuators with active damping for static and dynamic loads. Structural and Multidisciplinary Optimization, 38(2):171–183, 2009.

[36] Joachim Drenckhan, Arnold Lumsdaine, and Matthew Parsons. Topology optimization of a piezoelectric actuator on an elastic beam. Journal of Intelligent Material Systems and Structures, 19:445–455, 2008.

[37] N. E. duToit, B. L. Wardle, and S.-G. Kim. Design considerations for mems-scale piezoelectric mechanical vibration energy harvesters. Integrated Ferroelectrics, 71:121–160, 2005.

[38] A. Elka and I. Bucher. Optimal electrode shaping for precise modal electromechanical filtering. Structural and Multidisciplinary Optimization, 38(6):627–641, 2009.

[39] Niell G. Elvin and Alex A. Elvin. A general equivalent circuit model for piezoelectric generators. Journal of Intelligent Material Systems and Structures, 20(1):3–9, 2009.

[40] A. Erturk and Daniel J. Inman. A distributed parameter electromechanical model for cantilevered piezoelectric energy harvesters. Journal of Vibration and Acoustics, 130(041002), 2008.

[41] A. Erturk and Daniel J. Inman. Issues in mathematical modeling of piezoelectric energy harvesters. Smart Materials and Structures, 17(065016), 2008.

[42] A. Erturk and Daniel J. Inman. On mechanical modeling of cantilevered piezoelectric vibration energy harvesters. Journal of Intelligent Material Systems and Structures, 19(11):1311–1325, 2008.

[43] A. Erturk and Daniel J. Inman. Energy Harvesting Technologies, chapter Electromechanical modeling of cantilevered piezoelectric energy harvesters for persistent base motions, pages 41–77. Springer, 2009.

[44] A. Erturk and Daniel J. Inman. An experimentally validated bimorph cantilever model for piezoelectric energy harvesting from base excitations. Smart Materials and Structures, 18(025009):1–18, 2009.

[45] A. Erturk, P. A. Tarazaga, J. R. Farmer, and Daniel J. Inman. Effect of strain nodes and electrode configuration on piezoelectric energy harvesting from cantilever beams. Journal of Vibration and Acoustics, 131(011010):1–11, 2009.

[46] Alper Erturk, Jamil M. Renno, and Daniel J. Inman. Modeling of piezoelectric energy harvesting from an l-shaped beam-mass structures with an application to uavs. Journal of Intelligent Material Systems and Structures, 2009.

[47] Anton Evgrafov, Cory J. Rupp, Kurt Maute, and Martin L. Dunn. Large scale parallel topology optimization using dual-primal substructuring solver. Structural and Multidisciplinary Optimization, 2008.

[48] Nicholas Fang, Dongjuan Xi, Jianyi Xu, Muralidhar Ambati, Werayut Srituravanich, Cheng Sun, and Xiang Zhang. Ultrasonic metamaterials with negative modulus. Nature, 5:452–456, 2006.

[49] Charbel Farhat, Philip Avery, Radek Tezaur, and Jing Li. Feti-dph: A dual-primal domain decomposition method for acoustic scattering. Journal of Computational Acoustics, 13(3):499–524, 2005.

[50] G. W. Farnell and E. L. Adler. Properties of elastic surface waves. In Warren P. Mason and R. N. Thurston, editors, Physical Acoustics, volume 6, chapter 3, pages 109–166. Academic Press, 1970.

[51] Carlos A. Felippa. A study of optimal membrane triangles with drilling freedoms. Computer Methods in Applied Mechanics and Engineering, 192:2125–2168, 2003.

[52] G. Floquet. Sur les equations différentielles linéaries à coefficients périodiques. annales de l'Ecole Normale Supérieur, pages 47–88, 1883.

[53] L. H. Frandsen, A. Harpøth, P. I. Borel, M. Kristensen, J. S. Jensen, and O. Sigmund. Bradband photonic crystal waveguide 60 degree bend obtained utilizing topology optimization. Optics Express, 12(24):5916–5921, 2004.

[54] Mary I. Frecker. Recent advances in optimization of smart structures and actuators. Journal of Intelligent Material Systems and Structures, 14(4-5):207–216, 2003.

[55] W. R. Frei, D. A. Tortorelli, and H. T. Johnson. Topology optimization of a photonic crystal waveguide termination to maximize directional emission. Applied Physics Letters, 86(11), 2005.

[56] Moritz Frenzel. Topology optimization for wave problems. Master's thesis, University of Colorado at Boulder, 2004.

[57] George A. Gazonas, Daniel S. Weile, Raymond Wildman, and Anuraag Mohan. Genetic algorithm optimization of phononic bandgap structures. International Journal of Solids and Structures, 43:5851–5866, 2006.

[58] Thomas L. Geers and Brett A. Lewis. Double asymptotic approximations for transient elastodynamics. International Journal of Solids and Structures, 34(11):1293–1305, 1997.

[59] J. M. Gibert and E. M. Austin. Demonstration of optimizing piezoelectric polarization in the design of a flextensional actuator. Structural and Multidisciplinary Optimization, 33:471–480, 2007.

[60] Philip E. Gill, Walter Murray, and Michael A. Saunders. Snopt: An sqp algorithm for large-scale constrained optimization. SIAM Journal on Optimization, 12(4):979–1006, 2002.

[61] T. Gorishnyy, C. K. Ullal, M. Maldovan, G. Fytas, and E. L. Thomas. Hypersonic phononic crystals. Physical Review Letters, 94(115501), 2005.

[62] Karl F. Graff. Wave motion in elastic solids. Dover, New York, 1975.

[63] Sebastien Guenneau, Alexander Movchan, Gunnar Petursson, and S. Anantha Ramakrishna. Acoustic metamaterials for sound focusing and confinement. New Journal of Physics, 9(399), 2007.

[64] Yu. V. Gulyaev and V. P. Plesskii. Propagation of acoustic surface waves in periodic structures. Sov. Phys. Usp, 32(1):51–74, 1989.

[65] Daniel Guyomar, Adrien Badel, Elie Lefeuvre, and Claude Richard. Toward energy harvesting using active materials and conversion improvement by nonlinear processing. IEEE Transactions on Ultrasonics, Ferroelectrics, and Frequency Control, 52(4):584–595, 2005.

[66] Yoondo Ha and Seonho Cho. Design sensitivity analysis and topology optimization of eigenvalue problems for piezoelectric resonators. Smart Materials and Structures, 15:1513–1524, 2006.

[67] N. W. Hagood and A. von Flotow. Damping of structural vibrations with piezoelectric materials and passive electrical networks. Journal of Sound and Vibration, 146(2):243–268, 1991.

[68] Søren Halkjær, Ole Sigmund, and Jakob S. Jensen. Maximizing band gaps in plate structures. Struct. Multidisc. Optim., 32:263–275, 2006.

[69] Isaac Harari. A survey of finite element methods for time-harmonic acoustics. Computer Methods in Applied Mechanics and Engineering, 195:1594–1607, 2006.

[70] Isaac Harari and Uri Albocher. Studies of fe/pml for exterior problems of time-harmonic elastic waves. Computer Methods in Applied Mechanics and Engineering, 195:3854–3879, 2006.

[71] F. Hemez. The 3-node composite shell and isoparametric timoshenko beam elements. Technical Report CU-CAS-94-16, Center for Aerospace Structure, University of Colorado, 1994.

[72] Anne-Christine Hladky-Hennion and Jean-Noel Decarpigny. Analysis of the scattering of a plane acoustic wave by a double periodic structure using the finite element method: Application to alberich anechoic coatings. Journal of the Acoustical Society of America, 90(6):3356–3367, 1991.

[73] K. M. Ho, C. T. Chan, and C. M. Soukoulis. Existence of photonic gap in periodic delectric structures. Physical Review Letters, 65(25):3152–3155, 1990.

[74] Manfred Hofer, Norman Finger, Gunter Kovacs, Joachim Schoberl, Sabine Zaglmayr, Ulrich Langer, and Reinhard Lerch. Finite-element simulation of wave propagation in periodic piezoelectric saw structures. IEEE Transactions on Ultrasonics, Ferroelectrics, and Frequency Control, 53(6), 2006.

[75] Po-Feng Hsieh, Tsung-Tsong Wu, and Jia-Hong Sun. Three-dimensional phononic band gap calculations using the fdtd method and a pc cluster system. IEEE Transactions on Ultrasonics, Ferroelectrics, and Frequency Control, 53(1):148–158, 2006.

[76] Jin-Chen Hsu and Tsung-Tsong Wu. Lamb waves in binary locally resonant phononic plates with two-dimensional lattices. Applied Physics Letters, 90(201904), 2007.

[77] Jin-Chen Hsu and Tsung-Tsong Wu. Propagation of lamb waves in phononic-crystal plates. Journal of Mechanics, 23(3):223–228, 2007.

[78] Jin H. Huang, Jhao-Ming Chen, and Y. C. Shiah. Electromechanical analysis of a piezoelectric beam used to drive a torsional microactuator. Journal of Intelligent Material Systems and Structures, 18:543–553, 2007.

[79] Ying Huang, Yijun Feng, and Tian Jiang. Electromagnetic cloaking by layered structure of homogeneous isotropic materials. Optics Express, 15(18):11133–11141, 2007.

[80] Mahmoud I. Hussein, Karim Hamza, Gregory M. Hulbert, and Kazuhiro Saitou. Optimal synthesis of 2d phononic crystals for broadband frequency isolation. Waves in Random and Complex Media, 17(4):491–510, 2007.

[81] Mahmoud I. Hussein, Karim Hamza, Gregory M. Hulbert, Richard A. Scott, and Kazuhiro Saitou. Multiobjective evolutionary optimization of periodic layered materials for desired wave dispersion characteristics. Struct. Multidisc. Optim., 31(1):60–75, 2006.

[82] Mahmoud I. Hussein, Gregory M. Hulbert, and Richard A. Scott. Band-gap engineering of elastic waveguides using periodic materials. In IMECE, November 16-21, Washington, DC USA, number 41886. ASME, 2003.

[83] Mahmoud I. Hussein, Gregory M. Hulbert, and Richard A. Scott. Hierarchical design of phononic materials and structures. In IMECE, November 5-11, Orlando, Florida USA, number 81325. ASME, 2005.

[84] Jakob S. Jensen. Topology optimization problems for reflection and dissipation of elastic waves. Journal of Sound and Vibration, 301:319–340, 2007.

[85] Jakob S. Jensen and Ole Sigmund. Systematic design of photonic crystal structures using topology optimization: Low-loss waveguide bends. Applied Physics Letters, 84(12):2022–2024, 2004.

[86] Jakob S. Jensen and Ole Sigmund. Topology optimization of photonic crystal structures: a high-bandwidth low-loss t-junction waveguide. J. Opt. Soc. Am. B, 22(6):1191–1198, 2005.

[87] John D. Joannopoulos, Robert D. Meade, and Joshua N. Winn. Photonic crystals: Molding the flow of light. Princeton University Press, 1995.

[88] Hajime Kando, Daisuke Yamamoto, Hikari Tochishita, and Michio Kadota. Rf filter using boundary acoustic wave. Japanese Journal of Applied Physics, 45(5B):4651–4654, 2006.

[89] Zhan Kang and Liyong Tong. Integrated optimization of material layout and control voltage for piezoelectric laminated plates. Journal of Intelligent Material Systems and Structures, 19(8):889–904, 2008.

[90] Zhan Kang and Liyong Tong. Topology optimization-based distribution design of actuation voltage in static shape control of plates. Computers and Structures, 86:1885–1893, 2008.

[91] Sunghwan Kim, William W. Clark, and Qing-Ming Wang. Piezoelectric energy harvesting with a clamped circular plate: Analysis. Journal of Intelligent Material Systems and Structures, 16(10):847–854, 2005.

[92] Sunghwan Kim, William W. Clark, and Qing-Ming Wang. Piezoelectric energy harvesting with a clamped circular plate: Experimental study. Journal of Intelligent Material Systems and Structures, 16(10):855–863, 2005.

[93] Shuichi Kinoshita, Shinya Yoshioka, and Kenji Kawagoe. Mechanisms of structural colour in the morpho butterfly: cooperation of regularity and irregularity in an iridescent scale. Proc. R. Soc. Lond. B, 269:1417–1421, 2002.

[94] Manvir S. Kushwaha. Band gap engineering in n-dimensional phononic crystals. In IMECE, November 5-10, Chicago, Illinois, USA, number 13416. ASME, 2006.

[95] Manvir S. Kushwaha, P. Halevi, L. Dobrzynski, and B. Djafari-Rouhani. Acoustic band structure of periodic elastic composites. Physical Review Letters, 71(13):2022–2025, 1993.

[96] Mickael Lallart, L. Garbuio, L. Petit, Claude Richard, and Daniel Guyomar. Double syncrhonized switch harvesting (dssh): a new energy harvesting scheme for efficient energy extraction. IEEE Transactions on Ultrasonics, Ferroelectrics, and Frequency Control, 55(10):2119–2130, 2008.

[97] Mickael Lallart and Daniel Guyomar. An optimizaed self-powered switching circuit for non-linear energy harvesting with low voltage output. Smart Materials and Structures, 17(035030), 2008.

[98] Philippe Langlet, Anne-Christine Hladky-Hennion, and Jean-Noel Decarpigny. Analysis of the propagation of plane acoustic waves in passive periodic materials using the finite element method. Journal of the Acoustical Society of America, 98(5):2792–2800, 1995.

[99] M. Lapine and S. Tretyakov. Contemporary notes on metamaterials. IET Microwaves, Antennas and Propagation, 1(1):3–11, 2007.

[100] Anders A. Larsen, Bogi Laksafoss, Jakob Søndergaard Jensen, and Ole Sigmund. Topological material layout in plates for vibration suppression and wave propagation control. Structural and Multidisciplinary Optimization, 2009.

[101] Elie Lefeuvre, Adrien Badel, A. Benayad, L. Lebrun, Claude Richard, and Daniel Guyomar. A comparison between several approaches of piezoelectric energy harvesting. J. Phys. IV France, 128:177–186, 2005.

[102] Elie Lefeuvre, Adrien Badel, Claude Richard, and Daniel Guyomar. Piezoelectric energy harvesting device optimization by synchronous electric charge extraction. Journal of Intelligent Material Systems and Structures, 16(10):865–876, 2005.

[103] Elie Lefeuvre, Adrien Badel, Claude Richard, and Daniel Guyomar. Energy harvesting using piezoelectric materials: Case of random vibrations. Journal of Electroceramics, 19:349–355, 2007.

[104] Elie Lefeuvre, Gael Sebald, Daniel Guyomar, Mickael Lallart, and Claude Richard. Materials, structures and power interfaces for efficient piezoelectric energy harvesting. Journal of Electroceramics, 2009.

[105] G. A. Lesieutre, G. K. Ottman, and H. F. Hofmann. Damping as a result of piezoelectric energy harvesting. Journal of Sound and Vibration, 269(3-5):991–1001, 2004.

[106] Zhengyou Liu, C. T. Chan, Ping Sheng, A. L. Goertzen, and J. H. Page. Elastic wave scattering by periodic structures of spherical objects: Theory and experiment. Physical Review B, 62(4):2446–2457, 2000.

[107] John Lysmer and Roger L. Kuhlemeyer. Finite dynamic model for infinite media. J. Eng. Mech. Div. ASCE, 95:859–877, 1969.

[108] Stephen A. Maas. Nonlinear microwave and RF circuits. Artech House Publishers, 2nd edition, 2003.

[109] Dragan Marinkovic, Heinz Koppe, and Ulrich Gabbert. Accurate modeling of the electric field within piezoelectric layers for active composite structures. Journal of Intelligent Material Systems and Structures, 18:503–513, 2007.

[110] Carmelo Militello and Carlos A. Felippa. The first andes elements: 9-dof plate bending triangles. Computer Methods in Applied Mechanics and Engineering, 93:217–246, 1991.

[111] Graeme W. Milton. The theory of composites. Cambridge University Press, Cambridge, 2002.

[112] Graeme W. Milton. New metamaterials with macroscopic behavior outside that of continuum elastodynamics. New Journal of Physics, 9(359), 2007.

[113] Graeme W. Milton. Waves in composites and metamaterials, 2007. Course notes: http://imechanica.org/node/870.

[114] Graeme W. Milton, Marc Briane, and John R. Willis. On cloaking for elasticity and physical equations with a transformation invariant form. New Journal of Physics, 8(248), 2006.

[115] Graeme W. Milton and Nicolae-Alexandru P. Nicorovici. On the cloaking effects associated with anomalous localized resonance. Proc. R. Soc. A, 462:3027–3059, 2006.

[116] Graeme W. Milton and John R. Willis. On modifications of newton's second law and linear continuum elastodynamics. Proc. R. Soc. A, 463:855–880, 2007.

[117] Changko Mo, Wright Rika, and William W. Clark. The effect of electrode pattern on the behaviour of piezoelectric actuators in a circular diaphragm structure. Journal of Intelligent Material Systems and Structures, 18(5):467–476, 2007.

[118] Allahyar Montazeri, Javad Poshtan, and Aghil Yousefi-Koma. The use of 'particle swarm' to optimize the control system in a pzt laminated plate. Smart Materials and Structures, 17(045027), 2008.

[119] D. P. Morgan. History of saw devices. In IEEE International Frequency Control Symposium, pages 439–460, 1998.

[120] Osama M. Mukdadi, Subhendu K. Datta, and Martin L. Dunn. Acoustic-phonon dispersion in nanowires. Journal of Applied Physics, 97(7), 2005.

[121] Roy H. Olsson, James G. Fleming, Ihab F. El-Kady, Melanie R. Tuck, and Frederick B. McCormick. Micromachined bulk wave acoustic bandgap devices. In in proceedings of the 14th International Conference on Solid-State Sensors, Actuators, and Microsystems, pages 317–321, 2007.

[122] G. K. Ottman, H. F. Hofmann, A. C. Bhatt, and G. A. Lesieutre. Adaptive piezoelectric energy harvesting circuit for wireless remote power supply. IEEE Transactions on Power Electronics, 17(5):669–676, 2002.

[123] Geffrey K. Ottman, Heath F. Hofmann, and George A. Lesieutre. Optimized piezoelectric energy harvesting circuit using step-down converter in discontinuous conduction mode. IEEE Transactions on Power Electronics, 18(2):696–703, 2003.

[124] Joseph M. Pajot. Topology Optimization of Geometrically Nonlinear Structures Including Thermo-Mechanical Coupling. PhD thesis, University of Colorado at Boulder, 2006.

[125] J. B. Pendry. Negative refraction makes a perfect lens. Physical Review Letters, 85(18):3966–3969, 2000.

[126] J. B. Pendry, David Schurig, and D. R. Smith. Controlling electromagnetic fields. Science, 312(1780), 2006.

[127] Yan Pennec, B. Djafari-Rouhani, J. O. Vasseur, Abdelkrim Khelif, and P. A. Deymier. Tunable filtering and demultiplexing in phononic crystals with hollow cylinders. Physical Review E, 69(046608), 2004.

[128] Dennis W. Prather, Shouyuan Shi, Janusz Murakowski, Garrett J. Schneider, Ahmed Sharkawy, Caihua Chen, and Binglin Miao. Photonic crystal structures and applications: Perspective, overview, and development. IEEE Journal of Selected Topics in Quantum Electronics, 12(6):1416–1437, 2006.

[129] S. Priya. Advances in energy harvesting using low profile piezoelectric transducers. Journal of Electroceramics, 19:167–184, 2007.

[130] John William Strutt Rayleigh. On the remarkable phenomenon of crystalline reflexion described by prof. stokes. Phil. Mag., 26:256–265, 1888.

[131] Jamil M. Renno, Mohammed F. Daqaq, and Daniel J. Inman. On the optimal energy harvesting from a vibration source. Journal of Sound and Vibration, 320(1-2):386–405, 2009.

[132] Vittorio Rizzoli, Alessandro Lipparini, Alessandra Costanzo, Franco Mastri, Claudio Cecchetti, Andrea Neri, and Diego Masotti. State-of-the-art harmonic-balance simulation of forced nonlinear microwave circuits by the piecewise technique. IEEE Transactions on Microwave Theory and Techniques, 40(1):12–28, 1992.

[133] V. Romero-Garcia, E. Fuster-Garcia, L. M. Garcia-Raffi, and J. V. Sanchez-Perez. Acoustic barriers based on sonic crystals. In in proceedings of the ASME International Design Engineering Technical Conferences and Computers and Information in Engineering Conference, Sept. 4-7, Las Vegas, Nevada, 2007.

[134] Zhichao Ruan, Min Yan, Curtis W. Neff, and Min Qiu. Ideal cylindrical cloak: perfect but sensitive to tiny perturbations. Physical Review Letters, 99(113903), 2007.

[135] K. Schittkowski. Nlpql: A fortran subroutine solving constrained nonlinear programming problems. Annals of Operations Research, 5:485–500, 1985.

[136] David Schurig, J. J. Mock, B. J. Justice, Steven A. Cummer, J. B. Pendry, A. F. Starr, and D. R. Smith. Metamaterial electromagnetic cloak at microwave frequencies. Science, 314:977–980, 2006.

[137] A. P. Seyranian, E. Lund, and N. Olhoff. Multiple eigenvalues in structural optimization problems. Struct. Multidisc. Optim., 8(4):207–227, 1994.

[138] Ping Sheng, Jun Mei, Zhengyou Liu, and Weijia Wen. Dynamic mass density and acoustic metamaterials. Physica B, 394(2):256–261, 2007.

[139] Y. C. Shu. Energy Harvesting Technologies, chapter Performance evaluation of vibration-based piezoelectric energy scavengers, pages 75–105. Springer, 2009.

[140] Y. C. Shu and I. C. Lien. Analysis of power output for piezoelectric energy harvesting systems. Smart Materials and Structures, 15:1499–1512, 2006.

[141] Y. C. Shu and I. C. Lien. Efficiency of energy conversion for a piezoelectric power harvesting system. Journal of Micromechanics and Microengineering, 16:2429–2438, 2006.

[142] Y. C. Shu, I. C. Lien, and W. J. Wu. An improved analysis of the sshi interface in piezoelectric energy harvesting. Smart Materials and Structures, 16:2253–2264, 2007.

[143] M. Sigalas and E. N. Economou. Band structure of elastic waves in two dimensional systems. Solid State Communications, 86(3):141–143, 1993.

[144] M. M. Sigalas. Defect states of acoustic waves in a two-dimensional lattice of solid cylinders. J. Appl. Phys., 84(6):3026–3030, 1998.

[145] M. M. Sigalas and E. N. Economou. Elastic and acoustic wave band structure. Journal of Sound and Vibration, 158(2):377–382, 1992.

[146] Ole Sigmund and Jakob Søndergaard Jensen. Systematic design of phononic band-gap materials and structures by topology optimization. Philosophical Transactions of the Royal Society A, 361(1806):1001–1019, 2003.

[147] Henry A. Sodano, Daniel J. Inman, and Gyuhae Park. A review of power harvesting from vibration using piezoelectric materials. The Shock and Vibration Digest, 36(3):197–205, 2004.

[148] Roman Stainko and Ole Sigmund. Tailoring group velocity by topology optimization. In WCSMO07, May 21-25, Seoul, Korea. ISSMO, 2007.

[149] George Gabriel Stokes. On a remarkable phenomenon of crystalline reflection. Proceedings of the Royal Society, 1885.

[150] Krister Svanberg. The method of moving asymptotes - a new method for structural optimization. Int. J. Numer. Meth. Engng, 24(2):359–373, 1987.

[151] Krister Svanberg. A class of globally convergent optimization methods based on conservative convex separable approximzations. SIAM Journal on Optimization, 12(2):555–573, 2002.

[152] Yukihiro Tanaka and Shin-Ichiro Tamura. Surface acoustic waves in two-dimensional periodic elastic structures. Physical Review B, 58(12):7958–7965, 1998.

[153] Yukihiro Tanaka and Shin-Ichiro Tamura. Acoustic stop bands of surface and bulk modes in two-dimensional phononic lattices consisting of aluminum and a polymer. Physical Review B, 60(19):13294–13297, 1999.

[154] Salvatore Torquato. Random heterogeneous materials: Microstructure and macroscopic properties. Springer, Harrisonburg, 2002.

[155] Daniel Torrent and Jose Sanchez-Dehesa. Acoustic metamaterials for new two-dimensional sonic devices. New Journal of Physics, 9(323), 2007.

[156] Daniel Torrent and Jose Sanchez-Dehesa. Anisotropic mass density by two-dimensional acoustic metamaterials. New Journal of Physics, 10(023004), 2008.

[157] D. A. Tortorelli and P. Michaleris. Design sensitivity analysis: Overview and review. Inverse Problems in Engineering, 1(1):71–105, 1994.

[158] S. Y. Wang, K. Tai, and S. T. Quek. Topology optimization of piezoelectric sensors/actuators for torsional vibration control of composite plates. Smart Materials and Structures, 15:253–269, 2006.

[159] Eli Yablonovitch. Inhibited spontaneous emission in solid-state physics and electronics. Physical Review Letters, 58(20):2059–2062, 1987.

[160] Eli Yablonovitch. Localization and propagation of classical waves in random and periodic structures, chapter Photonic Band Gaps. Plenum, New York, 1993.

[161] Eli Yablonovitch and T. J. Gmitter. Photonic band structure: The face-centered-cubic case. Physical Review Letters, 63(18):1950–1953, 1989.

[162] Xiangdong Zhang and Zhengyou Liu. Negative refraction of acoustic waves in two-dimensional phononic crystals. Applied Physics Letters, 85(2):341–343, 2004.

[163] Guozhong Zhao, Biaosong Chen, and Yuanxian Gu. Control-structural design optimization for vibration of piezoelectric intelligent truss structures. Structural and Multidisciplinary Optimization, 2009.

[164] Bin Zheng, Ching-Jui Chang, and Hae Chang Gea. Topology optimization of energy harvesting devices using piezoelectric materials. Structural and Multidisciplinary Optimization, 38(1):17–23, 2009.

[165] Yibing Zheng and Xiaojun Huang. Anisotropic perfectly matched layers for elastic waves in cartesian and curvilinear coordinates. In Earth Resources Laboratory 2002 Industry Consortium Meeting, Dept. of Earth, Atmospheric, and Planetary sciences, Cambridge, MA, USA, 2002.

Appendix A

Energy Harvesting with Nonlinear Circuits

A.1 Introduction

Piezoelectric harvesting systems consist of two distinct, but coupled parts: the piezoelectric harvesting structure and the harvesting circuit. The harvesting structure consists of a piezomechanical system under harmonic or broadband vibration. The piezoelectric component of this system converts mechanical strain to electrical charge and voltage, which vary as a function of time. The design of harvesting structures considered in chapter 6 and elsewhere (see Anton and Sodano (2007) and Erturk and Inman (2008) for recent reviews) consider only linear harvesting circuits. Generally, however, the harvesting circuit is designed to condition the electrical energy for compatibility, typically by using full-bridge rectifiers or other circuit components that have nonlinear voltage/current relationships. A number of specialized circuits have been developed to serve this purpose with various performance improvements including synchronous electric charge extraction [102], synchronized switch harvesting on inductor circuits (SSHI) [65, 142], and others [105, 123]. Lefeuvre et al. [101, 104] give a review of many of these harvesting circuits.

A number of authors have provided simplified analysis techniques to analyze nonlinear harvesting circuits. Shu and Lien [141, 140] provide an analytical analysis of systems with full-bridge rectifiers, which expands on previous work by Ottman et al. [122]. Shu, Lien, and Wu [142] and Lallart and Guyomar [97] perform similar analysis

on SSHI-type harvesting circuits and Lallart et al. [96] for DSSH-type circuits. The methods used in these papers all make assumptions on the shape of the voltage and current waveforms, which are guided by assuming that the diodes behave ideally, i.e. they are perfect conductors for positive voltage and perfect insulators for negative voltage. In a different study, Elvin and Elvin [39] make the same assumptions on the diodes but use a numerical transient electrical circuit simulator to calculate the harvesting power. In addition to the simplified circuit analysis techniques, all of these analysis techniques also use lumped parameter models for the piezoelectric harvesting structure, generally at resonance only. There are currently no studies that have incorporated nonlinear harvesting circuit analysis with a high fidelity finite element model of the harvesting structure. As such, current models and methods are incapable of analyzing the mechanical and electrical response from effects such as higher order feedback from the circuit or non-saturated diodes from low vibration environments. These are phenomena that have not yet been shown for energy harvesters with nonlinear circuits. Additionally, the design of piezoelectric harvesting structures, which is currently performed with linear circuit models [46, 40, 44, 45] (see also chapter 6 of this document), is limited by the lack of an accurate solution scheme.

Here, a methodology for quantitatively analyzing nonlinear energy harvesting circuits connected to a piezoelectric harvesting structure is developed. The goal is to provide an accurate prediction/evaluation tool for piezoelectric energy harvesting systems with nonlinear circuits and to at least partially answer the question of whether the nonlinearities play a significant role in the response of such systems. The methodology is based on the harmonic balance technique commonly used in the analysis of nonlinear microwave and radio frequency circuits. The harmonic balance algorithm developed by Rizzoli et al. [132] and described further by Maas [108] is modified and expanded by introducing a variable current source, namely the piezoelectric harvester, which is subject to circuit feedback. In illustrative examples, piezoelectric harvesting systems are

analyzed with full-bridge rectifier circuits where the piezoelectric harvester is subject to a harmonic force. It is then shown that the assumptions of previous analytical models can be overly restrictive, particularly when the diodes are not saturated (i.e. not acting ideally). In this case there is a definite dependence on the magnitude of vibration to which the piezoelectric harvester is subjected, whereas in the analytical models there is no dependence. A second important finding is described in the examples where feedback from the nonlinear circuit into the piezoelectric harvesting structure will excite higher order vibrations, which could potentially excite higher order structural modes in either the harvesting structure or host to which it is attached. This is an effect that may be of concern in some vibration sensitive systems.

This appendix is organized as follows. First the analysis methodology is presented with descriptions of the circuit components, the piezoelectric harvester models that are used, and the implementation of the modified harmonic balance algorithm. Next, examples of systems with lumped parameter and finite element models are provided with discussion. This is finished with a conclusion.

A.2 Analysis methodology

The following outlines a general methodology for the analysis of a linear piezoelectric harvesting structure coupled to a nonlinear circuit as applied to a full-bridge rectifier circuit. The system consists of two distinct, but interdependent, components as shown in Figure A.1: the electrical circuit, which may consist of both linear and nonlinear elements, and the piezoelectric harvesting structure, for which both lumped parameter and finite element models are considered. For the electrical circuit a full-bridge rectifier is considered. The two components are coupled through the voltages and currents they share. An accurate solution for both the electrical and structural responses of this fully coupled electromechanical problem is sought.

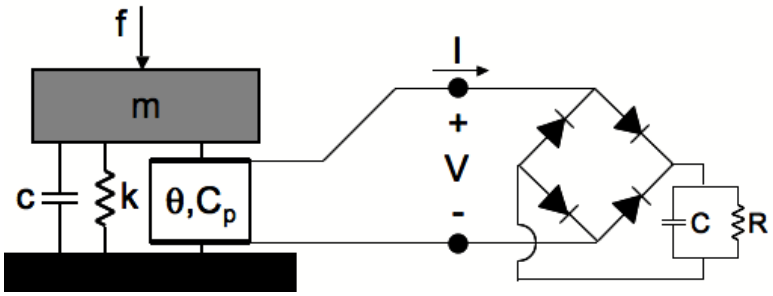

Figure A.1: Schematic of the coupled electromechanical energy harvesting system with a lumped parameter model and full-bridge rectifier.

A.2.1 Circuit model

The model of the electrical circuit may consist of both linear and nonlinear elements. The full-bridge rectifier consists of four nonlinear diodes connected to a resistor and capacitor in parallel, which are linear. The diodes are assumed to have a current/voltage relationship of the Shockley diode form:

$$i^{diode}(t) = I_{sat}\left(\exp\left(\frac{v(t)}{\eta\delta}\right) - 1\right) \tag{A.1}$$

where I_{sat}, η, and δ are the diode reverse-leakage current, ideality factor, and thermal voltage, respectively. In the linear circuit components, the current/voltage relationship can be formulated in the frequency domain as:

$$I^{lin} = \left(\frac{1}{R} + j\omega C\right)\Delta V \tag{A.2}$$

where the resistance R is specified and the capacitance C is usually considered to be "sufficiently large" such that the ripple voltage is small relative to the DC voltage. Here, the capacitance is set by assuming a consistent RC time constant τ such that $C = \tau/R$, which allows for a "sufficiently large" capacitance but which is not so large to cause numerical difficulties.

A.2.2 Piezoelectric harvester model

The equations of motion for the piezoelectric harvester can be formulated using a number of methods. In this study, lumped parameter and finite element models are used as described here.

A.2.2.1 Lumped parameter model

In the lumped parameter model of the piezoelectric harvester the governing equations for a single degree of freedom model can be written as:

$$\begin{array}{rrrrcr} m\ddot{u}+ & c\dot{u}+ & ku+ & \theta V_{piezo} & = & F \\ & & -\theta\dot{u}+ & C_p\dot{V}_{piezo} & = & -I^{lin}_{piezo} \end{array} \tag{A.3}$$

where m, c, k, θ, C_p, u, V_{piezo}, F, and I^{lin}_{piezo} are the lumped mass, mechanical damping, stiffness, piezoelectric coupling, piezoelectric capacitance, displacement, external force, and current, respectively, and the overdot is differentiation with respect to time. Using the time-harmonic assumptions $u = u_0 e^{j\omega t}$, $V_{piezo} = V_0 e^{j\omega t}$, $F = F_0 e^{j\omega t}$, $I^{lin}_{piezo} = I_0 e^{j\omega t}$ with angular frequency ω and rearranging (A.3) so that the voltage is the independent variable with the current as the dependent variable results in the system:

$$\begin{bmatrix} (k + j\omega c - \omega^2 m) & 0 \\ j\omega\theta & -1 \end{bmatrix} \begin{pmatrix} u \\ I^{lin}_{piezo} \end{pmatrix} = \begin{pmatrix} F - \theta V_{piezo} \\ j\omega C_p V_{piezo} \end{pmatrix} \tag{A.4}$$

from which one can obtain the current as a function of voltage and external force. Multiple degree of freedom models can also be easily formulated in this manner.

Following Shu and Lien [140], several non-dimensional quantities can be defined for the lumped parameter model, which are reproduced here for convenience:

$$k_e^2 = \frac{\theta^2}{kC_p},\ \zeta = \frac{c}{2\sqrt{km}},\ \omega_{sc} = \sqrt{\frac{k}{m}},\ \Omega = \frac{\omega}{\omega_{sc}} \tag{A.5}$$

where k_e is the electromechanical coupling coefficient, ζ is the mechanical damping ratio, ω_{sc} is the short circuit natural frequency, and Ω is the normalized frequency.

A.2.2.2 Finite element model

When using a finite element model as the piezoelectric harvester, the system of equations consists of a large number of displacement and voltage degrees of freedom to produce a high fidelity model. The system of finite element equations can be written under time-harmonic assumptions as:

$$\begin{bmatrix} \left(\mathbf{K} + j\omega\mathbf{C} - \omega^2\mathbf{M}\right) & \mathbf{\Theta} \\ \mathbf{\Theta}^T & \mathbf{C}_p \end{bmatrix} \begin{pmatrix} \mathbf{u} \\ \mathbf{V} \end{pmatrix} = \begin{pmatrix} \mathbf{F} \\ \mathbf{Q} \end{pmatrix} \rightarrow \tilde{\mathbf{K}}\tilde{\mathbf{u}} = \tilde{\mathbf{f}} \tag{A.6}$$

where $\mathbf{K}$, $\mathbf{C}$, $\mathbf{M}$, $\mathbf{\Theta}$, and $\mathbf{C}_p$ are the stiffness, damping, mass, piezoelectric coupling, and capacitance matrices, $\mathbf{u}$ and $\mathbf{V}$ are the displacement and voltage solution vectors, $\mathbf{F}$ and $\mathbf{Q}$ are the external force and charge vectors, respectively. This system represents the unconnected piezoelectric harvester. To facilitate the calculation of generated harvester current, which is used to couple the harvester to the circuit, a low value test resistor R_{test} is added to the system connecting a harvester voltage degree of freedom V_{peizo} and a new voltage degree of freedom V_{test}. The lumped parameter form for this resistor in time-harmonic analysis is:

$$-j\frac{1}{\omega R_{test}} \begin{bmatrix} 1 & -1 \\ -1 & 1 \end{bmatrix} \mathbf{V}^e = \mathbf{Q}^e. \tag{A.7}$$

The low resistivity of the resistor ensures its influence on the system dynamics is minimal, yet it enables the calculation of the generated harvester current I^{lin}_{piezo} via:

$$I^{lin}_{piezo} = \frac{V_{test} - V_{piezo}}{R_{test}}. \tag{A.8}$$

The new voltage degree of freedom V_{test} can then also be used as the harvester voltage since $V_{piezo} \approx V_{test}$.

A.2.3 Solution algorithm

To solve the combined system of piezoelectric harvesting structure and electric harvesting circuit, a modified harmonic balance algorithm is used. In a linear circuit

with a time-harmonic forcing function (in our case the mechanical forcing function on the piezoelectric harvester) the voltage and current response is also time-harmonic with the same frequency. If nonlinear elements are included, however, higher order responses occur and the system is no longer harmonic with a single frequency. The general idea behind the harmonic balance algorithm is to assume that the nonlinear elements of the circuit can be represented by convergent polynomial expansions. Under this assumption, the response of the circuit will be a harmonic function of the driving frequency and its harmonics (i.e. 0, f_0, $2f_0$, $3f_0$, $\ldots$). Using this information, one can also use convergent series approximations for the circuit voltage and current waveforms, since all polynomial operations on these harmonic functions result in the same set of harmonic functions. Thus the nonlinear problem can be separated into a set of linear harmonic problems, one for each frequency. In the harmonic balance algorithm the goal is to "balance" the voltages and currents across and through each of the circuit components for each of these harmonic problems, thereby solving for the series coefficients of the voltage and current waveforms, which can be found via Fourier Transforms. This formulation allows for the nonlinear steady-state problem to be solved via a sequence of simple linear time-harmonic subproblems.

In the harmonic balance algorithm described by Maas (2003), one can setup the problem as either a nodal or port formulation. The approach developed here is based on the nodal formulation where at each circuit node (circuit junction) Kirchhoff's current law is used to form a residual of currents into the node for a given set of nodal voltages. More specifically, the currents for each of the harmonic subproblems must be "balanced" at each node. The balancing is then performed by minimizing the current residuals through some residual reduction technique such as Newton's method. The series approximation can also be truncated, whereby solution accuracy is sacrificed for a reduction in computational effort.

This basic procedure features a robust convergence only for circuits with a mod-

erately nonlinear behavior. In the presence of strong nonlinearities, which are caused by diodes in the present problem, Newton and Newton-like methods are not guaranteed to converge and the linearized sub-problem may suffer from ill-conditioning. This was also observed in the present study. In order to remedy this, Rizzoli et al. [132] introduced a piecewise formulation that splits the nonlinearity between voltage and current by introducing a fictitious state variable. This technique uses the port formulation of the circuit problem where voltages are measured across ports rather than at nodes and the port currents form the residuals, resulting in a better-conditioned system. In the port formulation, however, certain circuits such as full-bridge rectifiers lead to a highly disconnected (singular) admittance matrix used in the harmonic balance technique. Maas [108] outlines several techniques for addressing this problem, but they generally add to the complexity of the algorithm.

Here, rather than use either the nodal or port formulations of the harmonic balance algorithm, a hybrid approach is developed that provides both clarity and stability to the algorithm for the types of problems of concern to piezoelectric energy harvesting. In particular, the response of a piezoelectric harvester connected to a full-bridge rectifier, as shown in Figure A.2, is needed. The hybrid formulation is based on the nodal approach where the currents into the three nodes form three vectors harmonic coefficient residuals. In addition, as a matter of numerical stabilization, the nonlinear splitting technique of Rizzoli et al. [132] is used to parameterize the voltage current relationship for the diodes as:

$$\begin{aligned} v^{diode}\left(x\left(t\right)\right) &= \begin{cases} \hat{V} + \frac{1}{\alpha}\ln\left(1+\alpha\left[x\left(t\right)-\hat{V}\right]\right), & \hat{V} \leq x\left(t\right) \\ x\left(t\right), & x\left(t\right) \leq \hat{V} \end{cases} \\ i^{diode}\left(x\left(t\right)\right) &= \begin{cases} I_{sat}\left(\exp\left(\alpha\hat{V}\right)\left(1+\alpha\left[x\left(t\right)-\hat{V}\right]\right)-1\right), & \hat{V} \leq x\left(t\right) \\ I_{sat}\left(\exp\left(\alpha x\left(t\right)\right)-1\right), & x\left(t\right) \leq \hat{V} \end{cases} \end{aligned} \tag{A.9}$$

where $x\left(t\right)$ is the state variable, $\alpha = 1/\eta\delta$, and $\hat{V}$ is a parameter chosen to optimize

algorithm performance. Via Rizzoli et al. [132], $\hat{V} = \ln(\gamma/\alpha I_{sat})/\alpha$ is used with $\gamma = 1$. There are now four additional state variables, which can be written in the same set of harmonic functions as the current and voltage because the parametric form can be written in a convergent Taylor series. From these state variables constraint equations are written for the voltage across the diodes. Overall, this results in seven residual equations:

$$\begin{aligned}
&i_1^{lin} + i_1^{NL} = i_1^{lin}(v_1, v_2) + i_1^{diode}(x_1) + i_2^{diode}(x_2) = 0 \\
&i_2^{lin} + i_2^{NL} = i_2^{lin}(v_1, v_2) - i_3^{diode}(x_3) - i_4^{diode}(x_4) = 0 \\
&i_{piezo}^{lin} + i_3^{NL} = i_{piezo}^{lin}(v_3) - i_1^{diode}(x_1) + i_4^{diode}(x_4) = 0 \\
&v_1 - v_3 + v_1^{diode}(x_1) = 0 \\
&v_1 + v_2^{diode}(x_2) = 0 \\
&-v_2 + v_3^{diode}(x_3) = 0 \\
&-v_2 + v_3 + v_4^{diode}(x_4) = 0
\end{aligned} \tag{A.10}$$

for seven variables v_1, v_2, v_3, x_1, x_2, x_3, x_4. Transforming these into the frequency domain and taking only the DC component and K lowest harmonics results in a residual vector of size $7 \cdot (K+1)$ whose solution solves the electromechanical problem.

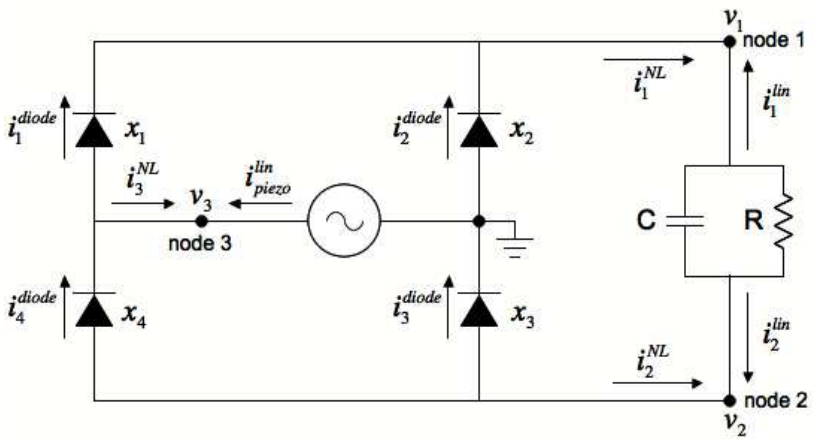

Figure A.2: Full-bridge rectifier circuit with linear piezoelectric harvester.

To solve the set of residual equations the hybrid harmonic balance algorithm

outlined in Algorithm A-1 is used, which employs Newton's method. The algorithm solves the nonlinear circuit equations for a constant driving frequency f_0, a constant harvesting resistance R, and a constant force magnitude Y_0 applied to the piezoelectric harvester. The algorithm requires calculations both in the time and frequency domains, for which the voltages, currents, and state variables are written in lower case in the time domain (v, i, and x) and upper case in the frequency domain (V, I, and X). Frequency transforms are performed via the Fast Fourier Transform algorithm. Newton's method requires the computation of the Jacobian of the residual equations. This sub-step is described in detail in the next section.

Algorithm A-1

1) Form a vector of driving frequency and harmonics:

$\vec{f} = (0, f_0, 2f_0, 3f_0, \ldots, , kf_0) \;\; k = 0 \ldots K$

2) Make an initial estimate of the voltage and state variable waveforms in the frequency domain:

$V_1 = V_1^0\left(\vec{f}\right),\; V_2 = V_2^0\left(\vec{f}\right),\; V_3 = V_3^0\left(\vec{f}\right)$

$X_1 = X_1^0\left(\vec{f}\right),\; X_2 = X_2^0\left(\vec{f}\right),\; X_3 = X_3^0\left(\vec{f}\right),\; X_4 = X_4^0\left(\vec{f}\right)$

3) Using the voltages, calculate the linear currents and their gradients w.r.t. the voltages at each of the nodes for the piezoelectric harvester:

$\left[I_{piezo}^{lin}\left(\vec{f}\right), \frac{dI_{piezo}^{lin}}{dV_3}\left(\vec{f}\right)\right] = \mathcal{F}_{piezo}\left(\vec{f}, V_3, Y_0\right)$

4) Similarly, calculate the linear currents and their gradients for the linear circuit components:

$\left[I_1^{lin}\left(\vec{f}\right), \frac{dI_1^{lin}}{dV_1}\left(\vec{f}\right), \frac{dI_1^{lin}}{dV_2}\left(\vec{f}\right), I_2^{lin}\left(\vec{f}\right), \frac{dI_2^{lin}}{dV_1}\left(\vec{f}\right), \frac{dI_2^{lin}}{dV_2}\left(\vec{f}\right)\right] =$

$\mathcal{F}_{linearcircuit}\left(\vec{f}, V_1, V_2\right)$

5) Transform the state variables into the time domain with imaginary unit j:

$x_p(t) = \sum_{q=-K}^{K} X_p(q \cdot f_0) \exp\left(q \cdot (2\pi j \cdot f_0 t)\right),\; p = 1 \ldots 4$

6) Calculate the nonlinear currents at each of the nodes and the voltages across each of the diodes using the state variable waveforms:

$$i_1^{NL} = \mathcal{F}_1^{diodes}(x_1, x_3) = i_1^{diode}(x_1) + i_2^{diode}(x_3)$$

$$i_2^{NL} = \mathcal{F}_2^{diodes}(x_2, x_3) = -i_3^{diode}(x_3) - i_4^{diode}(x_4)$$

$$i_3^{NL} = \mathcal{F}_3^{diodes}(x_1, x_2, x_3) = -i_1^{diode}(x_1) + i_4^{diode}(x_4)$$

$$v_1^{NL} = v_1^{diode}(x_1)$$

$$v_2^{NL} = v_2^{diode}(x_2)$$

$$v_3^{NL} = v_3^{diode}(x_3)$$

$$v_4^{NL} = v_4^{diode}(x_4)$$

7) Calculate the gradients of the nonlinear currents w.r.t. the state variables:

$$g_{m,p}^{NL} = \frac{di_m^{NL}}{dx_p} = \begin{cases} \alpha I_{sat} \exp\left(\alpha \hat{V}\right), & \hat{V} \leq x(t) \\ \alpha I_{sat} \exp\left(\alpha x(t)\right), & x(t) \leq \hat{V} \end{cases}$$

8) Calculate the gradients of the voltages across the diodes w.r.t. the state variables:

$$h_{n,p}^{NL} = \frac{dv_n^{NL}}{dx_p} = \begin{cases} \left(1 + \alpha\left[x(t) - \hat{V}\right]\right)^{-1}, & \hat{V} \leq x(t) \\ 1, & x(t) \leq \hat{V} \end{cases}$$

9) Transform the nonlinear currents, diode voltages, and all gradients into the frequency domain using Fast Fourier Transforms and take only the frequency components in $\vec{f}$:

$$\tilde{I}_m^{NL} = fft\left(i_m^{NL}\right), \tilde{G}_{m,p}^{NL} = fft\left(g_{m,p}^{NL}\right)$$

$$\tilde{V}_n^{NL} = fft\left(v_n^{NL}\right), \tilde{H}_{n,p}^{NL} = fft\left(h_{n,p}^{NL}\right)$$

$$I_m^{NL}\left(\vec{f}\right) = reduce\left(\tilde{I}_m^{NL}\right), G_{m,p}^{NL}\left(\vec{f}\right) = reduce\left(\tilde{G}_{m,p}^{NL}\right)$$

$$V_n^{NL}\left(\vec{f}\right) = reduce\left(\tilde{V}_n^{NL}\right), H_{n,p}^{NL}\left(\vec{f}\right) = reduce\left(\tilde{H}_{n,p}^{NL}\right)$$

10) Form the residual vector containing the sum of the currents at the nodes and the voltage-state variable constraint for each diode:

$$\overrightarrow{R} = \begin{pmatrix} I_1^{lin} + I_1^{NL} \\ I_2^{lin} + I_2^{NL} \\ I_{piezo}^{lin} + I_3^{NL} \\ V_1 - V_3 + V_1^{NL} \\ V_1 + V_2^{NL} \\ -V_2 + V_3^{NL} \\ -V_2 + V_3 + V_4^{NL} \end{pmatrix}$$

11) Form the Jacobian (see section Formulation of the Jacobian).

$$\mathbf{J} = \mathcal{F}_{Jacobian}\left(\frac{dI_m^{lin}}{dV_n}, G_{m,p}, H_{n,p}\right)$$

12) Use the Jacobian and residual vector to update the voltages and state variables via a Newton iteration:

$$\begin{pmatrix} \vec{V} \\ \vec{X} \end{pmatrix}^{new} = \begin{pmatrix} \vec{V} \\ \vec{X} \end{pmatrix} - \mathbf{J}^{-1}\vec{R}$$

13) If the inverse of the Jacobian does not reduce the residual then use the pseudo-inverse.

$$\begin{pmatrix} \vec{V} \\ \vec{X} \end{pmatrix}^{new} = \begin{pmatrix} \vec{V} \\ \vec{X} \end{pmatrix} - \mathbf{J}^{+}\vec{R}$$

14) If the norm of the residual vector ϵ is sufficiently small, then the solution has converged, otherwise return to step 3.

$$\epsilon = \left|\vec{R}\right|$$

Regarding the use of the pseudo-inverse in step 13. Firstly, while the piecewise nonlinearity splitting for the diodes was found to result in a better-conditioned nonlinear system (i.e. Jacobian), at high voltages or with a large number of harmonics the Jacobian was still often ill-conditioned. Much of this is due to the nature of the linear components of the circuit (i.e. resistor/capacitor and piezoelectric harvester) whose gra-

dients and higher harmonic currents increase dramatically with voltage and frequency while the gradients for the nonlinear components stay generally constant. The pseudo-inverse ignores singular or nearly singular values and as a result does not suffer from ill-conditioning, yet it retains most of the important information for this problem. Secondly, the pseudo-inverse is not computationally expensive due to the small size of the Jacobian in these problems. In practice the pseudo-inverse was used sparingly, usually in the initial Newton step where the regular inverse would predict a new variable set that often increased the residual by many orders of magnitude, indicating a poor initial guess for the variables.

A.2.4 Formulation of the Jacobian

In the frequency domain the currents, voltages, and state variables are complex valued and only represent half of the waveform for a given $f > 0$, corresponding to the positive, but not negative, frequency components of the signal. The concept of negative frequency may be confusing at first, but consider that in order to reconstruct the waveform from the frequency domain to the time domain one must sum the components from $-K$ to K:

$$\begin{aligned} i_m(t) &= \sum_{k=-K}^{K} I_m(k \cdot f_0) \exp(k \cdot (2\pi j \cdot f_0 t)) \\ v_n(t) &= \sum_{l=-K}^{K} V_n(l \cdot f_0) \exp(l \cdot (2\pi j \cdot f_0 t)) \\ x_p(t) &= \sum_{q=-K}^{K} X_p(q \cdot f_0) \exp(q \cdot (2\pi j \cdot f_0 t)) \end{aligned} \tag{A.11}$$

where negative frequency components of the transform are the conjugate $(\cdot)^*$ at the same positive frequency:

$$\begin{aligned} I_m(-k \cdot f_0) &= I_m^*(k \cdot f_0) \\ V_n(-l \cdot f_0) &= V_n^*(l \cdot f_0) \\ X_p(-q \cdot f_0) &= X_p^*(q \cdot f_0) \end{aligned} \quad . \tag{A.12}$$

The derivative of the currents and voltages w.r.t. the state variables then must consider both positive and negative frequency components:

$$\begin{aligned} dI_m\left(k\cdot f_0\right) &= \tfrac{\partial I_m(k\cdot f_0)}{\partial X_p(q\cdot f_0)} dX_p\left(q\cdot f_0\right) + \tfrac{\partial I_m(k\cdot f_0)}{\partial X_p(-q\cdot f_0)} dX_p\left(-q\cdot f_0\right) \\ dV_n\left(l\cdot f_0\right) &= \tfrac{\partial V_n(l\cdot f_0)}{\partial X_p(q\cdot f_0)} dX_p\left(q\cdot f_0\right) + \tfrac{\partial V_n(l\cdot f_0)}{\partial X_p(-q\cdot f_0)} dX_p\left(-q\cdot f_0\right) \end{aligned} \tag{A.13}$$

where

$$\begin{aligned} \tfrac{\partial I_m(k\cdot f_0)}{\partial x_p(q\cdot f_0)} &= G_{m,p}\left((k-q)\cdot f_0\right) \\ \tfrac{\partial I_m(k\cdot f_0)}{\partial x_p(-q\cdot f_0)} &= G_{m,p}\left((k+q)\cdot f_0\right) \\ \tfrac{\partial V_n(l\cdot f_0)}{\partial x_p(q\cdot f_0)} &= H_{n,p}\left((l-q)\cdot f_0\right) \\ \tfrac{\partial V_n(l\cdot f_0)}{\partial x_p(-q\cdot f_0)} &= H_{n,p}\left((l+q)\cdot f_0\right) \end{aligned} . \tag{A.14}$$

for which the $(k-q)$ and $(l-q)$ terms may have negative frequency components. Because of the negative frequencies and the conjugate in the transform components, the gradients must be separated into real and imaginary parts:

$$\begin{aligned} \begin{pmatrix} dI_m^R\left(k\cdot f_0\right) \\ dI_m^I\left(k\cdot f_0\right) \end{pmatrix} &= \left[\mathbf{J}_{mp}^G\left(k,q\right)\right] \begin{pmatrix} dX_p^R\left(q\cdot f_0\right) \\ dX_p^I\left(q\cdot f_0\right) \end{pmatrix} \\ \begin{pmatrix} dV_n^R\left(l\cdot f_0\right) \\ dV_n^I\left(l\cdot f_0\right) \end{pmatrix} &= \left[\mathbf{J}_{np}^H\left(l,q\right)\right] \begin{pmatrix} dX_p^R\left(q\cdot f_0\right) \\ dX_p^I\left(q\cdot f_0\right) \end{pmatrix} \end{aligned} \tag{A.15}$$

such that the components of the Jacobian are:

$$\begin{aligned} &\mathbf{J}_{mp}^G\left(k,q\right) = \\ &\begin{bmatrix} G_{m,p}^R\left((k-q)\cdot f_0\right) + G_{m,p}^R\left((k+q)\cdot f_0\right) & -G_{m,p}^I\left((k-q)\cdot f_0\right) + G_{m,p}^I\left((k+q)\cdot f_0\right) \\ G_{m,p}^I\left((k-q)\cdot f_0\right) + G_{m,p}^I\left((k+q)\cdot f_0\right) & G_{m,p}^R\left((k-q)\cdot f_0\right) - G_{m,p}^R\left((k+q)\cdot f_0\right) \end{bmatrix} \\ &\mathbf{J}_{np}^H\left(l,q\right) = \\ &\begin{bmatrix} H_{n,p}^R\left((l-q)\cdot f_0\right) + H_{n,p}^R\left((l+q)\cdot f_0\right) & -H_{n,p}^I\left((l-q)\cdot f_0\right) + H_{n,p}^I\left((l+q)\cdot f_0\right) \\ H_{n,p}^I\left((l-q)\cdot f_0\right) + H_{n,p}^I\left((l+q)\cdot f_0\right) & H_{n,p}^R\left((l-q)\cdot f_0\right) - H_{n,p}^R\left((l+q)\cdot f_0\right) \end{bmatrix} \end{aligned} \tag{A.16}$$

which constitute the parts of the Jacobian originating from the nonlinear components of the circuit.

The gradients forming the linear components of the Jacobian include those from the linear circuit and the piezoelectric harvester. In the linear circuit of our full-bridge rectifier model, the currents into nodes 1 and 2 can be written from (A.2) as:

$$\begin{aligned} I_1^{lin} &= \left(\tfrac{1}{R} + j\omega C\right)(V_2 - V_1) \\ I_2^{lin} &= \left(\tfrac{1}{R} + j\omega C\right)(V_1 - V_2) \end{aligned} \tag{A.17}$$

where gradients of these currents w.r.t. the voltages are:

$$\begin{aligned} \tfrac{dI_1^{lin}}{dV_1} &= -\left(\tfrac{1}{R} + j\omega C\right) \\ \tfrac{dI_1^{lin}}{dV_2} &= \left(\tfrac{1}{R} + j\omega C\right) \\ \tfrac{dI_2^{lin}}{dV_1} &= \left(\tfrac{1}{R} + j\omega C\right) \\ \tfrac{dI_2^{lin}}{dV_2} &= -\left(\tfrac{1}{R} + j\omega C\right) \end{aligned} \tag{A.18}$$

from which it is easy to see that the higher harmonics produce large entries in the Jacobian that may lead to scaling problems and ill-conditioning. For the piezoelectric harvester equations the gradient of the generated current in the lumped model from (A.4) can be found via:

$$\begin{bmatrix} \left(k + j\omega c - \omega^2 m\right) & 0 \\ j\omega\theta & -1 \end{bmatrix} \begin{pmatrix} \frac{du}{dV} \\ \frac{dI}{dV} \end{pmatrix} = \begin{pmatrix} \theta \\ j\omega C_p \end{pmatrix}. \tag{A.19}$$

For the finite element model, the gradient of the current w.r.t. the test voltage from (A.8) is:

$$\frac{dI_{piezo}^{lin}}{dV_{test}} = \frac{\partial I_{piezo}^{lin}}{\partial V_{test}} + \frac{\partial I_{piezo}^{lin}}{\partial V_{piezo}}\frac{dV_{piezo}}{dV_{test}} = \frac{1}{R_{test}}\left(1 - \frac{dV_{piezo}}{dV_{test}}\right) \tag{A.20}$$

where the derivative of the harvester voltage w.r.t. the test voltage can be found by differentiating the system of finite element equations:

$$\frac{d}{dV_{test}}\left(\tilde{\mathbf{K}}\tilde{\mathbf{u}} = \tilde{\mathbf{f}}\right) \rightarrow \tilde{\mathbf{K}}\frac{d\tilde{\mathbf{u}}}{dV_{test}} = \frac{d\tilde{\mathbf{f}}}{dV_{test}} \tag{A.21}$$

from which $\frac{dV_{piezo}}{dV_{test}}$ is obtained from $\frac{d\tilde{\mathbf{u}}}{dV_{test}}$ and where $\frac{d\tilde{\mathbf{f}}}{dV_{test}}$ is a vector of zeros except at the degree of freedom for V_{piezo}. The bulk of the computational expense here comes from the factorization of the finite element system. If this is stored for each of the

$(K+1)$ harmonics, however, then the calculation of $\frac{d\tilde{\mathbf{u}}}{dV_{test}}$ is computationally inexpensive, making the harmonic balance algorithm tractable with finite element models.

These linear components, for which the harmonics are independent of each other, have Jacobian submatrices as:

$$\mathbf{J}_{mn}^{lin} = \begin{cases} \begin{bmatrix} \mathrm{Re}\left(\frac{dI_m^{lin}}{dV_n}\right) & -\mathrm{Im}\left(\frac{dI_m^{lin}}{dV_n}\right) \\ \mathrm{Im}\left(\frac{dI_m^{lin}}{dV_n}\right) & \mathrm{Re}\left(\frac{dI_m^{lin}}{dV_n}\right) \end{bmatrix}, & m = n \\ \begin{bmatrix} 0 & 0 \\ 0 & 0 \end{bmatrix}, & otherwise \end{cases} \tag{A.22}$$

resulting in a 2x2 block diagonal structure. The nonlinear circuit component contributions, on the other hand, are fully populated. In each of the submatrices, the second row and column are empty because the imaginary part of the DC current/voltage $(k = l = q = 0)$ is always zero. These entries thus make the Jacobian singular, which can be easily remedied by either removing those rows/columns or setting the entry on the diagonal to 1.

In the case of the full-bridge rectifier model, the full Jacobian can be assembled as:

$$\mathbf{J} = \begin{bmatrix} \mathbf{J}_{11}^{lin} & \mathbf{J}_{12}^{lin} & 0 & \mathbf{J}_{11}^{G} & \mathbf{J}_{12}^{G} & 0 & 0 \\ \mathbf{J}_{21}^{lin} & \mathbf{J}_{22}^{lin} & 0 & 0 & 0 & \mathbf{J}_{23}^{G} & \mathbf{J}_{24}^{G} \\ 0 & 0 & \mathbf{J}_{33}^{lin} & \mathbf{J}_{31}^{G} & 0 & 0 & \mathbf{J}_{34}^{G} \\ \mathbf{I} & 0 & -\mathbf{I} & \mathbf{J}_{11}^{H} & 0 & 0 & 0 \\ \mathbf{I} & 0 & 0 & 0 & \mathbf{J}_{22}^{H} & 0 & 0 \\ 0 & -\mathbf{I} & 0 & 0 & 0 & \mathbf{J}_{33}^{H} & 0 \\ 0 & -\mathbf{I} & \mathbf{I} & 0 & 0 & 0 & \mathbf{J}_{44}^{H} \end{bmatrix} \text{ for } \begin{pmatrix} \vec{V} \\ \vec{X} \end{pmatrix} = \begin{pmatrix} V_1 \\ V_2 \\ V_3 \\ X_1 \\ X_2 \\ X_3 \\ X_4 \end{pmatrix} \tag{A.23}$$

where $\mathbf{I}$ is an identity matrix with a zero in the $(2,2)$ entry.

A.3 Examples

The following examples are used to illustrate the correctness and versatility of the present methodology in solving piezoelectric energy harvesting problems with nonlinear circuits. The examples include a lumped parameter model and a finite element model of the piezoelectric harvesting structure connected to full-bridge rectifier circuits.

A.3.1 Lumped parameter model

In the first example, a single degree of freedom lumped parameter model is used as the piezoelectric harvester. This model is commonly used in the literature and provides a direct comparison between this methodology and those results. The lumped parameters are selected as $k = 1.0$ N/m, $c = 9.55$ kg/sec, $m = 2.53E-6$ kg, $\theta = 1.25E-3$ N/V, $C_p = 1.2E-6$ F so that the resulting non-dimensional parameters are $\omega_{sc} = 100$ Hz, $k_e = 1.14$, and $\zeta = 0.03$, which correspond to the strongly coupled case of Shu and Lien [140]. A force acting on the mass actuates the mechanical vibration. The diodes in the circuit are modeled with the physically relevant parameters: $I_{sat} = 18.8E-9$ A, $\eta = 2$, and $\delta = 26$ mV.

To investigate the mechanical and electrical responses of the model, analyses for different frequency and resistance values as well as force amplitude are performed. The normalized driving frequency range is $\Omega = 0.8$ to 1.8 and the normalized resistance, defined as $r = C_p \omega_{sc} R$, ranges from $r = 10^{-4}$ to 10^4. At each frequency and resistance point a series of force values from $Y_0 = 0.25E-3$ N to $10.0E-3$ N with steps of $0.25E-3$ N are used starting with the lowest value and with each successive load increment starting the harmonic balance algorithm at the previous solution, essentially making it a continuation method. 10 harmonics were used for estimation of the waveforms in the algorithm, with a convergence criterion of 10^{-8} in the residual norm (Algorithm A-1, step 14). For this set of parameters, it took on average 4-5 iterations of the Newton

algorithm to converge for each load step. For each call of the harmonic balance algorithm the DC component of the converged rectified voltage V_{rect} and displacements for each harmonic are recorded, from which normalized power $\bar{P}$ and normalized displacement $\bar{u}$ are calculated as:

$$\bar{P} = \frac{\frac{V_{rect}^2}{R}}{\frac{Y_0^2}{\omega_{sc} m}}, \; \bar{u} = \frac{|u|}{\frac{Y_0}{k}}. \tag{A.24}$$

As a check for waveform convergence, frequency and resistance sweeps with $K = 20$ harmonics were performed which revealed errors in the harvesting voltages of less than 1%.

The results of this analysis can be seen in Figure A.3, which shows a case for low force at $0.25E-3$ N and at high force at $10.0E-3$ N. Also included is the analytical solution from Shu and Lien [140], which has no dependence on force. The most prominent difference between low and high forces, other than the power magnitudes, is the presence of two localized optimal frequency/resistance pairs in the high force case. This is a phenomenon noted by Shu and Lien [140], although in their study both the peaks had the same power harvesting value, which is not the case in the harmonic balance results. The peak near short circuit resonance produces less power than the other peak, which occurs near open circuit resonance. By artificially reducing the thermal voltage for the diode model (i.e. modeling the diode as more ideal), it was found, but not shown here, that both peaks approached the analytical solution provided by Shu and Lien [140]. This indicates that the lower power produced at the peak near short circuit resonance is a direct result of a more accurate diode model. A comparison of the locations and values for the power peaks in these three cases is shown in Table A.2.

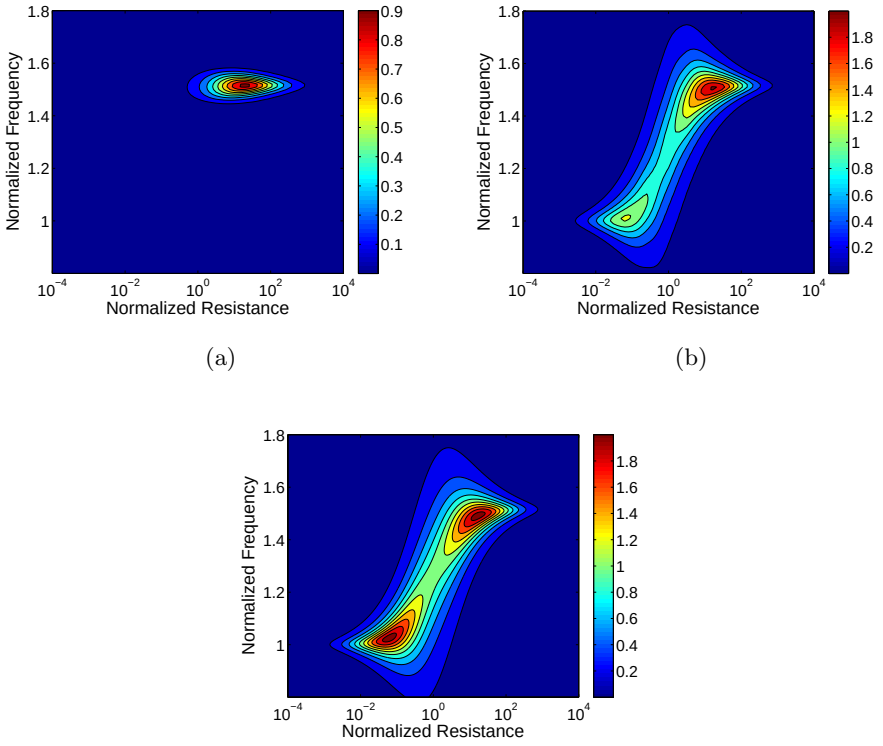

Figure A.3: Contour plots of normalized harvesting power for the lumped parameter model. (a) Low force, (b) high force, and (c) analytical solution from Shu and Lien (2006).

Table A.2: Comparison of peak power location and value.

	Analytical		FE - High force		FE - Low force
	Peak 1	Peak 2	Peak 1	Peak 2	Peak 1
Ω_{opt}	1.03	1.49	1.01	1.51	1.51
r_{opt}	0.0617	17.4	0.0631	15.9	20.0
$\bar{P}_{opt}$	2.08	2.08	1.22	2.01	0.919

An interesting phenomenon that can only be realized using the present method

is found upon inspection of the displacements experienced by the lumped parameter model. The model, being fully coupled to the circuit, receives feedback from the circuit that creates a structural response. For example, although the force upon the structure occurs only at one frequency, the harmonics created in the voltage and current signals cause the piezoelectric structure to act as an actuator, thereby creating displacements and vibrations at the harmonic frequencies. This is a phenomenon that has not been shown previously because of shortcomings caused by diode ideality assumptions of other models. The normalized displacement response as functions of the driving frequency and resistance are shown in Figure A.4 for the displacements occurring at the driving frequency itself f_0 and at the second harmonic $3f_0$. As was the case for the harvested power, the low and high force responses at the driving frequency are quite different with a single displacement mode for the low force case and two modes for the high force case. The normalized displacement responses for the second harmonic, however, show some unexpected and peculiar behavior. In the low force case the response as a function of driving frequency is similar, but the response of the second harmonic is largest for low resistances, which is opposite from the driving frequency response. In the high force case, on the other hand, the second harmonic behavior seems to have little connection with the driving frequency response. Although the magnitudes of the second harmonic responses are much lower than the driving frequency responses, the excitation of structural modes at that frequency or other harmonics could be detrimental to the system. The proposed analysis method captures these effects and allows accounting for them in the design process.

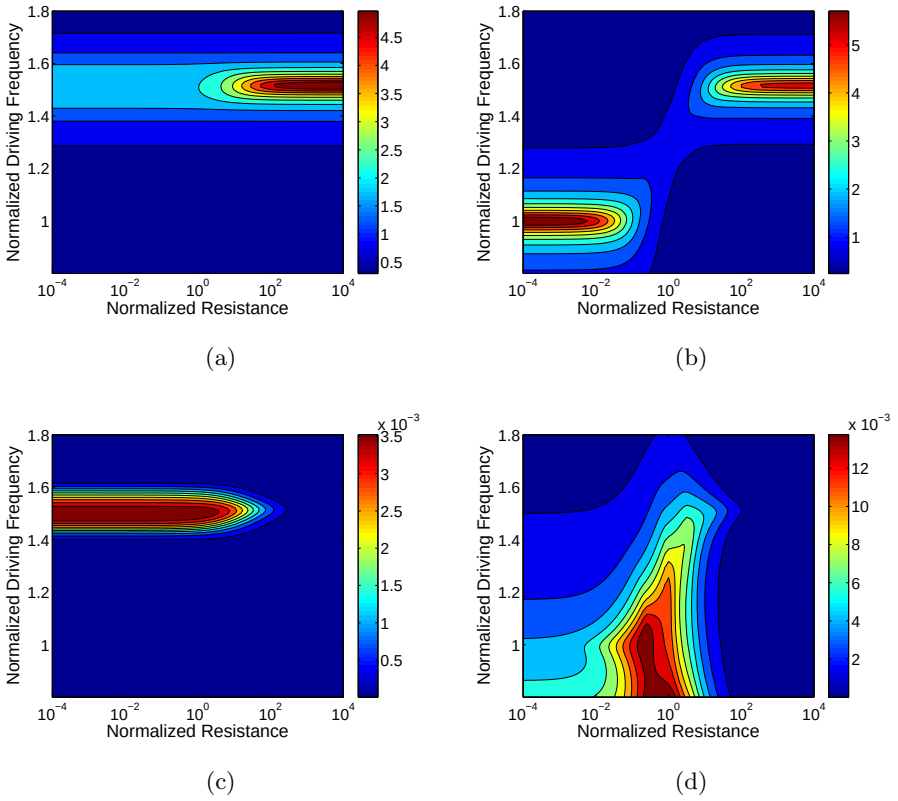

Figure A.4: Contour plots of normalized displacement for the lumped parameter model. (a) Low and (b) high force response at the driving frequency f_0. (c) Low and (d) high force response at the second harmonic $3f_0$.

A.3.2 Finite Element model

In the second example of the presented methodology a finite element model is considered as the piezoelectric harvester. The model setup, shown in Figure A.5, consists of a 10 cm x 10 cm square plate with a piezoelectric layer of thickness 0.2 mm surrounded by negligibly thin electrodes on top of an aluminum substrate of 1.0 mm thickness. The force on the plate is actuated along a 4 mm middle section of the left edge in the direction normal to the plate. The material properties of the piezoelectric (PZT-5H) and aluminum substrate are provided in Table A.3. Mass proportional damping of 2% at 714.5 Hz is also included in the model. The finite element model consists of a mesh

of 25 x 25 layered composite piezoelectric plate/shell elements. The circuit is the same as before.

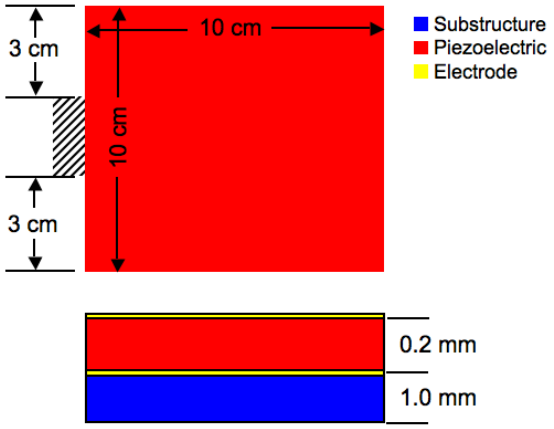

Figure A.5: Setup of piezoelectric harvester finite element model.

Table A.3: Material properties used in finite element example.

	Mass density	Stiffness properties	Piezoelectric properties
Piezoelectric (PZT-5H)	$\rho = 7500\ kg/m^3$	$c_{11} = c_{22} = 127\ GPa$	$e_{31} = -6.62\ N/C$
		$c_{12} = 80.2\ GPa$	$e_{33} = 23.2\ N/C$
		$c_{13} = c_{23} = 84.7\ GPa$	$\epsilon_{33} = 1.28E-8\ F/m$
		$c_{33} = 117\ GPa$	
Aluminum	$\rho = 2700\ kg/m^3$	$E = 73.0\ GPa,\ \nu = 0.33$	

Similar to the previous example, the harvesting power as a function of frequency and resistance is sought. Here, however, normalized parameters are not used because they are not simple when using a finite element model. The driving frequency is varied from $f_0 = 650$ Hz to 760 Hz while the harvesting resistance is varied from $R = 10^{-4}\ \Omega$ to $10^4\ \Omega$. The force magnitude is varied from $Y_0 = 2.5E-2$ N to 2.0 N stepping by $2.5E-2$ N, again creating a continuation approach. In the harmonic balance algorithm,

$K = 20$ harmonics were used and a convergence criterion of 10^{-8} in the residual norm was used. The harvesting power is calculated via $P = V_{rect}^2/R$.

To give an idea of what the structural response looks like for this finite element model, a broadband frequency sweep of average dissipation power is performed for the finite element model with only a 100 Ω resistor as the external circuit rather than the full-bridge rectifier. The voltage frequency response function for this linear system is shown in Figure A.6 along with a contour plot of average dissipation power as a function of both frequency and resistance. Figure A.7 then shows the results of the full-bridge rectifier circuit analysis for low ($Y_0 = 7.5E-2$ N) and high ($Y_0 = 2.0$ N) force magnitudes. The difference between the linear and nonlinear cases is clear. In the linear resistive system a very small peak shows up, while in the full-bridge system, the peak power is much broader in its range of effectiveness for both low and high forcing. As was found for the lumped parameter model, in the nonlinear analysis the location of peak power shifts and changes shape with increasing load. Noticeably a second peak did not appear for the finite element model, although this is not necessarily unexpected as the system dynamics are much more complex.

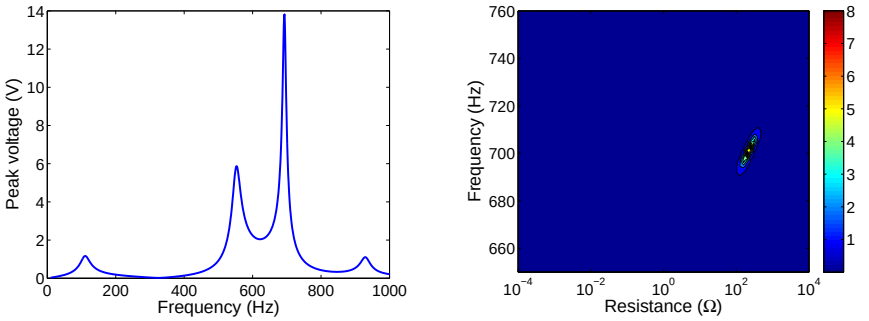

(a) (b)

Figure A.6: (a) Peak voltage frequency response function ($R = 100$ Ω) and (b) contour plot of average dissipated power as a function of frequency and resistance for a linear resistive system.

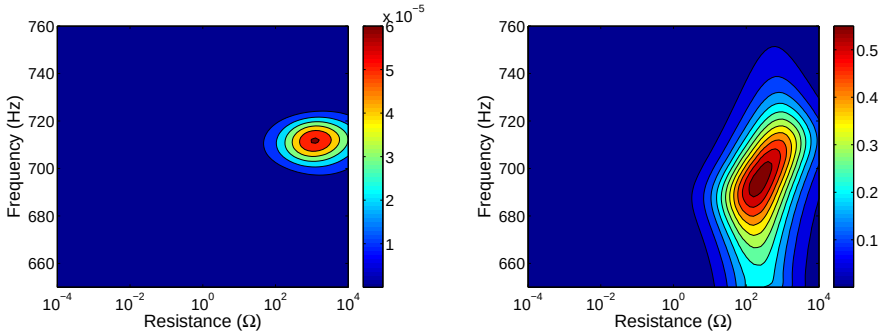

(a) (b)

Figure A.7: Contour plots of the harvesting power for the finite element model for (a) low force and (b) high force.

A.4 Conclusions

A methodology for accurately analyzing the electromechanical response of piezoelectric harvesting structures connected to nonlinear harvesting circuits is developed. Through the examples it has been shown that the nonlinear effects of a full-bridge rectifier circuit do significantly change the electrical response of piezoelectric energy harvesting systems when compared with currently available analytical models. On the other hand, the effects of higher order feedback are generally negligible when compared to the primary response at the driving frequency. In sensitive systems, however, this may not be true and may pose a significant problem in systems where unwanted modes could be excited. Thus, special design considerations may be necessary with the use of nonlinear circuits. As a result, this analysis methodology significantly improves upon existing analysis techniques and can provide and valuable information that is otherwise unavailable for the design and response of piezoelectric energy harvesting systems.